

## Tomography of the $z \sim 2$ Circumgalactic Medium using KBSS Galaxy Pairs\*

NIKOLAUS Z. PRUSINSKI <sup>1</sup>, CHARLES C. STEIDEL <sup>1</sup>, AND YUGUANG CHEN <sup>2,3</sup>

<sup>1</sup>*Cahill Center for Astronomy and Astrophysics, California Institute of Technology, MC 249-17, Pasadena, CA 91125, USA; [nik@astro.caltech.edu](mailto:nik@astro.caltech.edu), [ccs@astro.caltech.edu](mailto:ccs@astro.caltech.edu)*

<sup>2</sup>*Department of Physics and Astronomy, University of California Davis, 1 Shields Avenue, Davis, CA 95616, USA*

<sup>3</sup>*Department of Physics, The Chinese University of Hong Kong, Shatin, N.T., Hong Kong SAR, China; [yuguangchen@cuhk.edu.hk](mailto:yuguangchen@cuhk.edu.hk)*

(Received 2025 March 25)

Submitted to ApJ

### ABSTRACT

We present new results on the spatial structure and kinematics of Ly $\alpha$  and several far-UV metallic ions in the circumgalactic medium of Keck Baryonic Structure Survey galaxies using foreground/background galaxy pairs with angular separations  $\leq 30''$ . Keck/KCWI and Keck/LRIS spectra of 736 background galaxies with  $\langle z_{\text{bg}} \rangle = 2.58 \pm 0.38$  probe sightlines through 1033 foreground galaxies ( $\langle z_{\text{fg}} \rangle = 2.03 \pm 0.36$ ) at projected distances  $8 \leq D_{\text{tran}}/\text{kpc} \leq 250$ . For each ion, we measure equivalent widths ( $W_\lambda$ ) as a function of  $D_{\text{tran}}$  and find  $W_\lambda \propto D_{\text{tran}}^{-\gamma}$  with  $0.3 \lesssim \gamma \lesssim 0.6$ . Higher ionization species (C IV) decrease less rapidly and extend to larger  $D_{\text{tran}}$  compared to low ions (O I, C II, Si II). Splitting the pair sample into subsets based on foreground galaxy properties, we find  $W_\lambda(\text{C IV})$  exhibits a strong dependence on stellar mass ( $M_*$ ) and a weaker dependence on star formation rate. Similarly,  $W_\lambda(\text{Ly}\alpha)$  increases with  $M_*$ , albeit with more scatter. In 2D, we map the excess Ly $\alpha$  and C IV absorption as functions of line-of-sight velocity and  $D_{\text{tran}}$ . The Ly $\alpha$  velocity centroid varies with  $D_{\text{tran}}$ ; at  $D_{\text{tran}} \lesssim 50$  kpc, Ly $\alpha$  emission from the foreground galaxy affects the Ly $\alpha$  absorption feature measured in the background galaxy spectrum, resulting in a net blueshifted absorption profile. We construct a two-component model to fit the observed Ly $\alpha$  map. The best fit suggests approximately half of the excess Ly $\alpha$  absorption arises from a decelerating outflow component with initial velocity  $v_{\text{out}} \simeq 750$  km s<sup>-1</sup>; the remainder is associated with a component centered on the galaxy systemic redshift with a  $D_{\text{tran}}$ -independent 1D velocity dispersion of  $\sigma_v \simeq 220$  km s<sup>-1</sup>, consistent with the average foreground galaxy circular velocity.

**Keywords:** Circumgalactic medium (1879); Galaxy evolution (594); Galaxy pairs (610); High-redshift galaxies (734)

### 1. INTRODUCTION

Galaxies evolve via the cycling of baryons between gas reservoirs in the intergalactic medium (IGM) and their own interstellar media (ISM). The circumgalactic medium (CGM) represents the sphere of influence for a galaxy and acts as a boundary layer where one can directly observe the exchange of baryons to and from the IGM. Despite its importance in galaxy formation, the CGM and the underlying processes

driving its evolution with time remain largely unconstrained (Tumlinson et al. 2017).

Observational and theoretical work has established that the CGM of star-forming galaxies comprises metal-enriched gas (e.g., Peeples et al. 2014; Péroux & Howk 2020; Dutta et al. 2020, 2021) in a clumpy morphology (e.g., Rubin et al. 2018b; Rudie et al. 2019; Erb et al. 2023; Li et al. 2024) across a range of temperatures, densities, and ionization states (e.g., Byrohl & Nelson 2023; Faucher-Giguère & Oh 2023). The multiphase nature of the CGM is the result of a combination of baryonic feedback processes e.g., supernova ejecta (Leitherer et al. 1999; Veilleux et al. 2005), active galactic nuclei (Faucher-Giguère & Quataert 2012), and radiation pressure (Murray et al. 2011) from massive stars all acting in concert to shape the gas distribution and physical con-

\* Based on data obtained at W. M. Keck Observatory, which is operated as a scientific partnership among the California Institute of Technology, the University of California, and the National Aeronautics and Space Administration. The Observatory was made possible by the generous financial support of the W. M. Keck Foundation.

ditions. Numerous studies across a range of redshifts have observed outflows which inject energy and momentum into the ISM and CGM of their host galaxy (e.g., Shapley et al. 2003; Weiner et al. 2009; Steidel et al. 2010; Martin et al. 2012; Erb et al. 2012; Prusinski et al. 2021); signatures of inflowing material are much less common (e.g., Kereš et al. 2005; Rubin et al. 2012; Bouché et al. 2013), but the connections between such baryonic flows, the underlying CGM gas distribution, and the host galaxy properties remain uncertain.

A natural epoch in which to study the CGM around galaxies is at  $z \sim 2 - 3$  where the global star formation rate, baryonic accretion rate, and supermassive black hole growth all reached their peak (e.g., Richards et al. 2006; Faucher-Giguère et al. 2011; Behroozi et al. 2013; Madau & Dickinson 2014). At these redshifts, many of the rest-frame far-UV and optical diagnostics fall into wavelength windows with high atmospheric throughput and can therefore be observed using ground-based telescopes (see e.g., Steidel et al. 2014). Indeed, galaxies in this redshift range show prominent outflows, extended H I halos in both emission and absorption, and substantial metal absorption in their CGM (Bouche et al. 2007; Steidel et al. 2010, 2011; Rudie et al. 2012; Leclercq et al. 2020; Chen et al. 2021; Weldon et al. 2022).

Prior to the early 1990s, the connection between diffuse, metal-enriched gas and galaxies was based largely on the statistical incidence of various classes of intervening absorption systems in spectroscopic surveys of QSOs – the characteristic “size” of extended gas in galaxy halos was derived from a combination of the observed incidence per unit redshift path length of absorption systems (e.g. Mg II, C IV, damped Ly $\alpha$ ) and the space density of galaxies with which the gas was assumed to be bound, yielding “predicted” halo sizes of  $R_{\text{gal}} \simeq 20 - 100$  pkpc, depending on the sensitivity of the QSO absorption system samples, the tracer ion, and the assumed scaling relation between galaxy luminosity and galaxy gaseous cross-section. More direct association of QSO absorption systems and intervening galaxies began at low redshift: deep CCD images of QSO sightlines with known  $z \simeq 0.2 - 0.5$  Mg II absorption systems were used to identify candidate absorbing galaxies within several arcsec of the QSO, followed by spectroscopic observations of the relatively faint ( $R \gtrsim 20$ ) galaxies to confirm their redshifts (Bergeron & Boissé 1991). The initial success in identifying  $\simeq L^*$  galaxies within  $\lesssim 50$  kpc of the QSO sightline appeared to support the general expectations that had been based on simple statistical arguments.

However, the small samples of identified absorbing galaxies, in addition to being observationally expensive, were subject to potential observational selection biases – e.g., one cannot be certain that the galaxy identified is the one responsible for the absorption system, or simply the most easily-observed galaxy at the same redshift near the QSO sight-

line. A less biased means of establishing the connection between galaxies and absorbers would be to first observe galaxies near QSO sightlines, where each would have known luminosity, stellar mass, SFR, etc., as well as separation from the QSO sightline  $D_{\text{tran}}$ , and subsequently look for absorption signatures (or sensitive limits) in the QSO spectrum for each. Such a “galaxy-centered” approach – where galaxy samples are observed in fields deliberately chosen to have one or more bright background sources (usually QSOs) that can provide high-quality measurements of diffuse gas over the relevant range of redshift – has become more practical on large telescopes equipped with efficient multi-object spectrographs (MOS) or integral field units (IFUs).

An alternative to using background QSOs is to use unrelated foreground-background galaxy pairs, which are 50–100 times more numerous within the Keck Baryonic Structure Survey (KBSS) than QSO-galaxy sightlines (e.g. Adelberger et al. 2005; Steidel et al. 2010; Chen et al. 2020). The CGM of a particular foreground galaxy (at  $z_{\text{fg}}$ ) can be probed using spectroscopy of background galaxies ( $z_{\text{bg}} > z_{\text{fg}}$ ), each of which forms a sightline through the foreground CGM. In this way, background galaxies and background QSOs offer two complementary means of sampling a foreground galaxy’s CGM using independent sets of sightlines, but stacks of galaxy spectra converge faster than QSO sightlines to the average foreground gas distribution (Steidel et al. 2010). Three representative examples of how this technique works are shown in Figure 1. Note how the projected distance ( $D_{\text{tran}}$ ) for the Q0142-BX195-BX188 pair is approximately twice that of the pairs in the top two panels and has comparatively weaker absorption features. In addition, unlike the other spectra, Q0142-BX195 (the background system in the pair) is an AGN, but as long as the background spectrum has a continuum measured with sufficient  $S/N$ , it can be used to measure foreground absorption. In principle, a sparsely sampled grid of sightlines can be used to characterize the physical conditions in a foreground galaxy and its surrounding CGM.

Galaxy foreground-background close angular pairs drawn from what would become the KBSS survey were used by both Adelberger et al. (2005) and Steidel et al. (2010); the latter study constructed a sample of 512 galaxy pairs with angular separations  $\theta \leq 15''$  from a sample of  $z \sim 2 - 3$  star forming galaxies. The galaxy pairs were subdivided into three composite spectra ( $\langle D_{\text{tran}} \rangle \in [31, 63, 103]$  kpc) to make a low resolution map of absorption as a function of  $D_{\text{tran}}$  (their Figure 21). They used the measurements of absorption line equivalent widths ( $W_\lambda$ ) versus  $D_{\text{tran}}$ , combined with the stack of “down the barrel” (DTB;  $D_{\text{tran}} = 0$  kpc) spectra of the foreground galaxies in each angular pair, to model the velocity field and galactocentric radial distribution of absorbing gas in the “mean” CGM surrounding galaxies

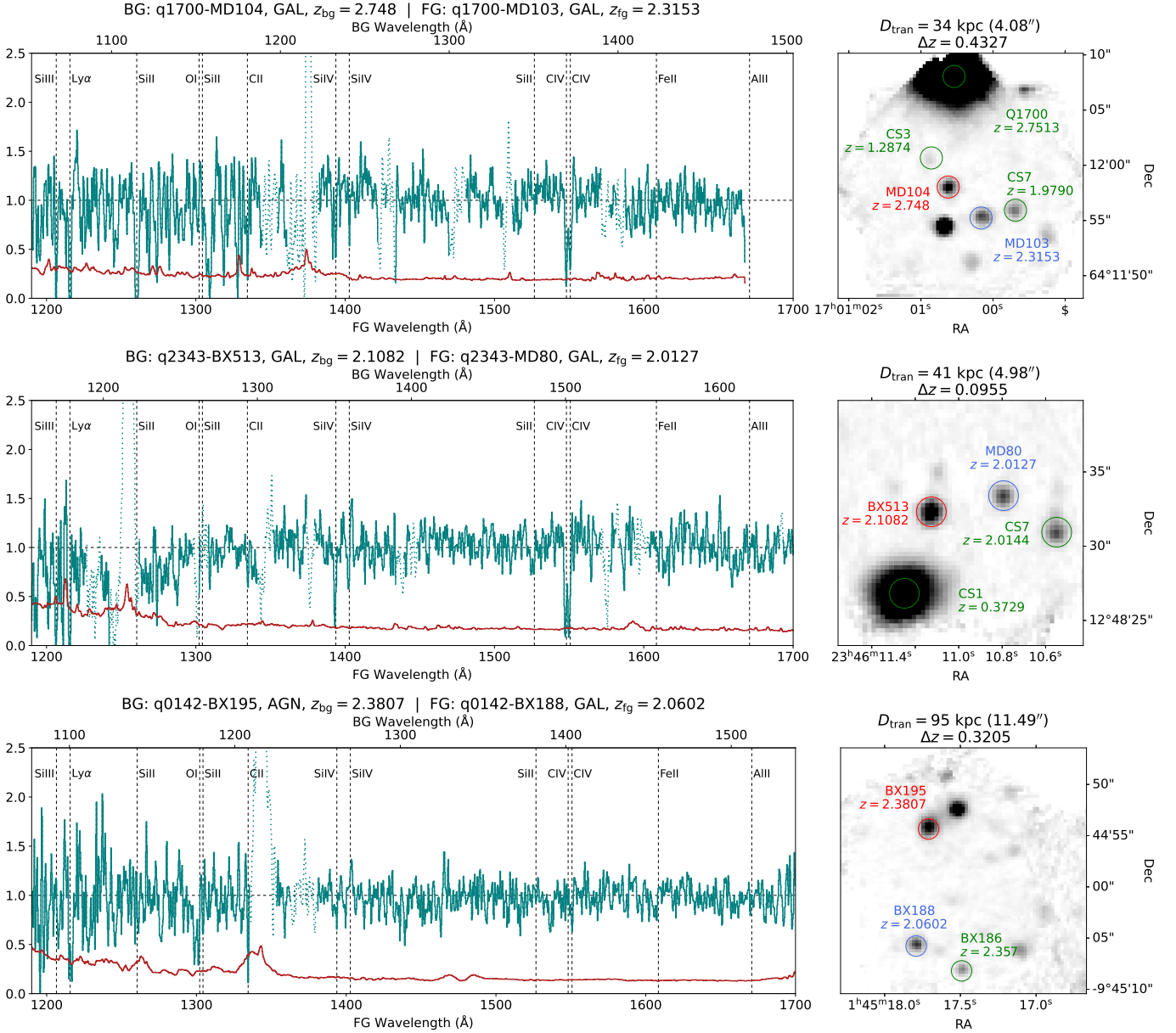


**Figure 1.** Example KCWI background galaxy spectra, normalized and shifted to the rest frame of the foreground galaxy of the pair, from the KBSS-KCWI sample. The righthand images show the white light (3530 – 5530 Å) image from the relevant KCWI pointing, where the background galaxy is labeled in red and the foreground galaxy in blue; green labels indicate other galaxies with spectroscopic identifications within the field of view. Spectral features at the redshift of the FG in each pair are indicated with vertical dashed lines and labels. The location of the same set of features at the BG redshift have been highlighted with a dotted line style. The three cases have  $D_{tran} \simeq 34, 41,$  and  $95$  kpc, respectively.

at  $\langle z \rangle = 2.2$ . They found that all of the observed metallic species were observable to  $D_{tran} \simeq 70 - 100$  kpc, at which point the equivalent widths fell below the detection limit of  $W_\lambda \simeq 0.1$  Å. Excess Ly $\alpha$  absorption remained detectable to at least  $D_{tran} \sim 250$  kpc, as expected given the earlier results using background QSOs to probe similar galaxies in the same fields (Adelberger et al. 2005).

Chen et al. (2020) extended the galaxy pair technique by incorporating a larger sample of galaxy spectra ( $N \simeq 3000$

with  $1.7 \lesssim z \lesssim 3.4$ ), with an increased range of pair separations, drawn from the KBSS survey regions. The authors assembled more than 200,000 foreground/background galaxy pairs with angular separations  $\Delta\theta \simeq 3 - 500''$  ( $20 \lesssim D_{tran}/\text{kpc} \lesssim 4000$ ) and produced maps of Ly $\alpha$  absorption strength as a function of line of sight velocity (with respect to the foreground galaxy systemic redshifts)  $v_{LOS}$  and  $D_{tran}$ . They found that, if expressed as a single power law,  $W_\lambda(\text{Ly}\alpha) \propto D_{tran}^{-0.4}$  over the full range of impact param-

ters, in agreement with Steidel et al. (2010). The number of galaxy pairs sampling separations  $D_{\text{tran}} \leq 100$  kpc – i.e., the range over which metal lines had been detected by Steidel et al. (2010) – was not significantly larger, so only the distribution and kinematics of Ly $\alpha$  were analyzed.

In the present work, our goal has been to construct an ensemble of foreground/background galaxy pairs that provides improved sampling of gas within  $D_{\text{tran}} \leq 250$  kpc, the approximate scale of the CGM surrounding individual  $L_{\text{UV}}^*$  galaxies at  $z \simeq 2 - 3$  established by previous work using KBSS QSO sightlines. We are also interested in improving the constraints on CGM gas-phase kinematics (both H I and metals) and its relation to the properties of the foreground galaxies; to this end, from Chen et al. (2020) we include only the subset ( $\sim 30\%$ ) of background galaxy spectra observed with the higher spectral resolving power configuration of LRIS-B ( $\langle R \rangle \sim 1300$ ; see Appendix B of Chen et al. 2020). The most significant improvement – the one that has motivated our revisiting the use of close angular pairs of galaxies – comes from incorporating deep IFU pointings using the Keck Cosmic Web Imager (KCWI; Morrissey et al. 2018). The KCWI data set (KBSS-KCWI; see Chen et al. 2021) consists of IFU observations of many contiguous  $\sim 20''$  diameter ( $\simeq 170$  kpc at  $z \sim 2$ ) regions within the KBSS survey fields. The KBSS-KCWI subsample provides deep ( $\gtrsim 5$  hour total integrations per pointing) spectra with resolving power  $\langle R \rangle \simeq 1800$  of a large number of galaxy angular pairs with projected separations  $\leq 20''$ , including previously-known KBSS galaxies as well as fainter galaxies newly-identified from their extracted KCWI spectra. The KCWI pointings are embedded within larger KBSS survey fields, each of which has extensive photometric and spectroscopic ancillary data. All of the galaxy spectra included in the combined LRIS+KCWI sample have resolving power  $R \simeq 1500 \pm 300$ , such that the C IV  $\lambda\lambda 1548, 1550$  doublet is resolved, as are O I  $\lambda 1302.2$  and Si II  $\lambda 1304.4$ .

This paper is organized as follows: in Section 2, we discuss the observations and data reduction associated with each instrument subsample; Section 3 covers the construction of the galaxy pair sample comprising galaxies from all subsamples; Section 4 presents results from Ly $\alpha$  and metal absorption features; Section 5 features maps of Ly $\alpha$  and C IV absorption; these results are placed in a broader context in Section 6; and finally, we summarize our conclusions in Section 7. Appendix A justifies why an explicit redshift cut is not required for our sample; Appendix B uses pairs generated from HIRES spectra of background QSOs to elucidate the profiles we observe at low resolution; Appendix C shows how different stacking methods affect the composite spectra; and Appendix D details how, for galaxy pairs with close angular separations, Ly $\alpha$  emission from the foreground galaxy can modulate the observed background Ly $\alpha$  absorption signal.

Throughout this paper, we adopt the *Planck* 2018 cosmology (Planck Collaboration et al. 2020): a flat  $\Lambda$ CDM model with  $H_0 = 67.7$  km s $^{-1}$  Mpc $^{-1}$ ,  $\Omega_{m,0} = 0.31$ , and  $\Omega_{\Lambda,0} = 0.69$ . In this cosmology, at the median redshift of the sample ( $z_{\text{med}} = 2.3$ ),  $1''$  corresponds to 8.4 (physical) kpc. We use  $D_{\text{tran}}$  to represent the projected physical separation between a foreground galaxy and the line of sight to a background object, evaluated at the redshift of the foreground galaxy ( $z_{\text{fg}}$ ); we direct the reader to Figure 23 of Steidel et al. (2010) for a schematic.

## 2. OBSERVATIONS

The KBSS spectra used in this study are drawn from several observing programs using various instruments and reduction strategies.

### 2.1. KBSS-KCWI

The KBSS-KCWI spectra (Chen et al. 2021, 2025) used in this paper comprise 193 galaxies observed in 46 different KCWI pointings, selected to include objects from KBSS. KBSS-KCWI pointings maximize the number of previously identified galaxies in each field, in particular those with data from LRIS (Steidel et al. 2004), MOSFIRE (McLean et al. 2012), and *HST* WFC3-IR imaging. Of the 193 targets, 7 are optically faint AGN, while the remainder are star-forming galaxies.

KCWI observations were conducted between 2017 September and 2022 June, after which KCWI went offline for red-channel integration. The integral field spectra used in this study were obtained using KCWI’s low resolution grating (BL; central wavelength = 4500 Å) and Medium slicer (slices were sampled with  $0''.3$  pixels) using  $2 \times 2$  detector binning resulting in cubes with a  $20''.4 \times 16''.5$  FoV and spectral resolution  $\langle R \rangle \approx 1800$  over the 3530 – 5530 Å bandpass. Each KBSS-KCWI field was observed for a typical total integration time of five hours, with dithers and/or position angle (PA) rotations after every twenty minute exposure. In the end, the data cube maps a region with a  $20''$  diameter (170 kpc at  $\langle z \rangle = 2.3$ ) with approximately uniform exposure.

Individual exposures were reduced using a customized version of the IDL KCWI Data Reduction Pipeline (DRP; Neill et al. 2023)<sup>1</sup> described in detail in Chen et al. (2021). Briefly, each twenty minute science frame was converted into a 3D flux calibrated cube and each exposure was then coadded into a stacked cube using the KCWIKit package (Chen et al. 2021; Prusinski & Chen 2024). KCWIKit reads in a list of cubes to be stacked; a parameter file enumerating e.g. the final stack pixel scale, dimensions, and orientation; and if necessary, a list of pre-alignment cube world coordinate system (WCS) shifts if the header WCS is incorrect or significantly

<sup>1</sup> <https://github.com/Keck-DataReductionPipelines/KcwiDRP>

offset from the rest of the stack. The code runs natively in a `jupyter` (Kluyver et al. 2016) environment and begins by aligning each cube with respect to a fiducial frame (the first in the list of cubes by default). The code cross-correlates each frame, then drizzles them onto a common grid weighted by exposure time using the `Montage`<sup>2</sup> (Jacob et al. 2010) package. Since all data were taken in the Medium BL configuration, each cube has the same wavelength range and sampling ( $1 \text{ \AA pix}^{-1}$ ). The WCS of the stacked cube is then corrected using an external observation (typically *HST* F160W images) to match the astrometry of existing KBSS ancillary data products. The final output is a WCS-registered  $\sim 20''$  (170 kpc) diameter pointing.

For each stacked cube, we also constructed a “white light” (3530 – 5530 Å) image and used `Source Extractor` (Bertin & Arnouts 1996) to detect all significant continuum sources; all detected continuum sources were extracted to 1D from the data cubes by weighting each spatial element within the detected segmentation region by the  $(S/N)^2$  of the white light signal. Some of the continuum sources detected in each KCWI pointing were not KBSS catalog objects, but yielded spectroscopic redshifts placing them in the targeted range for the present purposes,  $1.6 \leq z \leq 3.5$ , and were bright enough for spectral energy distribution (SED) fitting. These sources (of which there are 51 in all) have been labeled “CS” (continuum serendipitous) along with their segmentation IDs (e.g., CS3 – see Figure 1). Of the 51 galaxies, 22/51 (43%) are fainter than the KBSS continuum limit ( $\mathcal{R} \geq 25.5$ ), with a limiting  $\mathcal{R}$ -band magnitude of 27.33.

## 2.2. LRIS

LRIS spectra comprise the bulk of the KBSS rest-frame far-UV spectroscopic sample, having been accumulated over  $\sim$ two decades, and as such we direct the reader to Steidel et al. (2003, 2004) and Adelberger et al. (2004) for color selection criteria and data reduction strategies of the QSO field observations used in this study. LRIS observations are used to supplement KCWI observations and include a portion of the KBSS galaxy pair sample (KGPS) compiled by Chen et al. (2020) which at the time comprised a broad superset of the galaxies used previously in numerous projects (e.g. Steidel et al. 2003, 2004; Adelberger et al. 2005; Reddy et al. 2006; Steidel et al. 2010). Notably, in the current work we include only galaxy pairs with angular separations  $\Delta\theta \leq 30''$  ( $\sim 250$  kpc) and background galaxy spectra obtained with the higher resolution 600 lines  $\text{mm}^{-1}$  LRIS-B grism. The latter condition translates to LRIS spectra with  $R \sim 1300$  (Chen et al. 2020), marginally lower resolution than KCWI at the same wavelengths.

The bulk of the LRIS data used in this sample were obtained between 2002 and 2016. 872/2862 spectra from the KGPS sample were observed with the 600 lines  $\text{mm}^{-1}$  grism blazed at 4000 Å, and of those, 400/872 were observed on more than one slitmask. Each slitmask was observed for a minimum of 1.5 hours and 30% of the 600 lines  $\text{mm}^{-1}$  grism slitmasks have exposure times of at least 3 hours. 155/872 of the galaxies have LRIS red channel data but the galaxy pair analysis in this study uses only the blue channel data since the blue channel spectra cover approximately the same wavelength range as the KCWI configuration described earlier ( $\sim 3500 - 5500$  Å).

Of the 872 galaxies that make up the LRIS sample ( $1.4 \leq z \leq 3.64$ ), 135 were observed with long integration ( $\sim 10$  hours). The KBSS-LM1 sample was compiled between 2014 and 2016 to be a deep collection of LRIS rest-UV spectra at  $2.10 \leq z_{\text{gal}} \leq 2.58$  corresponding to the highest quality KBSS-MOSFIRE spectra. Sample selection criteria are described by Steidel et al. (2016) and Theios et al. (2019), but in short, the galaxies were chosen to maximize the overlap with the existing KBSS-MOSFIRE sample, and especially pertinent for this work, the KBSS fields were prioritized so that the largest number of galaxies could be observed on a single slitmask.

## 3. GALAXY PAIR SAMPLE

To understand the bulk properties of gas in galaxies’ circumgalactic media, we assembled a sample of galaxy pairs from the KCWI and LRIS subsamples. A galaxy pair consists of a foreground and background galaxy (at redshifts  $z_{\text{fg}}$  and  $z_{\text{bg}}$  respectively) with a projected separation on the sky satisfying the following requirements:

- $\Delta\theta < 30''$  so that the background galaxy probes the foreground galaxy’s CGM within 250 kpc.
- $\Delta v = \frac{c\Delta z}{1+z_{\text{bg}}} \gtrsim 3,000 \text{ km s}^{-1}$ , where  $\Delta z = z_{\text{bg}} - z_{\text{fg}}$  to ensure the two galaxies are not part of the same structure. For the average foreground redshift  $\langle z_{\text{fg}} \rangle = 2.3$ ,  $\Delta z \gtrsim 0.03$ . We do not impose an upper bound on  $\Delta v$  (see Appendix A).
- $z_{\text{fg}} > 1.4$ , such that at least C IV falls within low noise regions of both the LRIS and KCWI spectra.
- The background galaxy has been observed with KCWI or LRIS with the 600 line  $\text{mm}^{-1}$  grism.
- The background object in a pair is not a QSO. The rationale behind this decision is discussed in Section 1 and Appendix B, but in general we study foreground CGM gas probed by background galaxies.
- The foreground object in a pair is neither a QSO nor an AGN. We only probe the CGM of foreground galaxies.

<sup>2</sup> <http://montage.ipac.caltech.edu/>

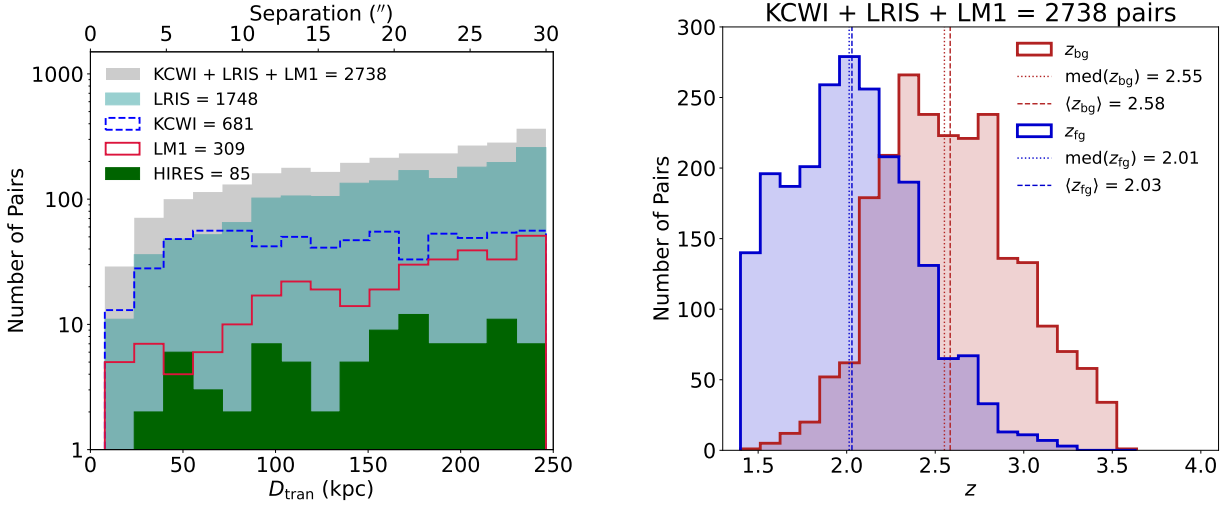


**Figure 2.** *Left:* Histogram of  $D_{\text{tran}}$  for the galaxy pair sample. The full distribution of projected distances is shown in gray and KCWI pairs are shown in the dashed blue histogram. KCWI background spectra are supplemented by LRIS (cyan histogram) and LM1 (red outline) observations, the former of which begins to dominate at  $D_{\text{tran}} \gtrsim 100$  kpc. There are 2738 pairs in total and respective totals are enumerated in the plot legend. The HIRES pair distribution constructed from background QSOs is shown for comparison in green. *Right:* The redshift distribution of foreground (blue) and background (red) galaxies in the galaxy pair sample along with vertical dotted and dashed lines denoting the median and mean redshifts respectively.

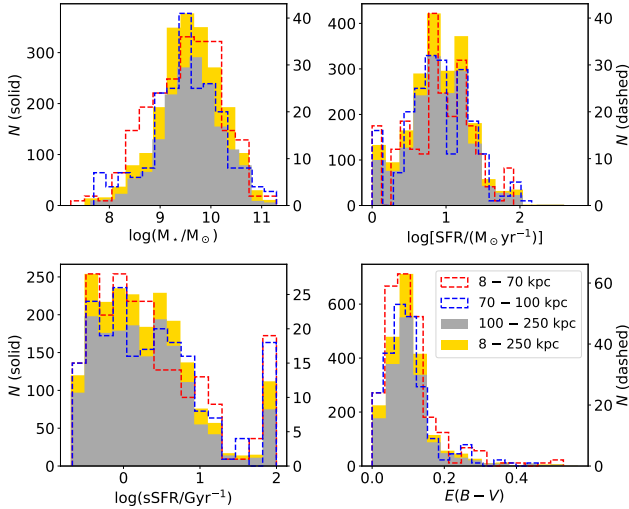


**Figure 3.** Foreground galaxy property distributions for  $M_*$  (top left), SFR (top right), sSFR (bottom left), and  $E(B - V)$  (bottom right). The yellow histogram shows the properties over the full range of  $D_{\text{tran}}$  probed in this sample, while the red outline, blue outline, and solid gray histogram correspond to samples drawn from  $D_{\text{tran}} = 8 - 70$  kpc,  $70 - 100$  kpc, and  $100 - 250$  kpc, respectively. The number of pairs in the solid histograms is shown on the left vertical axis, while the numbers in the dashed histograms (with considerably fewer pairs but a similar overall distribution) are shown on the right vertical axis.

- For the purpose of binning the sample by galaxy properties (Section 4.3), we require the foreground galaxy to have an SED fit.

Since we are interested in using background galaxy spectra to measure foreground absorption, a well-determined foreground galaxy redshift is essential to ensure accurate velocity measurements in the shifted spectra. To that end, where possible, nebular redshifts from KBSS-MOSFIRE (Steidel et al. 2014; Strom et al. 2017, 2018) were used to determine galaxy systemic velocities. The KBSS-MOSFIRE nebular redshifts have systemic redshift uncertainties  $\Delta v_{\text{MOSFIRE}} \simeq 18 \text{ km s}^{-1}$  (Steidel et al. 2014), considerably higher velocity accuracy than either LRIS ( $\sigma_{\text{LRIS}} \simeq 107 \text{ km s}^{-1}$ ) or KCWI ( $\sigma_{\text{KCWI}} \simeq 71 \text{ km s}^{-1}$ ). When nebular emission line measurements were not available, rest-frame UV emission (i.e. Ly $\alpha$ ) and low ionization interstellar (LIS) absorption features (e.g. Si II, C II) were used to calculate the systemic redshift, using the redshift calibration rules outlined by Chen et al. (2020); in such cases the typical redshift accuracy is  $\sigma_{\text{UV}} \simeq 100 \text{ km s}^{-1}$  (Steidel et al. 2018).

To assemble the sample, we started by constructing galaxy pairs for all known foreground galaxies in KBSS where the corresponding background galaxy had been observed with KCWI; 681 pairs with a KCWI-observed background galaxy satisfied the criteria above, 341 (51%) of which had a foreground galaxy with a nebular redshift. The number of KCWI pairs reaches a peak count at  $D_{\text{tran}} \simeq 50$  kpc and plateaus for  $D_{\text{tran}} > 100$  kpc (see the blue dashed histogram outline in the left panel of Figure 2). The lack of pairs with  $D_{\text{tran}} > 50$  kpc is an artifact of the KCWI observing strategy: 252/681 (37%) of the KCWI galaxy pairs have their foreground and background galaxies on the same KCWI pointing (which are  $\approx 170$  kpc in diameter). The remaining 429 (63%) pairs involve a KCWI background galaxy and a foreground galaxy

that falls off the KCWI footprint but still probes gas (at  $z_{\text{fg}}$ ) in the KCWI background galaxy spectrum.

To supplement the number of pairs sampling larger  $D_{\text{tran}}$ , we then formed pairs where the background galaxy was one observed with LRIS-B (the blue channel of LRIS). This added 1748 galaxy foreground/background pairs from the general LRIS sample ( $t_{\text{int}} \simeq 1.5 - 4.5$  hours; cyan solid histogram in the left panel of Figure 2) and 309 pairs from LM1 masks ( $t_{\text{int}} \simeq 10 - 12$  hours; red histogram outline in Figure 2) to the initial KCWI sample, mostly sampling  $100 \lesssim D_{\text{tran}}/\text{kpc} \lesssim 250$ ; 879 of the 1748 (50%) LRIS pairs and 186/309 (60%) of the LM1 pairs had foreground galaxies with nebular redshifts. In the end, 2738 pairs (1406 [51%] with foreground nebular redshifts) sampling  $8 \leq D_{\text{tran}}/\text{kpc} \leq 250$  ( $\Delta\theta \sim 1'' - 30''$ ) met all of our selection criteria. The final sample of galaxy pairs is summarized in Figure 2. The foreground galaxy stellar mass ( $M_*$ ), star formation rate (SFR), specific star formation rate (sSFR  $\equiv \text{SFR}/M_*$ ), and the inferred reddening  $E(B - V)$  distributions are shown in Figure 3. A thorough description of the SED fitting underlying these measurements can be found in Steidel et al. (2016, 2018) and Theios et al. (2019). We will return to the stellar population parameters of the foreground galaxies in Section 4.3.

### 3.1. Stacking

Each background spectrum in the pair sample has the possibility of absorption systems at  $z_{\text{bg}}$ ,  $z_{\text{fg}}$ , and possibly other “contaminating” redshifts (especially in the Ly $\alpha$  forest). With sufficiently high-resolution spectra it is possible to isolate each system, but in spectra with  $\langle R \rangle \simeq 1000$ , they become blended. Nevertheless, averaging over a sufficiently large number of spectra at different redshifts results in a new suppressed continuum (Appendix B) and can mitigate the contamination from such absorption systems since each sightline probes a random gas distribution. Furthermore, the increased effective  $S/N$  of composite foreground spectra (binned by  $D_{\text{tran}}$ ) facilitates the detection of weaker (metallic) absorption features.

Before stacking, each background galaxy spectrum was trimmed in wavelength. For KCWI pairs, background spectra were restricted to observed wavelengths where all 24 slices were sensitive i.e., 3530 – 5530 Å for the KCWI configuration we used. For the LRIS spectra, similar wavelength cuts were imposed both in the short and long wavelength ends of the blue channel data. The Ly $\alpha$  forest is primarily responsible for noise at the short wavelength end, while the LRIS dichroic cutoff at  $\sim 5600$  Å and the sky subtraction residuals around [O I]  $\lambda 5577$  occasionally introduce undulations in the red end of the blue channel. As for the KCWI spectra, 3500 – 5555 Å turned out to be a good fiducial wavelength to mitigate both effects. In addition to the wavelength end-

points, spectral regions near Ly $\alpha$  in the background galaxy spectrum were masked to avoid contamination in the final stack.<sup>3</sup>

In order to give each background spectrum an approximately equal weight in the composite, each spectrum was normalized with a cubic spline. The spline knots used to fit the background spectrum were chosen via a sparsely sampled median, ignoring wavelength regions near resonance lines. In the Ly $\alpha$  forest, we found points  $1\sigma$  above the local ( $\Delta\lambda \approx 50$  Å) median reliably traced the suppressed continuum. The KCWI and LM1 observations have associated error spectra; for the LRIS galaxies where error spectra do not always exist, we use the local standard deviation of the spectrum to construct a coarse error spectrum. We only allow spectral regions where the cubic spline fit is greater than the error spectrum to contribute to the stack. One could think of this requirement as effectively a  $S/N \gtrsim 1$  cut on all constituent background spectra. Background spectra where less than 15% of the bandpass had continuum  $S/N \gtrsim 1$  were excluded entirely to avoid adding patches of sporadic noise to the stack.

In stacking, each normalized background galaxy spectrum was shifted to the rest frame of its corresponding foreground galaxy and resampled onto a common wavelength grid with 0.2 Å sampling using linear interpolation. For a given range of  $D_{\text{tran}}$ , the associated background spectra were combined to make a final stack using a trimmed mean where spectral pixels above (below) the 95th (5th) percentile were rejected. For the stacks presented below, this resulted in 4 – 6 objects being excluded, comparable to a  $\sim 2\sigma$  clipped average, where  $\sigma$  is defined based on the variance of the input spectra at a given wavelength. Further details on the stacking method are described in Appendix C. Even with stacks of coarsely normalized spectra, the fact that each background spectrum has been shifted to an unrelated foreground redshift necessitates a manual continuum fit to the composite in order to extract accurate absorption profiles (discussed further in Appendix B).

As highlighted above, error spectra for KCWI and LM1 masks exist and can be propagated through to the stacks; however, we adopt a bootstrap approach since it includes sample variance and reveals how much individual spectra contribute to the absorption observed in the combined spectrum. For each background stack, we ran 100 bootstrap realizations with randomly selected galaxy pairs (with replacement) from that bin’s range of  $D_{\text{tran}}$ . The error spectrum is then the standard deviation of the 100 bootstrap stacks. As expected, the error spectra qualitatively resemble those propagated from each spectrum’s respective noise estimated by

<sup>3</sup> We experimented with masking other far-UV absorption features (e.g. C IV, Si II) but found that additional wavelength masks added more discontinuities to the constituent spectra and resulted in overall noisier stacks.

the DRP, but there tends to be a spike in variability around strong absorption features due to the variance in foreground absorption between galaxies.

Foreground galaxy spectra were combined in a similar fashion to their background galaxy counterparts, with a few notable exceptions. To ensure every foreground galaxy had a roughly equal contribution to the stack, each spectrum was approximately normalized based on its median continuum (1410 – 1510 Å) flux density before being combined. Each spectrum with a continuum  $S/N \gtrsim 1$  was then shifted to its rest frame and galaxies within the 5th – 95th percentiles (as a function of wavelength) were averaged. The final stack was normalized with a BPASSv2.2 (Stanway & Eldridge 2018) constant star formation rate stellar continuum model with age  $10^8$  years, metallicity  $Z = 0.14 Z_{\odot}$ , and SMC extinction curve<sup>4</sup>. More details on the choice of model and fitting procedure can be found in Steidel et al. (2016, 2018) and Theios et al. (2019).

Stacks from several  $D_{\text{tran}}$  bins are shown in Figure 4, offset from one another for clarity. We observe prominent Ly $\alpha$  and C IV over the widest range of impact parameters, plus Si III, Si IV, Si II  $\lambda 1260$ , and Si II  $\lambda 1526$  primarily in the small impact parameter bin ( $\langle D_{\text{tran}} \rangle = 50$  kpc; green spectrum). The number of objects contributing to the final stack varies by a factor of  $\sim 2$ , largely due to the underlying redshift distribution ( $1.4 \lesssim z_{\text{fg}} \lesssim 3.72$ ; see the right panel of Figure 2) and the short wavelength UV cutoff of the spectrometer ( $\sim 3500$  Å). As one moves to higher foreground redshifts, correspondingly higher redshift background objects are required to measure shorter wavelength transitions (e.g. Si III  $\lambda 1206$ ) which invariably fall in the Ly $\alpha$  forest of the background spectrum. The noise level is also somewhat higher at the short wavelength end of the spectrum as compared with a region around e.g. 1500 Å because many of the spectra cut off at shorter wavelengths and fewer pairs end up being averaged. There is also some small scale variability in the number of spectra contributing at a particular wavelength that arises from trimming and/or particular background spectral features being masked.

#### 4. ABSORPTION TRENDS FROM COMPOSITE SPECTRA

With a method for stacking galaxy pairs in hand, we proceed to construct a suite of composite spectra for  $D_{\text{tran}}$  between 8 kpc (the minimum pair separation) and 250 kpc, with the goal of sampling the changing absorption profiles over increasing galactocentric radius. Bins sampling projected distances  $D_{\text{tran}} \lesssim 100$  kpc are typically 30 kpc wide and are spaced in 10 kpc intervals (i.e. 8 – 40 kpc<sup>5</sup>, 20 – 50 kpc,

..., 100 – 130 kpc). The number of pairs contributing to a particular stack ranges from  $\sim 50$  at  $D_{\text{tran}} \simeq 30$  kpc to  $\sim 200$  at  $D_{\text{tran}} \simeq 100$  kpc which ensures any supposed absorption is real and easily discernible (Appendix C). As an illustration, Ly $\alpha$  and C IV absorption in several such stacks is shown in Figure 5; we will revisit these spectra in Section 4.1. These bins are not unique however; choosing different bin endpoints and/or spacing does not significantly alter the results presented below because the underlying distribution being sampled is the same.

Since the number of pairs increases with  $D_{\text{tran}}$  (Figure 2), it becomes possible to sample smaller impact parameter intervals while maintaining a comparable continuum  $S/N$ . On the other hand, the absorption features become weaker and less variable outside of the virial radius ( $R_{\text{vir}} \simeq 90$  kpc for a typical halo in our sample). As a compromise, for  $100 \lesssim D_{\text{tran}}/\text{kpc} < 250$  we maintain 30 kpc bins but increase the spacing to 15 kpc (i.e. 115 – 145 kpc, 130 – 160 kpc, ..., 220 – 250 kpc). The 10–15 kpc spacing between the bins means that every other or every third bin contains a unique set of background/foreground pairs or, depending on  $D_{\text{tran}}$ , at least  $\sim 30 - 50\%$  of the pairs differ between adjacent bins. The benefit to this “moving average” type sampling is a reduced susceptibility to outlier spectra and an increased resolution at small  $D_{\text{tran}}$ . We use these bins for the majority of the analysis with the full pair sample and specify for cases where the binning differs.

The composites lack the spectral resolution for a meaningful Voigt profile decomposition so we opted for model-independent representations of the absorption profiles. For each absorption line profile, we measured  $W_{\lambda}$ , velocity centroids ( $\Delta v$ ), and second moments ( $\sigma$ ) as a proxy for the velocity dispersion. For the DTB composite, each quantity was computed via direct integration over the region where the flux was below the continuum.<sup>6</sup> The  $D_{\text{tran}} \geq 8$  kpc composites have comparatively lower continuum  $S/N$  so each metric was instead computed over the range  $|v| \leq 700$  km s<sup>-1</sup>.<sup>7</sup> Since the background galaxy spectra ( $D_{\text{tran}} \geq 8$  kpc) measure absorption throughout the foreground galaxy halo and DTB spectra probe only gas “in front” of the galaxy along our line of sight, we corrected the DTB  $W_{\lambda}$  and  $\sigma$  by multiplying the observed DTB quantities by a factor of two (Table

<sup>6</sup> At this spectral resolution, the DTB  $\sigma(\text{C II})$  measurement is contaminated by the presence of the associated nonresonant C II\*  $\lambda 1335.62$  emission line which “fills in” the red side of the absorption feature. To compensate, we fit a double Gaussian to both features and define  $\sigma(\text{C II})$  as the standard deviation of the Gaussian absorption component.

<sup>7</sup> Given their close proximity, the integration region for O I  $\lambda 1302.2$  and Si II  $\lambda 1304.4$  was truncated at  $\lambda = 1303.3$  Å, the midpoint between the two features. Note that measuring the  $D_{\text{tran}} > 0$  kpc composites in the same manner as the DTB spectra increases the overall noise but does not significantly alter the results presented below.

<sup>4</sup>  $A_V = 2.74 E(B - V)$  for the SMC extinction curve.

<sup>5</sup> All but one of the foreground-background pairs have  $D_{\text{tran}} > 10$  kpc.



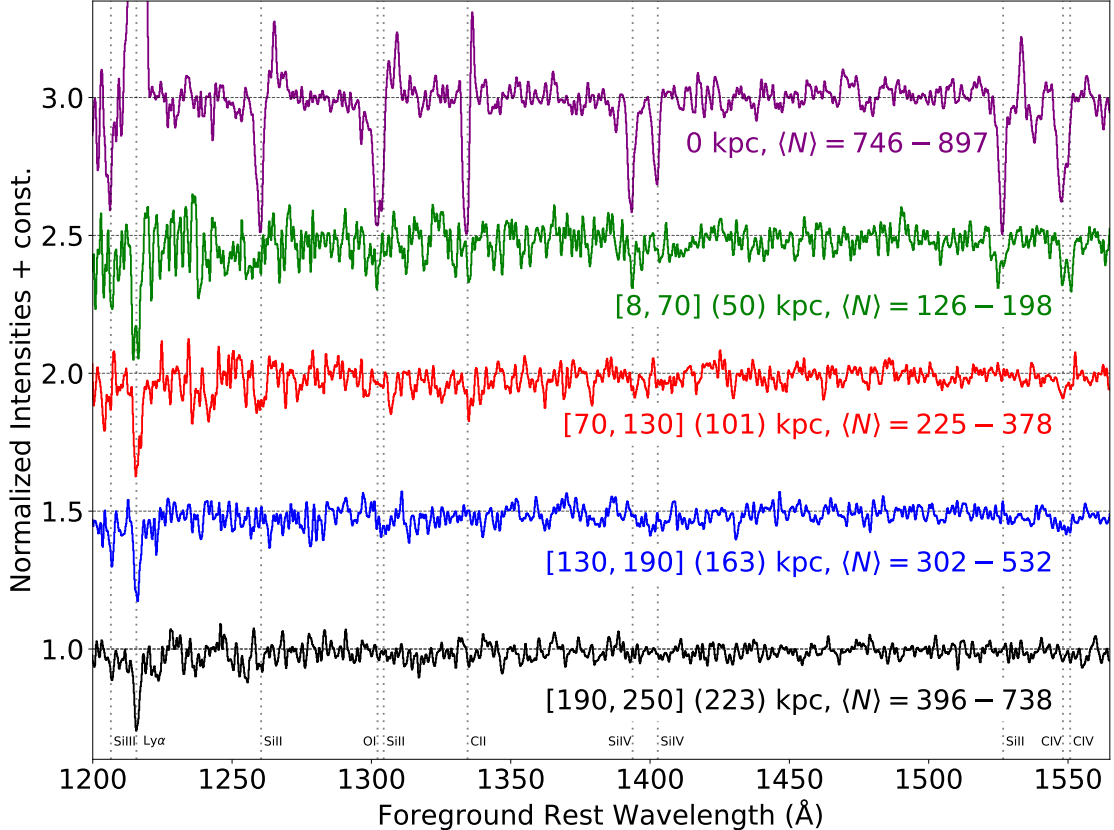


**Figure 4.** Normalized composite spectra of the foreground galaxies in this sample when viewed down the barrel (top, purple) plus four  $D_{\text{tran}}$  bins ranging from 8 – 250 kpc utilizing background galaxies as a continuum source. The spectra are offset by 0.5 from one another for ease of visualization. Each spectrum’s minimum, maximum, and median (shown in parentheses) sampled  $D_{\text{tran}}$  is labeled in the plot along with the number of pairs contributing to each stack. Note that the number of pairs varies as a function of wavelength with fewer pairs contributing at shorter wavelengths. The two counts specify the number of pairs contributing at  $\text{Ly}\alpha$  and C IV respectively. Typical far-UV resonant transitions are marked with vertical dotted lines and labeled at the bottom of the plot.

1) to approximate the total absorption and velocity spread that would be observed along a line of sight at  $D_{\text{tran}} = 0$  kpc. Similar to the background error spectrum calculation, we ran 2000 Monte Carlo resamples of the stacked spectrum perturbed by a Gaussian whose width was equal to the pixel noise level at each wavelength. Uncertainties on  $W_\lambda$ ,  $\Delta v$ , and  $\sigma$  were determined from the standard deviation of the resulting parameter distributions. Absorption line  $W_\lambda$ ,  $\sigma$ , and  $\Delta v$ , all as functions of  $D_{\text{tran}}$  can be seen in Figures 6, 7, and 8, respectively. These figures comprise the principal results of this study, and we will discuss them further in Sections 4.1 and 4.2.

We note that a few of the low ionization lines are detected in only a subset of the  $D_{\text{tran}}$  bins, leading to some nonuniform sampling. In general, if low ions or  $\text{Ly}\alpha$  are detected in a stack, then C IV tends to be as well simply because there is a factor of  $\approx 2$  increase in the number of pairs contributing to a stack between  $\text{Ly}\alpha$  and C IV (recall the  $S/N$  is roughly proportional to the number of pairs being averaged). The

net result is that  $\text{Ly}\alpha$  and C IV have the densest sampling in  $D_{\text{tran}}$ , especially at  $D_{\text{tran}} \lesssim 100$  kpc since bins where the low ionization features are detected can almost always be reused to measure  $\text{Ly}\alpha$  or C IV.

Before interpreting the stacked spectra and their derivatives, we first seek to establish the resolution of the composite spectra. As discussed in Section 3, 1406/2738 ( $f_{\text{neb}} = 51\%$ ) of the foreground galaxies in each galaxy pair have nebular redshift measurements i.e. velocity uncertainties  $\sigma_{\text{neb}} \approx 18$  km s $^{-1}$  (see Steidel et al. 2014); the remaining 1332 pairs ( $f_{\text{UV}} = 49\%$ ) have uncertainties  $\sigma_{\text{UV}} \approx 100$  km s $^{-1}$  (see Steidel et al. 2018; Chen et al. 2020). Combining the two velocity errors in quadrature weighted by their fractional contribution i.e.

$$\delta v_{\text{sys}} = \sqrt{f_{\text{neb}}\sigma_{\text{neb}}^2 + f_{\text{UV}}\sigma_{\text{UV}}^2} \quad (1)$$

implies the full galaxy pair sample has a systemic velocity uncertainty  $\delta v_{\text{sys}} \approx 73$  km s $^{-1}$ . Within  $D_{\text{tran}} < 100$  kpc, where KCWI pairs dominate the count,  $\delta v_{\text{sys}} \approx 79$  km s $^{-1}$ .

We compare the typical systematic error to the effective resolution of each stack. In a similar fashion to Equation 1,

$$\sigma_{\text{comb}} = \sqrt{f_{\text{LRIS}}\sigma_{\text{LRIS}}^2 + f_{\text{KCWI}}\sigma_{\text{KCWI}}^2} \quad (2)$$

where  $f_{\text{LRIS}}$  and  $f_{\text{KCWI}}$  are the fractional contributions of background spectra from each instrument to the total stack and  $\sigma_{\text{inst}}$  are the respective spectral resolutions. For the 600 line  $\text{mm}^{-1}$  grism, we adopt  $\sigma_{\text{LRIS}} = 107 \text{ km s}^{-1}$  ( $\langle R \rangle \simeq 1200$ ; Chen et al. 2020), and for KCWI we use  $\sigma_{\text{KCWI}} = 71 \text{ km s}^{-1}$ , consistent with a spectral resolution  $\langle R \rangle \simeq 1800$ . For the full  $D_{\text{tran}} < 250 \text{ kpc}$  sample,  $\sigma_{\text{comb}} \approx 102 \text{ km s}^{-1}$ , and for  $D_{\text{tran}} < 100 \text{ kpc}$ ,  $\sigma_{\text{comb}} \approx 67 \text{ km s}^{-1}$ .

Combining the two sources of error in quadrature, we find  $\sigma_{\text{tot}} = \sqrt{\delta v_{\text{sys}}^2 + \sigma_{\text{comb}}^2} \approx 125 \text{ km s}^{-1}$  for the full sample and  $\sigma_{\text{tot}} \approx 104 \text{ km s}^{-1}$  at  $D_{\text{tran}} < 100 \text{ kpc}$ . This calculation shows that we are unable to distinguish spectral features with velocity separations less than  $\approx 125 \text{ km s}^{-1}$  in the composites. With these numbers in mind, we proceed to discuss absorption feature morphology for the various rest-UV transitions.

#### 4.1. Ly $\alpha$ and C IV

Ly $\alpha$  and C IV (in that order) are by far the strongest absorption features detected in the composite spectra of background galaxies. We therefore present these results before moving onto the low ions. Starting in one dimension, some representative stacks are presented in Figure 5 that show how Ly $\alpha$  (left) and C IV (right) change with  $D_{\text{tran}}$ . The same  $D_{\text{tran}}$  bins are shown for ease of comparison, although as can be seen in, e.g., Figure 4, excess Ly $\alpha$  absorption extends well beyond  $D_{\text{tran}} = 100 \text{ kpc}$ . For Ly $\alpha$  and C IV, absorption starts out both stronger and more extended in velocity close to the center of the galaxy and the profiles become shallower and narrower with increasing  $D_{\text{tran}}$ . Between  $D_{\text{tran}} \simeq 30 \text{ kpc}$  and  $D_{\text{tran}} \simeq 100 \text{ kpc}$ ,  $W_{\lambda}(\text{Ly}\alpha)$  drops by a factor of  $\simeq 2$  from  $2 \text{ \AA}$  to  $1 \text{ \AA}$  (Figure 6) and  $\sigma(\text{Ly}\alpha)$  decreases from  $370 \text{ km s}^{-1}$  to  $300 \text{ km s}^{-1}$ ; a 23% reduction (Figure 7). In the same range of projected distances,  $W_{\lambda}(\text{C IV})$  drops by a factor of  $\simeq 2$  from  $1.0 \text{ \AA}$  to  $0.5 \text{ \AA}$ , while  $\sigma(\text{C IV})$  remains approximately constant at  $\simeq 400 \text{ km s}^{-1}$ . In this case,  $W_{\lambda}(\text{C IV})$  and  $\sigma(\text{C IV})$  were measured via direct integration over the full doublet, without distinguishing between the individual transitions.

For Ly $\alpha$  in the left panel of Figure 5 (see also Figure 8), we observe a shifting velocity centroid with  $D_{\text{tran}}$ : at  $D_{\text{tran}} \lesssim 50 \text{ kpc}$ ,  $\Delta v(\text{Ly}\alpha) < 0 \text{ km s}^{-1}$ ; between  $D_{\text{tran}} \sim 50 - 125 \text{ kpc}$ ,  $\Delta v(\text{Ly}\alpha) \simeq 100 \text{ km s}^{-1}$ , after which point  $\Delta v(\text{Ly}\alpha)$  is consistent with zero. We note that the relative scarcity of galaxy pairs within  $\simeq 100 \text{ kpc}$  results in noisier stacks compared with those at  $\langle D_{\text{tran}} \rangle \gtrsim 100 \text{ kpc}$  where more lines of sight are probed. This can be seen by comparing the dotted

red and dotted purple error spectra; the former has fewer (37) pairs contributing than the latter (116) and the corresponding bootstrap uncertainty is increased by a factor of  $\simeq 2$ . Despite the larger uncertainty in absorption strength, the shifted trough persists across multiple independent bins. We discuss the net blueshifted velocity centroid at  $D_{\text{tran}} \lesssim 50 \text{ kpc}$  further in Appendix D.

While both Ly $\alpha$  and C IV present a similar trend in decreasing  $W_{\lambda}$  and  $\sigma$  with increasing  $D_{\text{tran}}$ , the shape of the C IV absorption troughs changes more significantly. In the  $D_{\text{tran}} = 8 - 40 \text{ kpc}$  bin (right panel of Figure 5), both C IV  $\lambda 1548$  and C IV  $\lambda 1550$  present strong absorption near the systemic velocity with an extended trough in velocity space out to  $v_{\text{LOS}} \simeq -300 \text{ km s}^{-1}$  in C IV  $\lambda 1548$ , and  $v_{\text{LOS}} \simeq +300 \text{ km s}^{-1}$  in C IV  $\lambda 1550$ . We note that  $W_{\lambda}(1550)$  is at least a factor of two larger than  $W_{\lambda}(1548)$  which would of course be unphysical if one were measuring a single absorbing complex. In Appendix B, we use stacked HIRES spectra of background QSOs to show how such foreground absorption profiles can arise. The subsequent bins in Figure 5 show a contracting velocity spread centered near zero velocity and an increasing  $W_{\lambda}(1548)/W_{\lambda}(1550)$  ratio, approaching the DTB presentation. As an example, between  $D_{\text{tran}} \simeq 28 \text{ kpc}$  and  $D_{\text{tran}} \simeq 48 \text{ kpc}$ ,  $W_{\lambda}(1550)$  diminishes by  $\sim 25\%$  and the velocity dispersion reduces slightly from  $400 \text{ km s}^{-1}$  to  $350 \text{ km s}^{-1}$ .

We used the  $W_{\lambda}(1548)/W_{\lambda}(1550)$  ratio and  $\Delta v(\text{C IV})$  to estimate the change in  $\tau(\text{C IV})$  with  $D_{\text{tran}}$ . Figure 9 shows  $W_{\lambda}(1548)/W_{\lambda}(1550)$  measured via direct integration in each  $D_{\text{tran}}$  bin. The midpoint between C IV  $\lambda 1548$  and C IV  $\lambda 1550$  ( $v(1548) \approx 250 \text{ km s}^{-1}$ ) is used to separate the two doublet components. Between  $D_{\text{tran}} \simeq 40 \text{ kpc}$  and  $D_{\text{tran}} \simeq 90 \text{ kpc}$ , the average  $W_{\lambda}(1548)/W_{\lambda}(1550)$  ratio transitions from one to two. When  $\sigma(\text{C IV})$  is large, a more robust approach to measuring the gas opacity involves the overall velocity centroid ( $\Delta v(\text{C IV})$ ) integrating over the full doublet. Measuring the velocity offset from  $\lambda_{\text{cent}} = 1549.480 \text{ \AA}$  (the average of the two C IV rest wavelengths), we would theoretically expect a velocity centroid of  $\Delta v \simeq -90 \text{ km s}^{-1}$  for optically thin C IV absorption with  $W_{\lambda}(1548)/W_{\lambda}(1550) = 2$ . Naturally, the velocity centroid would be centered at  $\Delta v = 0 \text{ km s}^{-1}$  for the optically thick doublet ( $W_{\lambda}(1548)/W_{\lambda}(1550) = 1$ ).

Between  $D_{\text{tran}} \simeq 30 \text{ kpc}$  and  $D_{\text{tran}} \simeq 100 \text{ kpc}$ ,  $\Delta v(\text{C IV})$  blueshifts by  $\simeq 300 \text{ km s}^{-1}$  from  $\Delta v(\text{C IV}) \simeq +200 \text{ km s}^{-1}$  to  $\Delta v(\text{C IV}) \simeq -100 \text{ km s}^{-1}$  (Figure 8). The majority of the C IV bins show  $\Delta v \lesssim -90 \text{ km s}^{-1}$  beyond  $D_{\text{tran}} \simeq 60 \text{ kpc}$  and the average  $W_{\lambda}(1548)/W_{\lambda}(1550)$  changes from a 1:1 to a 2:1 ratio (Figure 9), consistent with a transition from optically thick to optically thin gas with increasing  $D_{\text{tran}}$ . The gradient in line strength is largest at  $D_{\text{tran}} \simeq 50 \text{ kpc}$ , but the noise in both  $\Delta v(\text{C IV})$  and  $W_{\lambda}(1548)/W_{\lambda}(1550)$  at

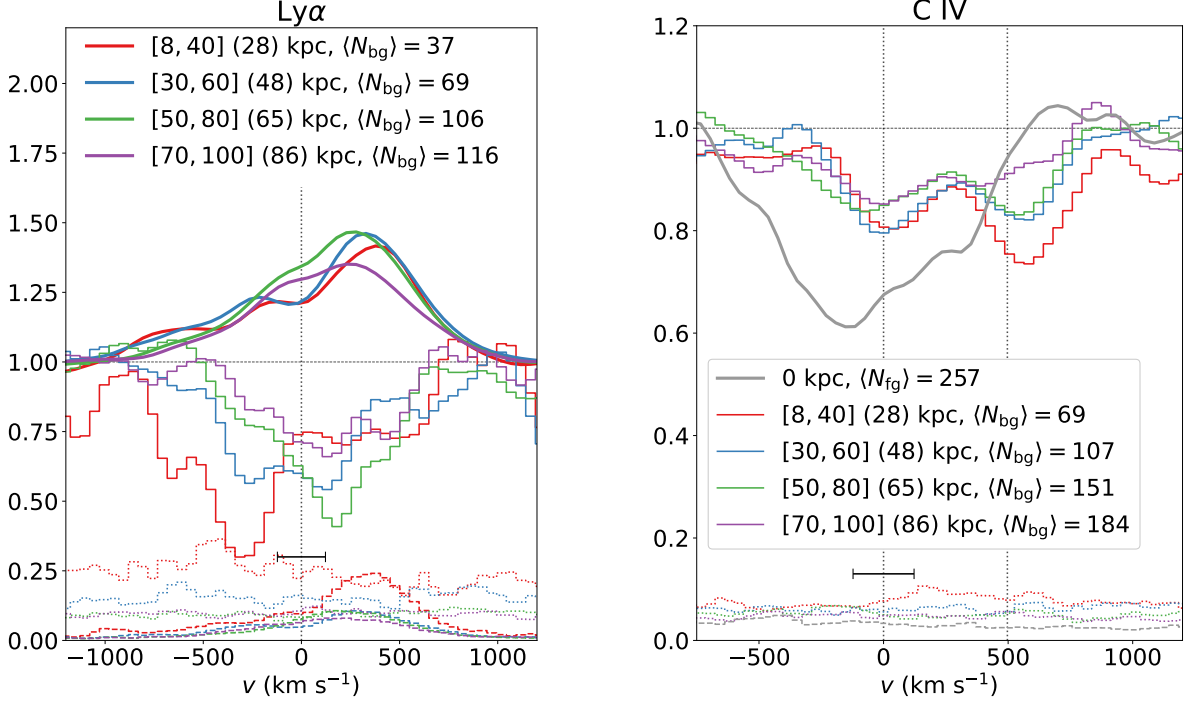


**Figure 5.** *Left:* Normalized and scaled Ly $\alpha$  emission (thick line style;  $D_{\text{tran}} = 0$  kpc) and absorption (thin histogram line style;  $D_{\text{tran}} > 0$  kpc) profiles plotted for several impact parameter bins. For a given impact parameter range, DTB foreground spectra were averaged to produce an emission spectrum while background spectra were similarly averaged to measure the absorption induced by the foreground galaxy’s CGM. The range of  $D_{\text{tran}}$  and the median are shown for each bin. Note that the Ly $\alpha$  emission is scaled down by a factor of 15 and translated vertically by +1 for display purposes. *Right:* C IV absorption profiles for the same bins in  $D_{\text{tran}}$  (with the same color scheme) as the left panel. The DTB (thick gray) spectrum includes all foreground galaxies in pairs with  $D_{\text{tran}} < 100$  kpc. In both panels, the number of pairs contributing to each stack at the wavelength of interest is shown in the plot legends; “fg” subscripts correspond to DTB spectra, while “bg” are measurements utilizing background spectra. The vertical dashed lines show  $v_{\text{sys}} = 0$   $\text{km s}^{-1}$  for each transition and the black error bar shows the effective resolution element of the stack. Note that C IV  $\lambda 1550$  is shown at  $v = 497$   $\text{km s}^{-1}$  on the right hand panel. Normalized background (DTB) error spectra from bootstrap resampling are plotted in a dotted (dashed) line style and are color coded to match the stacked spectra.

$50 \lesssim D_{\text{tran}}/\text{kpc} \lesssim 80$  kpc suggests that some optically thick C IV persists to  $D_{\text{tran}} \simeq 100$  kpc.

Beyond  $D_{\text{tran}} \simeq 100$  kpc, the C IV absorption signal becomes weaker and the marginal  $S/N$  prevents an accurate determination of  $W_\lambda(\text{C IV})$  ratios. Physically, the equivalent width ratio likely remains at or around two but the number of pairs in our sample is insufficient to distinguish C IV  $\lambda 1550$  from the continuum. Indeed, the consistently negative  $\Delta v(\text{C IV})$  values at  $D_{\text{tran}} \gtrsim 80$  kpc indicate that optically thin C IV is still present out to at least  $D_{\text{tran}} \simeq 125$  kpc; beyond this projected distance, the  $S/N$  is not sufficient to make a reliable velocity centroid measurement.

#### 4.2. Low Ions

In addition to Ly $\alpha$  and C IV, we attempted to measure additional far-UV low ionization interstellar absorption transitions in the stacked spectra. Figure 10 shows several far-UV transitions where the absorption profiles vary significantly with  $D_{\text{tran}}$  and provides a visualization of the changing  $W_\lambda$  and  $\sigma$  measured in Figures 6 and 7 respectively. As expected,

DTB ( $D_{\text{tran}} = 0$  kpc) absorption is considerably stronger for all transitions when compared with background galaxy sight-lines ( $D_{\text{tran}} > 10$  kpc). Among the  $D_{\text{tran}} > 10$  kpc spectra, the trend continues: absorption strength for all transitions decreases with  $D_{\text{tran}}$ . In particular, O I and Si IV show the largest change in both absorption strength and velocity extent over the other transitions.

The absorption line equivalent widths are reasonably well-fit by power laws in  $D_{\text{tran}}$ ; we show the best fit as a color coded dashed line in each of the subplots in Figure 6 and list the power law indices ( $\gamma$ ) in Table 1. As a group, the high ions (Si III, C IV, and Si IV) have shallower declines in  $W_\lambda$  with  $D_{\text{tran}}$  ( $\langle \gamma_{\text{high}} \rangle = -0.38$ ) compared to the low ions ( $\langle \gamma_{\text{low}} \rangle = -0.46$ ). C II, Si II, O I, and Ly $\alpha$  are all consistent with one another in their  $W_\lambda$  dependence (especially at  $D_{\text{tran}} \lesssim 100$  kpc) while weaker transitions like Al II and Si II  $\lambda 1526$  tend to fall off the fastest with projected distance. The exception to this trend is Si II  $\lambda 1260$  which tracks Si II  $\lambda 1526$  steadily until  $D_{\text{tran}} \simeq 50$  kpc but maintains a larger  $W_\lambda$  beyond that impact parameter.

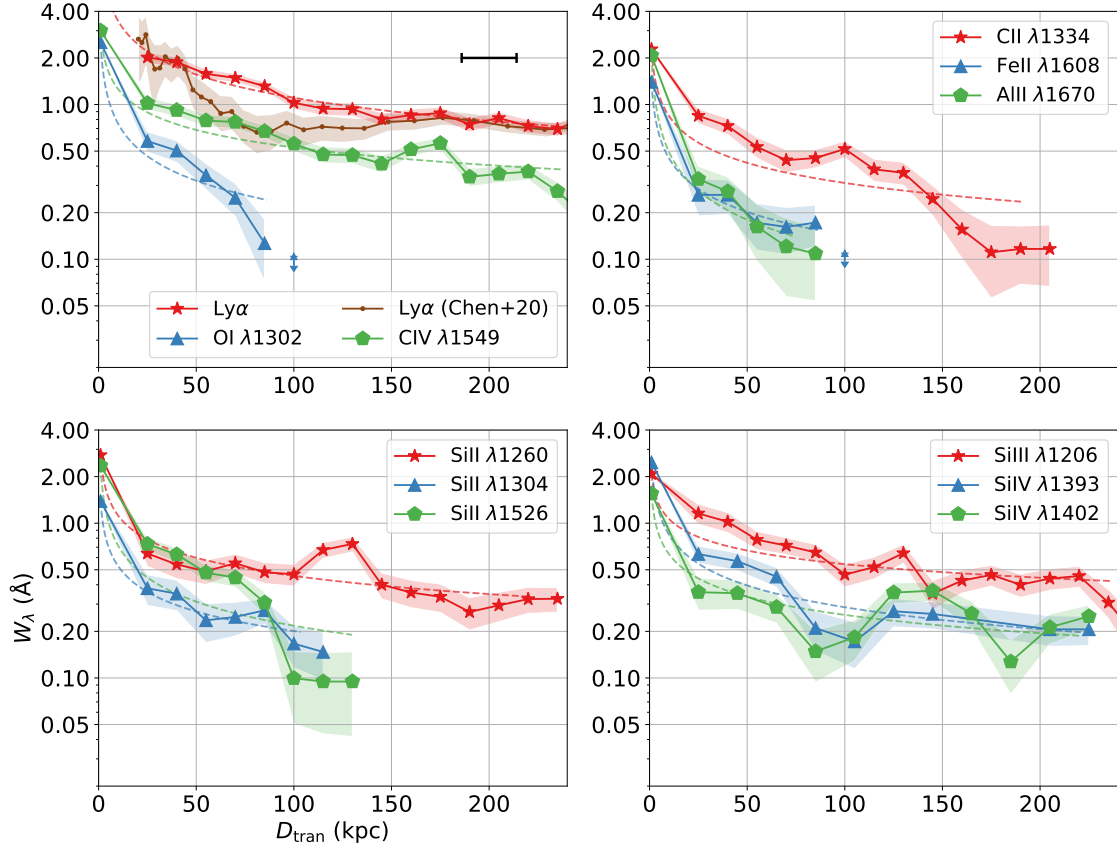


**Figure 6.** Absorption line  $W_\lambda$  vs.  $D_{\text{tran}}$  for several transitions (labeled in the plot legends). The green C IV  $\lambda$  1549 points show the total equivalent width integrating over the entire feature. Color coded bands show  $W_\lambda$  uncertainties and dashed lines correspond to power law fits of each respective transition ( $D_{\text{tran}} = 1$  kpc is used as an approximation for  $D_{\text{tran}} = 0$  kpc in the power law fit). In the top left plot, the horizontal error bar shows typical bin sizes for all the transitions shown. The [Chen et al. \(2020\)](#)  $W_\lambda$  ( $\text{Ly}\alpha$ ) measurements (with uncertainties) are shown in brown.

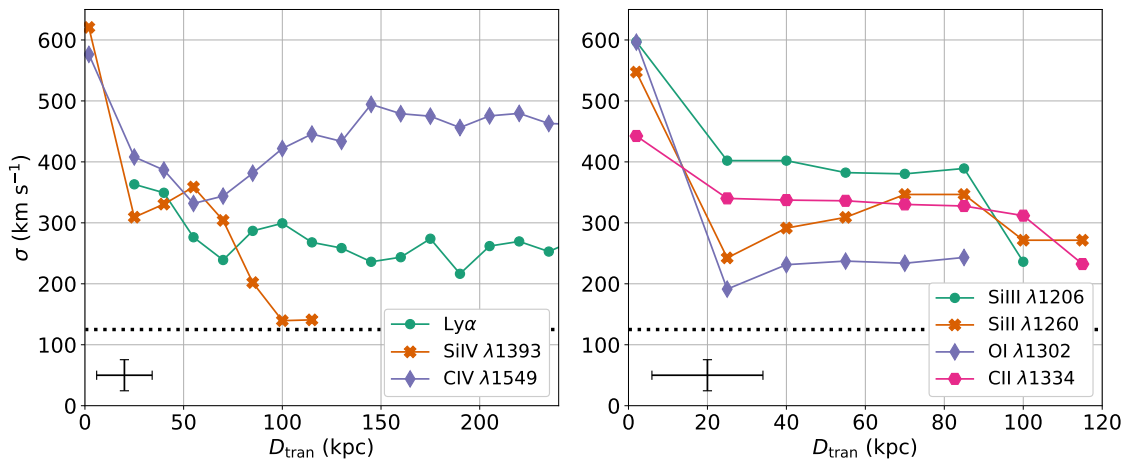


**Figure 7.** Second moment of the normalized absorption profiles ( $\sigma$ ) vs. projected distance ( $D_{\text{tran}}$ ) for transitions color coded in the legends of each panel. Like Figures 6 and 8, C IV  $\lambda$  1549 (thin purple diamonds) measurements are obtained by integrating over the entire doublet. The black error bar on the right side of each plot shows typical bin sizes (horizontal) and average bootstrap uncertainties on the second moment (vertical) for each transition. The black dotted horizontal line shows the effective velocity resolution element.

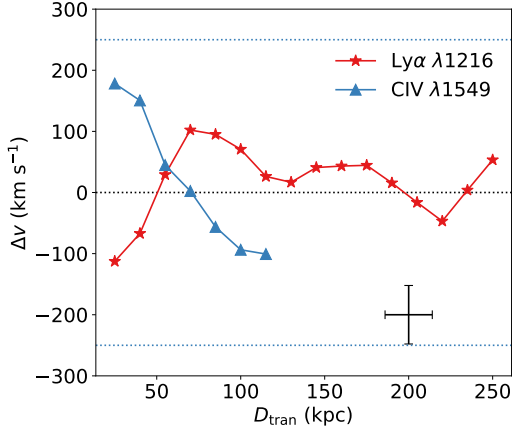


**Figure 8.** Ly $\alpha$  (red) and C IV (blue) velocity centroids ( $\Delta v$ ) as a function of  $D_{\text{tran}}$ . The C IV centroid was computed by integrating over the entire doublet and  $\Delta v(\text{C IV}) = 0 \text{ km s}^{-1}$  corresponds to the midpoint between the two C IV transitions ( $\lambda \approx 1549.480 \text{ \AA}$ ). The negative and positive dotted blue lines correspond to C IV  $\lambda 1548$  and C IV  $\lambda 1550$  plotted respectively in velocity space. The black error bar shows the average bin width and bootstrap error on the velocity centroid.

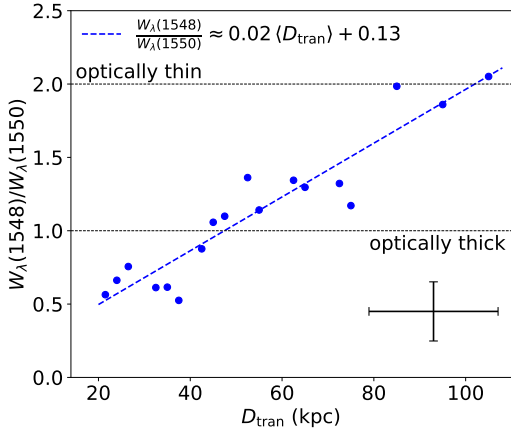


**Figure 9.** C IV equivalent width ratios as a function of projected distance with optically thick and thin regions plotted. The black error bar in the bottom right gives the average bin size and the fractional uncertainty in the  $W_\lambda$  measurement from bootstrap resampling. The blue dashed line is a linear fit to the  $W_\lambda(1548)/W_\lambda(1550)$  ratios.

We compare the Si II  $\lambda 1260$  and Si II  $\lambda 1526$   $W_\lambda$  ratios to see how Si II optical depth varies with  $D_{\text{tran}}$ . Down the barrel,  $W_\lambda(1260)/W_\lambda(1526) = 1$  (Table 1) implying both Si II  $\lambda 1260$  and Si II  $\lambda 1526$  are strongly saturated. However, the DTB spectra in the top left panel of Figure 11 show a divergence of velocities between Si II  $\lambda 1260$  (green) and Si II  $\lambda 1526$  (orange) on the blue side of the line suggesting that high velocity outflowing gas may be less strongly

**Table 1.** DTB Equivalent Width Measurements and Power Law Fits<sup>a</sup>

Line	$\lambda$ ( $\text{\AA}$ )	$W_\lambda^b$ ( $\text{\AA}$ )	$W_{\lambda, \text{corr}}^c$ ( $\text{\AA}$ )	$\gamma^d$
Si III	1206.51	$1.09 \pm 0.06$	$2.19 \pm 0.12$	$-0.30 \pm 0.02$
Ly $\alpha$	1215.67	...	$(10.87 \pm 1.16)$	$-0.50 \pm 0.03$
Si II	1260.42	$1.38 \pm 0.03$	$2.75 \pm 0.06$	$-0.39 \pm 0.01$
O I	1302.2	$1.00 \pm 0.02^e$	$2.01 \pm 0.05$	$-0.47 \pm 0.04$
Si II	1304.4	$1.16 \pm 0.02^e$	$2.31 \pm 0.05$	$-0.54 \pm 0.01$
C II	1334.53	$1.16 \pm 0.02$	$2.31 \pm 0.05$	$-0.44 \pm 0.03$
Si IV	1393.76	$1.23 \pm 0.02$	$2.47 \pm 0.04$	$-0.47 \pm 0.02$
Si IV	1402.77	$0.78 \pm 0.02$	$1.55 \pm 0.04$	$-0.39 \pm 0.02$
Si II	1526.72	$1.39 \pm 0.02$	$2.77 \pm 0.04$	$-0.56 \pm 0.05$
C IV	1549.0	$1.50 \pm 0.02$	$3.00 \pm 0.05$	$-0.38 \pm 0.01$
Fe II	1608.45	$0.70 \pm 0.02$	$1.40 \pm 0.04$	$-0.49 \pm 0.01$
Al II	1670.81	$1.02 \pm 0.03$	$2.04 \pm 0.05$	$-0.62 \pm 0.02$

NOTE—

<sup>a</sup> The full set of foreground galaxies in this sample have median stellar mass  $\log(M_*/M_\odot) = 9.6 \pm 0.8$  (Figure 3).

<sup>b</sup>  $W_\lambda$  are measured equivalent widths from DTB spectra ( $D_{\text{tran}} = 0$  kpc).

<sup>c</sup>  $W_{\lambda, \text{corr}}$  are corrected equivalent widths assuming one is looking through a full halo endowed with a symmetric velocity distribution (i.e.  $W_{\lambda, \text{corr}} = 2W_\lambda$ ). The DTB  $W_{\lambda, \text{corr}}$  are used in Figure 6.  $W_{\lambda, \text{corr}}(\text{Ly}\alpha)$  is extrapolated from the power law fit.

<sup>d</sup> Best fit power law indices for the  $W_\lambda$  fits shown in Figure 6. Each fit is normalized such that  $W_{\lambda, \text{fit}} = W_{\lambda, \text{corr}} \left( \frac{D_{\text{tran}}}{1 \text{ kpc}} \right)^\gamma$ .

<sup>e</sup> At the spectral resolution of the sample, the DTB O I  $\lambda 1302.2$  and Si II  $\lambda 1304.4$  lines are blended. We measure  $W_\lambda(1304.4)$  by scaling the Si II  $\lambda 1260$  profile to the red wing of the Si II  $\lambda 1304.4$  absorption feature;  $W_\lambda(1302.2)$  is computed by subtracting off the scaled Si II  $\lambda 1260$  profile from the blended (O I + Si II) profile and measuring the residual absorption.

<sup>f</sup>  $W_\lambda(\text{C IV})$  is computed by integrating over the full doublet.

saturated than gas at  $\Delta v \gtrsim -200 \text{ km s}^{-1}$ . Comparing  $W_\lambda(1260)$  and  $W_\lambda(1526)$  with  $D_{\text{tran}}$  (see Figures 6 and 11), we find Si II remains saturated through  $D_{\text{tran}} \simeq 50$  kpc, at which point  $W_\lambda(1526)$  begins to fall off more rapidly than  $W_\lambda(1260)$ . At  $D_{\text{tran}} \simeq 75$  kpc,  $W_\lambda(1260)/W_\lambda(1526) \approx 2$  ( $\tau(1526) \simeq 1.7$ , assuming the flat part of the curve of growth). We note that  $W_\lambda(1260)/W_\lambda(1526) = 6.25$  in the optically thin limit so beyond  $D_{\text{tran}} \simeq 100$  kpc, Si II  $\lambda 1526$  is unsaturated and we measure an optically thin Si II column density of  $\log(N(\text{Si II})/\text{cm}^{-2}) \simeq 12.9$ . We lack sufficient  $S/N$  to measure both transitions beyond  $D_{\text{tran}} \simeq 125$  kpc.

Figures 10 and 11 provide two complementary views on how each ion evolves with  $D_{\text{tran}}$  and how the profiles between transitions compare. While all lines show a decrease in absorption strength and velocity dispersion with increas-

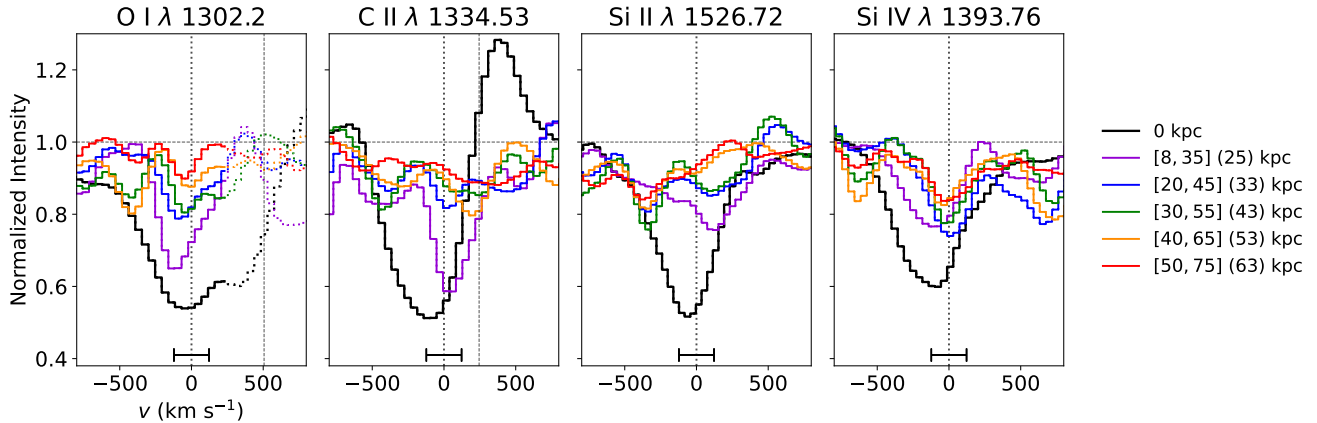


**Figure 10.** Normalized intensity profiles for several strong far-UV transitions, measured DTB (thick black) and at  $D_{\text{tran}}$  between 8 and 75 kpc (median  $D_{\text{tran}}$  shown in parentheses). The legend specifies the map between line color and range of  $D_{\text{tran}}$ . The plotted colors move from blue to red across the rainbow with increasing  $D_{\text{tran}}$  e.g.,  $D_{\text{tran}} \simeq 25$  kpc is blue and  $D_{\text{tran}} \simeq 63$  kpc is red. Black vertical dotted lines show  $v_{\text{sys}}$  and dashed lines show nearby transitions where appropriate (Si II  $\lambda 1304.4$  and C II\*  $\lambda 1335$ ). Regions of the spectrum contaminated by such nearby transitions are shown with a dotted line style. The black error bar shows the effective velocity resolution. This figure is in contrast to Figure 11 which shows different transitions within the same bin.

ing  $D_{\text{tran}}$ , the higher ionization lines like C IV and Si IV have a slightly broader velocity range at all  $D_{\text{tran}}$  than observed for O I and C II. Unlike the other transitions, Si IV has an extended red wing that extends to  $v_{\text{LOS}} \simeq 700$  km s $^{-1}$  for  $D_{\text{tran}} \lesssim 50$  kpc and similar to C IV,  $W_{\lambda}(1393)/W_{\lambda}(1402)$  increases with  $D_{\text{tran}}$  as  $N(\text{Si IV})$  decreases. The dichotomy between lower and higher ionization species is in agreement with previous QSO studies (see e.g. Rauch et al. 2001; Rudie et al. 2019) which have shown that higher ionization species probe a wider range of both  $N_{\text{HI}}$  and velocity.

Like the DTB spectra, Figure 11 shows that the low and high ions share similar respective profiles. The velocity extent of the various metal lines agree to within  $\sim 100$  km s $^{-1}$  (the effective velocity resolution element) in the  $D_{\text{tran}} \simeq 32$  kpc bin and the amplitudes are consistent to within the bootstrap uncertainties. The decreasing absorption strength with  $D_{\text{tran}}$  makes this type of comparison more difficult at larger projected distances due to the reduced  $S/N$  in each line, so we restrict these plots to  $D_{\text{tran}} \lesssim 50$  kpc. Out of the low ionization lines, we find O I and C II show the best agreement with one another for  $D_{\text{tran}} \lesssim 50$  kpc.

#### 4.3. Binning by stellar population parameters

In addition to binning the foreground-background galaxy pairs by  $D_{\text{tran}}$ , we also considered how galaxy properties affect CGM absorption. Using SED measurements of the fore-

ground galaxies, we constructed subsamples based on  $M_*$ , SFR, sSFR, and  $E(B-V)$ . As discussed in Appendix C, the stacked spectra we construct are always “pair limited,” i.e., the  $S/N$  of the spectra and the corresponding ease of detecting absorption features are both proportional to the number of galaxies being averaged. For this reason, the  $D_{\text{tran}}$  sampling achievable with the SED-based subsamples is considerably coarser than what can be done with the full sample.

After some experimentation with various  $D_{\text{tran}}$  bins, we settled on three independent configurations:  $D_{\text{tran}} = 8 - 70$  kpc,  $70 - 100$  kpc, and  $100 - 250$  kpc which have median  $D_{\text{tran}}$  of 51 kpc, 86 kpc, and 188 kpc, respectively. The two inner bins contain 208 and 202 galaxy pairs respectively and the first was chosen to sample radii where C IV had been detected in the full stacks. Indeed, Ly $\alpha$  and C IV are the only two lines robustly detected both due to the relative weakness of the remaining far-UV features and the broad ranges of projected distances needed to produce moderately high  $S/N$  spectra, so we restrict our discussion to those features.

The distributions of SED-fit galaxy properties for this sample are shown in Figure 3. While the  $D_{\text{tran}} = 100 - 250$  kpc bin has  $\simeq 80\%$  of the total foreground galaxies and is thus representative of the full sample, the number of galaxies in the  $D_{\text{tran}} = 8 - 70$  kpc and  $D_{\text{tran}} = 70 - 100$  kpc bins is smaller by almost an order of magnitude with respect to the  $D_{\text{tran}} = 8 - 250$  kpc bin. That being said, the overall distributions of galaxy properties remain similar which gives us confidence that both of the inner subsamples span the same range of galaxy parameters and are representative of the full sample.

We split the four SED derived distributions in half at their median value, and constructed “low” and “high” subsam-

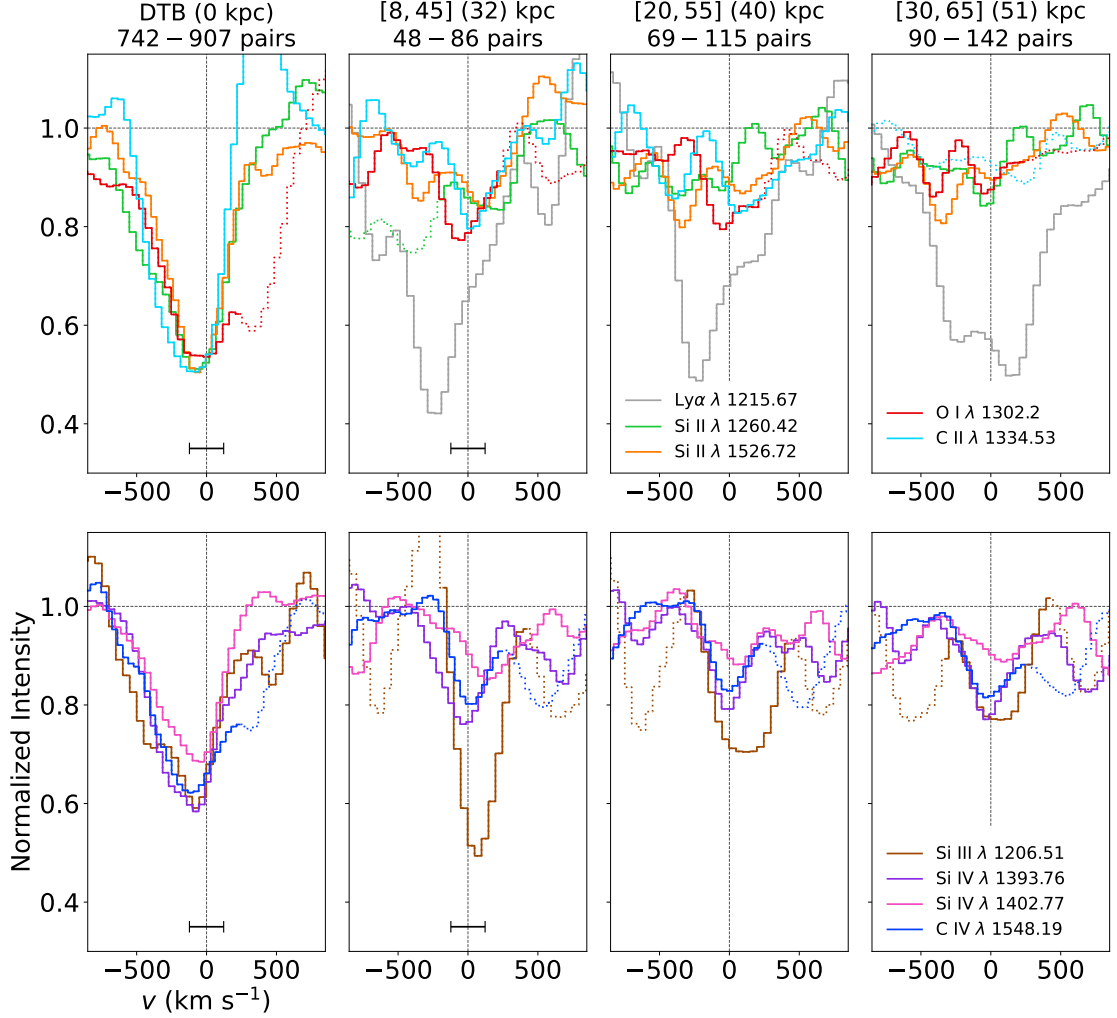


**Figure 11.** Normalized far-UV absorption features on a unified velocity scale for several different transitions DTB ( $D_{\text{tran}} = 0$  kpc) and at three nonzero projected distances (separated by column). The range of  $D_{\text{tran}}$  and number of galaxy pairs in that range are listed in the title in a similar format to previous figures. The ions being compared are shown in the legend. The vertical dashed line shows the systemic velocity of the foreground galaxy stack and the black error bar at the bottom shows the effective spectral resolution. Spectral regions contaminated by neighboring features are shown in a dotted line style. This plot differs from Figure 10 in that several transitions are being compared at a fixed  $D_{\text{tran}}$ , as opposed to comparing the effect of  $D_{\text{tran}}$  for a fixed transition.

ples; see the leftmost column of Table 2. Each subsample based on foreground galaxy properties spans approximately 1.5 dex in  $M_*$ , 1 dex in SFR and sSFR, and 0.1 magnitudes in  $E(B - V)$ . For each subsample, we followed the same procedure (see Section 3) as the full sample to construct stacked background galaxy spectra that contain foreground objects satisfying a particular galaxy property constraint (e.g.  $\log[\text{SFR}/(M_\odot \text{ yr}^{-1})] \leq 0.6$ ). These stacks were combined using a trimmed mean, renormalized, and line profile measurements were computed for  $\text{Ly}\alpha$  and C IV.  $W_\lambda$ ,  $\Delta v$ , and  $\sigma$  for each bin and absorption line are given in Tables 2, 3, and 4, respectively. Spectral cutouts of  $\text{Ly}\alpha$  and C IV for each galaxy property are shown in Figures 12–15. In each of the four figures, the top row of plots corresponds to spec-

tra from the  $D_{\text{tran}} = 8 - 70$  kpc bin, and the bottom has  $D_{\text{tran}} = 70 - 100$  kpc composites. Figure 16 shows the  $D_{\text{tran}} = 100 - 250$  kpc bin using a style similar to Figures 12–15, but since C IV becomes indistinguishable from the continuum for  $D_{\text{tran}} \gtrsim 100$  kpc, it is not significantly detected in this stack and we plot just the  $\text{Ly}\alpha$  absorption.

The most significant difference between subsamples is C IV absorption strength vs.  $M_*$ .  $W_\lambda(\text{C IV})$  in the high- $M_*$  subsample is a factor of  $\simeq 2$  greater than the low- $M_*$  bin for both ranges of  $D_{\text{tran}}$ . Given the difference of C IV strength in the two  $M_*$  subsamples, we split the sample in

**Table 2.** Absorption Strength ( $W_\lambda$ ) vs. Foreground Galaxy Properties

Composite <sup>a</sup>	Ly $\alpha$			C IV $\lambda$ 1549 <sup>b</sup>			
	[8, 70] (51) <sup>c</sup>	[70, 100] (86)	[100, 250] (188)	DTB <sup>d</sup>	[8, 70] (51)	[70, 100] (86)	[100, 250] (188)
	( $\text{\AA}$ )	( $\text{\AA}$ )	( $\text{\AA}$ )	( $\text{\AA}$ )	( $\text{\AA}$ )	( $\text{\AA}$ )	( $\text{\AA}$ )
$\log(M_*/M_\odot) = 9.0 \pm 0.5$	$0.85 \pm 0.20$	$1.03 \pm 0.14$	$0.63 \pm 0.07$	$1.77 \pm 0.03$	$0.47 \pm 0.10$	$0.71 \pm 0.09$	$0.23 \pm 0.05$
$\log(M_*/M_\odot) = 9.6 \pm 0.3$	$2.33 \pm 0.25$	$1.70 \pm 0.21$	$1.01 \pm 0.07$	$3.35 \pm 0.02$	$1.04 \pm 0.12$	$0.99 \pm 0.13$	$0.25 \pm 0.04$
$\log(M_*/M_\odot) = 10.2 \pm 0.4$	$1.74 \pm 0.22$	$2.21 \pm 0.16$	$0.80 \pm 0.08$	$3.69 \pm 0.02$	$1.65 \pm 0.11$	$0.99 \pm 0.11$	$0.44 \pm 0.04$
$\log[\text{SFR}/(M_\odot \text{ yr}^{-1})] = 0.6 \pm 0.3$	$1.82 \pm 0.19$	$1.31 \pm 0.14$	$0.74 \pm 0.06$	$2.35 \pm 0.02$	$0.75 \pm 0.09$	$0.86 \pm 0.08$	$0.43 \pm 0.03$
$\log[\text{SFR}/(M_\odot \text{ yr}^{-1})] = 1.2 \pm 0.3$	$1.36 \pm 0.15$	$1.15 \pm 0.14$	$0.77 \pm 0.05$	$3.75 \pm 0.01$	$1.13 \pm 0.09$	$0.98 \pm 0.10$	$0.31 \pm 0.03$
$\log(\text{sSFR}/\text{Gyr}^{-1}) = -0.2 \pm 0.4$	$1.62 \pm 0.19$	$1.27 \pm 0.15$	$0.76 \pm 0.06$	$3.24 \pm 0.02$	$0.90 \pm 0.08$	$0.59 \pm 0.08$	$0.33 \pm 0.03$
$\log(\text{sSFR}/\text{Gyr}^{-1}) = 0.6 \pm 0.5$	$1.38 \pm 0.17$	$1.00 \pm 0.15$	$0.79 \pm 0.05$	$3.05 \pm 0.01$	$0.67 \pm 0.10$	$1.03 \pm 0.09$	$0.18 \pm 0.03$
$E(B - V) = 0.07 \pm 0.04$	$2.03 \pm 0.15$	$1.23 \pm 0.14$	$0.74 \pm 0.05$	$2.95 \pm 0.01$	$0.84 \pm 0.07$	$0.89 \pm 0.09$	$0.19 \pm 0.03$
$E(B - V) = 0.12 \pm 0.05$	$1.18 \pm 0.18$	$1.44 \pm 0.14$	$0.89 \pm 0.06$	$3.63 \pm 0.02$	$1.44 \pm 0.09$	$1.08 \pm 0.08$	$0.28 \pm 0.03$
Full Sample	$1.42 \pm 0.09$	$0.90 \pm 0.09$	$0.76 \pm 0.04$	$3.00 \pm 0.05$	$0.79 \pm 0.06$	$0.67 \pm 0.06$	$0.26 \pm 0.02$

NOTE—

<sup>a</sup> The pair sample is split into tertiles in  $M_*$ ; the remaining subsamples are formed by splitting the pair sample in half at the median value of the stellar population parameter. Each subsample's median value and interquartile range are shown; see Figure 3 for the precise ranges of each subsample. The corresponding spectra from which these values are derived are shown in Figures 12–17. Values from the full pair sample are shown in the last row for comparison.

<sup>b</sup>  $W_\lambda$  (C IV) is computed by integrating over the full doublet.

<sup>c</sup> In order: the minimum, maximum, and median  $D_{\text{tran}}$  (in kpc) for each bin.

<sup>d</sup> The DTB  $W_\lambda$  (C IV) are corrected as discussed in Section 4 (cf.  $W_{\lambda, \text{corr}}$  in Table 1).

**Table 3.** Absorption Velocity Centroids ( $\Delta v$ ) vs. Foreground Galaxy Properties

Composite	Ly $\alpha$			C IV $\lambda$ 1549			
	[8, 70] (51)	[70, 100] (86)	[100, 250] (188)	DTB	[8, 70] (51)	[70, 100] (86)	[100, 250] (188)
	( $\text{km s}^{-1}$ )	( $\text{km s}^{-1}$ )	( $\text{km s}^{-1}$ )	( $\text{km s}^{-1}$ )	( $\text{km s}^{-1}$ )	( $\text{km s}^{-1}$ )	( $\text{km s}^{-1}$ )
$\log(M_*/M_\odot) = 9.0 \pm 0.5$	$-15 \pm 100$	$182 \pm 68$	$111 \pm 43$	$-294 \pm 20$	$133 \pm 123$	$56 \pm 79$	$280 \pm 124$
$\log(M_*/M_\odot) = 9.6 \pm 0.3$	$43 \pm 42$	$31 \pm 51$	$70 \pm 27$	$-294 \pm 6$	$9 \pm 63$	$8 \pm 74$	$96 \pm 85$
$\log(M_*/M_\odot) = 10.2 \pm 0.4$	$-19 \pm 51$	$-44 \pm 28$	$-50 \pm 40$	$-235 \pm 5$	$126 \pm 37$	$-97 \pm 58$	$-38 \pm 48$
$\log[\text{SFR}/(M_\odot \text{ yr}^{-1})] = 0.6 \pm 0.3$	$25 \pm 44$	$155 \pm 49$	$24 \pm 34$	$-255 \pm 9$	$23 \pm 64$	$10 \pm 47$	$91 \pm 41$
$\log[\text{SFR}/(M_\odot \text{ yr}^{-1})] = 1.2 \pm 0.3$	$16 \pm 47$	$-61 \pm 53$	$80 \pm 28$	$-328 \pm 4$	$110 \pm 44$	$63 \pm 52$	$31 \pm 56$
$\log(\text{sSFR}/\text{Gyr}^{-1}) = -0.2 \pm 0.4$	$36 \pm 46$	$87 \pm 46$	$-79 \pm 31$	$-269 \pm 6$	$89 \pm 51$	$-177 \pm 84$	$69 \pm 55$
$\log(\text{sSFR}/\text{Gyr}^{-1}) = 0.6 \pm 0.5$	$-15 \pm 53$	$64 \pm 59$	$106 \pm 27$	$-330 \pm 6$	$174 \pm 84$	$-17 \pm 47$	$198 \pm 106$
$E(B - V) = 0.07 \pm 0.04$	$15 \pm 31$	$172 \pm 49$	$87 \pm 27$	$-283 \pm 5$	$126 \pm 46$	$114 \pm 54$	$201 \pm 93$
$E(B - V) = 0.12 \pm 0.05$	$-63 \pm 70$	$-28 \pm 40$	$-13 \pm 26$	$-306 \pm 6$	$89 \pm 35$	$-123 \pm 69$	$90 \pm 58$
Full Sample	$-4 \pm 39$	$126 \pm 35$	$53 \pm 20$	$-285 \pm 7$	$122 \pm 47$	$-100 \pm 91$	$119 \pm 45$

NOTE—As for Table 2, with centroid velocity relative to systemic rather than  $W_\lambda$ .

three by mass<sup>8</sup>; the results are shown in Figure 17, including DTB spectra of the foreground galaxies for comparison. The blue, green, and red spectra correspond to stacks with  $\log(M_*/M_\odot)$  of approximately 9.0, 9.6, and 10.2 and show the same trend of increasing C IV absorption with stellar mass, this time though with an additional gradation. In the  $D_{\text{tran}} = 8 - 70$  kpc bin, we see a factor of 2.2 increase in

$W_\lambda$  between the first and second bins and a 59% increase between the second and third. The increase in absorption depth with mass implies the total C IV column density at fixed  $D_{\text{tran}}$  (perhaps unsurprisingly) increases with each subsequent bin. Incorporating the DTB spectra we find that in general, higher mass halos have stronger C IV absorption at all radii. If CGM size is related to the virial radius, then a LOS at constant  $D_{\text{tran}}$  would sample less absorbing gas at smaller masses and may explain the comparatively weak C IV absorption in the  $\log(M_*/M_\odot) = 9.0$  bin.

<sup>8</sup> We find splitting the sample into quartiles and beyond results in stacks with an insufficient number of pairs to successfully detect C IV.



**Table 4.** Absorption Second Moments ( $\sigma$ ) vs. Foreground Galaxy Properties

Composite	Ly $\alpha$			C IV $\lambda$ 1549			
	[8, 70] (51)	[70, 100] (86)	[100, 250] (188)	DTB	[8, 70] (51)	[70, 100] (86)	[100, 250] (188)
	(km s $^{-1}$ )	(km s $^{-1}$ )	(km s $^{-1}$ )	(km s $^{-1}$ )	(km s $^{-1}$ )	(km s $^{-1}$ )	(km s $^{-1}$ )
$\log(M_*/M_\odot) = 9.0 \pm 0.5$	243 $\pm$ 73	264 $\pm$ 64	244 $\pm$ 49	539 $\pm$ 35	275 $\pm$ 91	430 $\pm$ 51	525 $\pm$ 72
$\log(M_*/M_\odot) = 9.6 \pm 0.3$	324 $\pm$ 28	307 $\pm$ 36	248 $\pm$ 28	603 $\pm$ 8	384 $\pm$ 54	438 $\pm$ 48	541 $\pm$ 40
$\log(M_*/M_\odot) = 10.2 \pm 0.4$	310 $\pm$ 32	380 $\pm$ 14	263 $\pm$ 35	646 $\pm$ 5	444 $\pm$ 22	377 $\pm$ 52	358 $\pm$ 47
$\log[\text{SFR}/(M_\odot \text{ yr}^{-1})] = 0.6 \pm 0.3$	302 $\pm$ 32	294 $\pm$ 48	266 $\pm$ 29	523 $\pm$ 16	296 $\pm$ 71	452 $\pm$ 28	556 $\pm$ 18
$\log[\text{SFR}/(M_\odot \text{ yr}^{-1})] = 1.2 \pm 0.3$	288 $\pm$ 40	308 $\pm$ 42	208 $\pm$ 36	615 $\pm$ 5	438 $\pm$ 26	398 $\pm$ 36	337 $\pm$ 52
$\log(\text{sSFR}/\text{Gyr}^{-1}) = -0.2 \pm 0.4$	325 $\pm$ 29	329 $\pm$ 34	270 $\pm$ 27	578 $\pm$ 8	361 $\pm$ 44	370 $\pm$ 83	494 $\pm$ 27
$\log(\text{sSFR}/\text{Gyr}^{-1}) = 0.6 \pm 0.5$	264 $\pm$ 48	282 $\pm$ 54	213 $\pm$ 34	609 $\pm$ 8	308 $\pm$ 79	395 $\pm$ 34	364 $\pm$ 83
$E(B - V) = 0.07 \pm 0.04$	342 $\pm$ 17	261 $\pm$ 51	228 $\pm$ 33	565 $\pm$ 7	294 $\pm$ 54	501 $\pm$ 27	426 $\pm$ 71
$E(B - V) = 0.12 \pm 0.05$	229 $\pm$ 53	348 $\pm$ 24	265 $\pm$ 20	621 $\pm$ 6	478 $\pm$ 18	359 $\pm$ 75	448 $\pm$ 35
Full Sample	290 $\pm$ 47	257 $\pm$ 21	245 $\pm$ 18	576 $\pm$ 17	348 $\pm$ 46	388 $\pm$ 87	459 $\pm$ 26

NOTE—Similar to Tables 2 and 3, now with second moment measurements. The DTB  $\sigma(\text{C IV})$  are measured over the full doublet and corrected as discussed in Section 4.

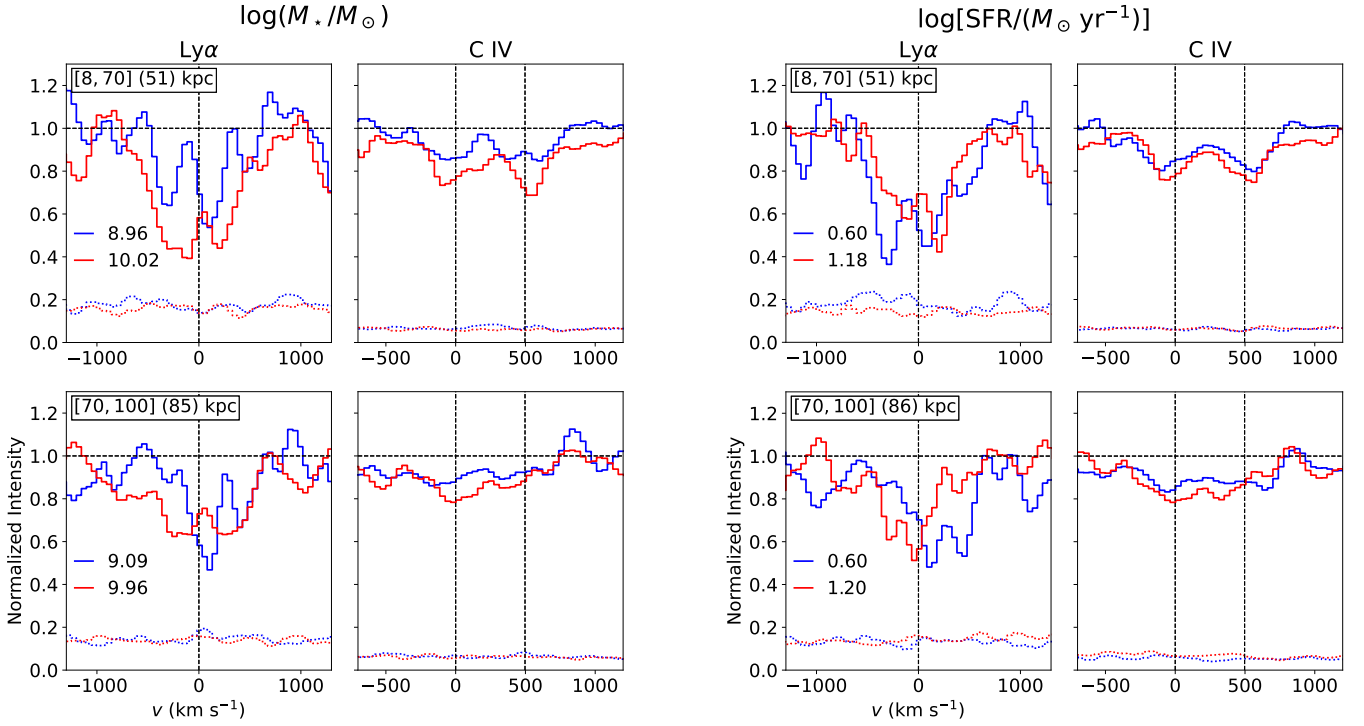


**Figure 12.** Ly $\alpha$  (left column) and C IV (right column) absorption spectra split into subsamples based on stellar mass ( $M_*$ ). Two ranges of  $D_{\text{tran}}$  are shown: 8 – 70 kpc (top) and 70 – 100 kpc (bottom), each with a similar number of constituent pairs ( $\simeq 100$  per subsample). Error spectra are shown as color coded dotted lines; the continuum level and systemic velocity of the foreground galaxy are indicated with black dashed lines. Subsamples are constructed by splitting the  $M_*$  distribution in half and forming samples from each in the  $D_{\text{tran}}$  range specified. In the plot, the “low” subsample is shown in blue while the “high” subsample is in red. The median  $\log(M_*/M_\odot)$  in each subsample is shown in the legend. Figure 3 shows the full distributions.

**Figure 13.** Plot elements and projected distances are the same as Figure 12 except this time the background spectra are split based on SFR. The legend has the median  $\log[\text{SFR}/(M_\odot \text{ yr}^{-1})]$  for each bin.

The  $D_{\text{tran}} = 8 - 70$  kpc bin shows a trend of increasing velocity dispersion across the doublet with increased mass. We observe a 40% increase between the first two mass bins and a 16% increase between the second and third, mostly due to an increase in  $\sigma$  for C IV  $\lambda$ 1548. While the inner  $D_{\text{tran}}$  bin shows increasing  $\sigma(\text{C IV})$  with  $M_*$ , the  $D_{\text{tran}} = 70 - 100$

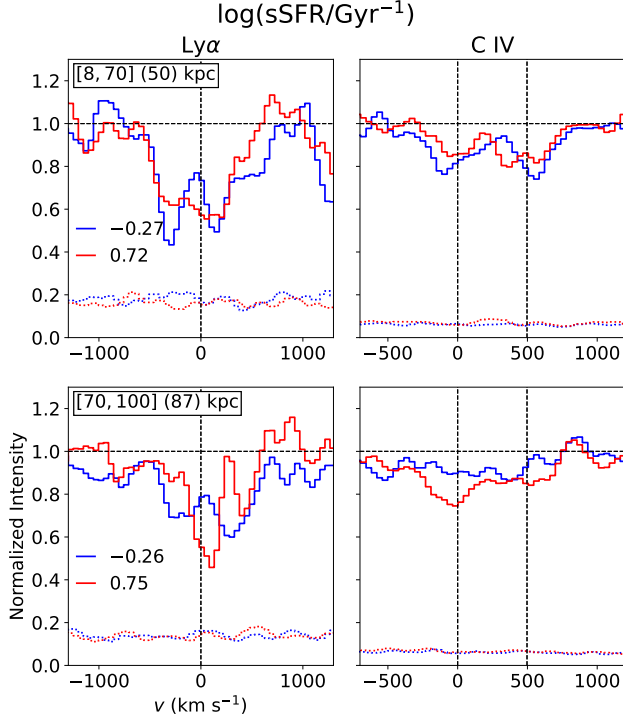


**Figure 14.** Plot elements and  $D_{\text{tran}}$  are the same as Figures 12 and 13; this time splitting by sSFR. The legend has the median  $\log(\text{sSFR}/\text{Gyr}^{-1})$  for both bins.

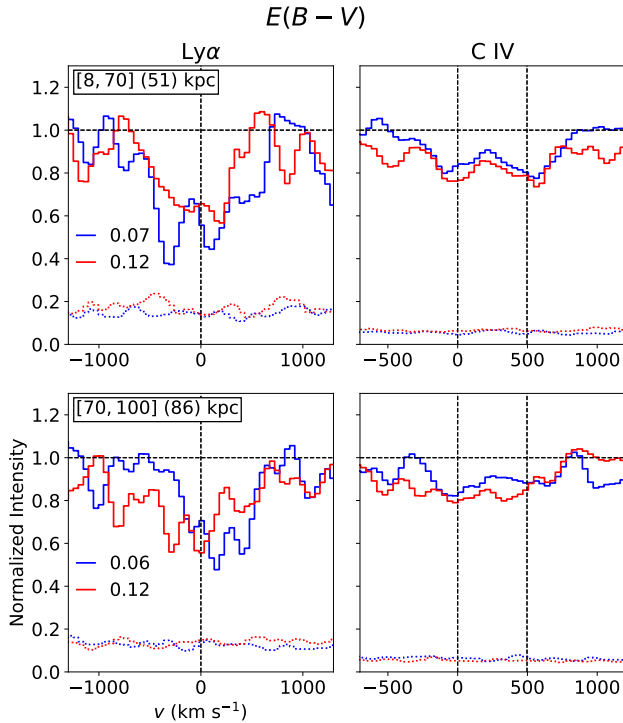


**Figure 15.** Similar to Figures 12, 13, and 14; spectra are binned by  $E(B - V)$ . The legend has the median  $E(B - V)$  for both bins.

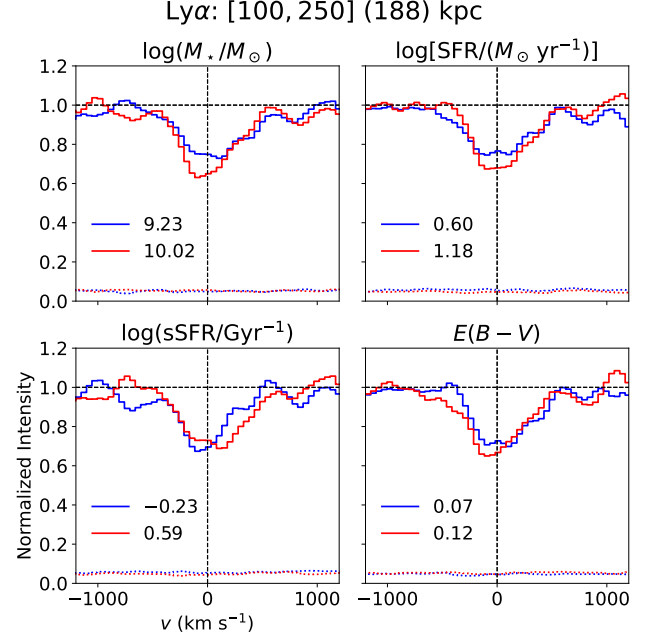


**Figure 16.**  $\text{Ly}\alpha$  absorption is measured for galaxy property subsamples at  $100 < D_{\text{tran}}/\text{kpc} < 250$ . The color and plotting scheme are the same as Figures 12–15.

kpc and 100 – 250 kpc bins show constant and marginally decreasing velocity dispersions, respectively. The low and high SFR subsamples also show a 48% increase in  $\sigma(\text{C IV})$  and a 60% increase in  $W_\lambda(\text{C IV})$  at  $D_{\text{tran}} \simeq 51$  kpc. These observations are in line with DTB C IV  $\lambda 1548$  measurements that show increased absorption strength in  $v < -500$   $\text{km s}^{-1}$  gas and faster outflows (inferred by e.g. a larger  $\sigma(\text{C IV})$ ) in higher mass galaxies (see the left panel of Figure 17).

While  $\text{Ly}\alpha$  absorption strength and velocity dispersion increase with  $M_*$  in all three  $D_{\text{tran}}$  bins, the trend is non-monotonic and both quantities exhibit more scatter than C IV. Within  $D_{\text{tran}} < 100$  kpc,  $W_\lambda(\text{Ly}\alpha)$  increases by a factor of  $\simeq 2$  between the low and high mass bins and  $\sigma(\text{Ly}\alpha)$  increases by  $\simeq 40\%$ .  $\text{Ly}\alpha$  absorption strength increases more modestly ( $\simeq 30\%$ ) in the largest  $D_{\text{tran}}$  bin and the velocity dispersions are consistent with mass, but since the median  $D_{\text{tran}}$  of the 100 – 250 kpc bin ( $D_{\text{tran}} \simeq 188$  kpc) is likely well beyond the typical virial radius for galaxies in the sample, one might expect the host galaxy properties to have the smallest effect in this bin. The  $\text{Ly}\alpha$  profiles in the SFR, sSFR, and  $E(B - V)$  bins are largely consistent with one another (Figures 12–16). The profiles become smoother as larger  $D_{\text{tran}}$  are considered since more sightlines are being averaged, but there is no distinguishable trend across all three bins and the variation, especially at small  $D_{\text{tran}}$ , is within the bootstrap-computed uncertainties.

Although the subsamples divided by galaxy properties do not show a large variation in  $\text{Ly}\alpha$  absorption, we note that

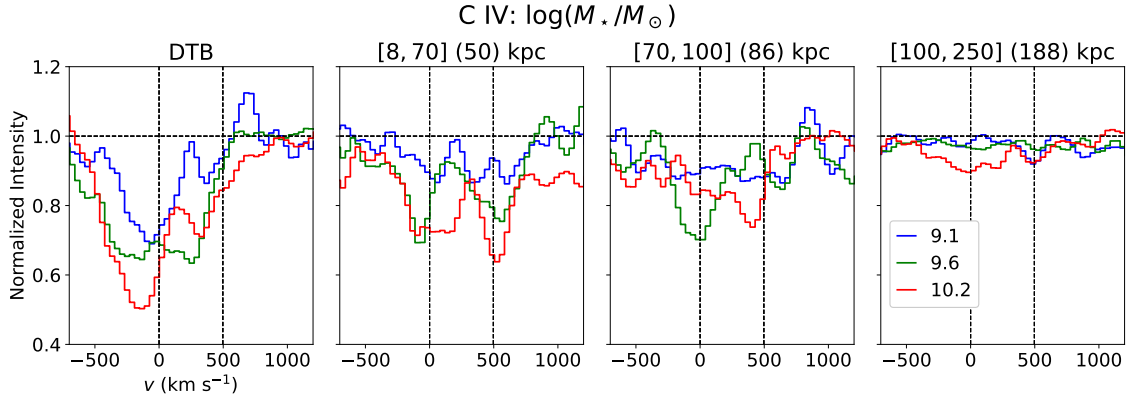


**Figure 17.** Extending the results of Figure 12, C IV absorption is plotted for three mass bins. From left to right, DTB ( $D_{\text{tran}} = 0$  kpc) spectra, the  $D_{\text{tran}} = 8 - 70$  kpc bin,  $D_{\text{tran}} = 70 - 100$  kpc bin, and  $D_{\text{tran}} = 100 - 250$  kpc bin are shown. Blue, green, and red spectra correspond to the first, second, and third tertiles in stellar mass. The legend shows the median  $\log(M_*/M_\odot)$  for each bin.

both low- $M_*$  bins at  $D_{\text{tran}} \leq 100$  kpc shows apparent emission at  $v \simeq 1000$  km s $^{-1}$ . Emission at this velocity and projected distance also appears in the low SFR and low  $E(B - V)$  bins. We hypothesize that this emission could result from foreground galaxy Ly $\alpha$  emission (whose emission profiles frequently extend to velocities  $|v| \simeq 1000$  km s $^{-1}$ ) contributing to the absorption line profile. In such a situation, the emission strength could exceed the absorption strength at  $v \simeq 1000$  km s $^{-1}$  and lead to net emission where elsewhere in the profile there is only absorption. We explore this point further in Appendix D.

Of all the stellar population parameters, sSFR shows the smallest difference between bins. The differences between  $E(B - V)$  bins similarly do not appear to have a coherent trend. A larger number of galaxy pairs would be required to determine exactly how much of the variability seen at  $D_{\text{tran}} < 100$  kpc is due to sample variance and where the velocity profiles begin to converge when separated by galaxy properties.

## 5. 2-D ABSORPTION MAPS

In addition to one dimensional spectra, we constructed two dimensional maps of apparent optical depth (defined as in Chen et al. 2020)

$$\tau_{\text{app}} = -\ln \frac{F(v)}{F_{\text{cont}}(v)}, \quad (3)$$

as a function of both  $v_{\text{LOS}}$  and  $D_{\text{tran}}$ ; these are shown in Figure 18. In Equation 3,  $F(v)$  is the flux density measured for a stacked spectrum and  $F_{\text{cont}}(v)$  is the level of the continuum. When working with normalized spectra,  $F_{\text{cont}}(v)$  would naturally be one.

We know from QSO sightlines through the CGM for a fraction of the galaxies in this sample that H I and metals at these projected distances are clumpy and comprise several discrete velocity components (Rudie et al. 2012). Although absorption is seen at velocities  $|\Delta v| < 700$  km s $^{-1}$ , the individual

velocity components do not span the full range of velocities meaning large swaths of velocity space may show little to no absorption. Where present however, most complexes have  $N_{\text{HI}} \gtrsim 10^{14.5}$  cm $^{-2}$  such that Ly $\alpha$  is saturated. At low resolution, as in Figure 18, the apparent optical depth  $\tau$  shows the variation in velocity and covering fraction of the clumps along the line of sight.

On that point, the two-dimensional maps in Figure 18 illustrate the spatial and velocity extent of Ly $\alpha$  (top) and C IV (bottom). Each map's respective  $S/N$  is presented in the right half of the figure. Given that these are compilations of one-dimensional stacks (selected examples of which are shown in Figure 5), they trivially support the assertions made in Section 4.1, i.e. both Ly $\alpha$  and C IV start out with extended absorption at small  $D_{\text{tran}}$  which shallows (both in  $\tau$  and  $v_{\text{LOS}}$ ) as galactocentric radius increases. The two-dimensional representation highlights the location of the velocity centroid and how that evolves with  $D_{\text{tran}}$ . Interestingly, Ly $\alpha$  absorption is the strongest within  $D_{\text{tran}} \lesssim 50$  kpc at  $v_{\text{LOS}} \simeq -250$  km s $^{-1}$ , indicative of a blue-dominated velocity asymmetry. Moving to larger  $D_{\text{tran}}$ , the velocity centroid shifts to  $v_{\text{LOS}} \simeq 100$  km s $^{-1}$  by  $D_{\text{tran}} \simeq 80$  kpc and Ly $\alpha$  absorption appears skewed by  $\Delta v \simeq 100$  km s $^{-1}$  to red LOS velocities for  $D_{\text{tran}} \lesssim 200$  kpc.

The 2D C IV spectra in Figure 18 has  $\Delta v$  closer to each transition's respective systemic velocity but exhibits high velocity components at small  $D_{\text{tran}}$ . As seen in Figure 5, at  $D_{\text{tran}} \simeq 20$  kpc, LOS velocities reach  $v_{\text{LOS}} \simeq 500$  km s $^{-1}$  and fall off with increasing  $D_{\text{tran}}$ . By the time the C IV transition is becoming optically thin at  $D_{\text{tran}} \simeq 60$  kpc, the C IV velocity spread is  $\simeq 350$  km s $^{-1}$ . Weak excess C IV  $\lambda 1548$  absorption appears to extend to  $D_{\text{tran}} \simeq 150$  kpc and beyond, but the LOS velocities measured at large projected distances are less than the effective spectral resolution element and may be spurious.

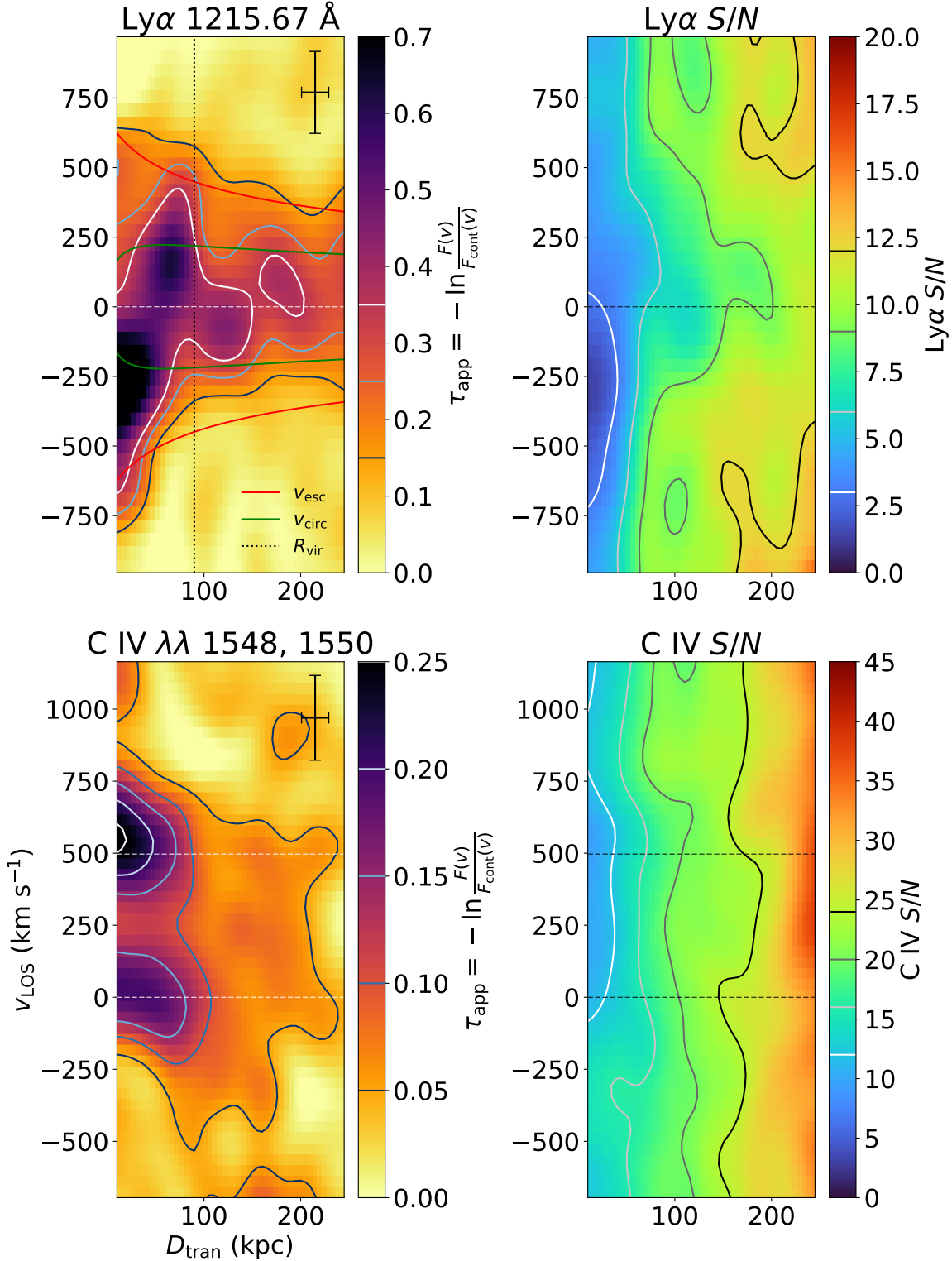


**Figure 18.** *Top:* Relative optical depth ( $\tau_{\text{app}}$ ; Equation 3) maps as a function of  $v_{\text{LOS}}$  and  $D_{\text{tran}}$  computed for Ly $\alpha$  (top left) and C IV (bottom left). The darker regions correspond to deeper absorption troughs and thus higher apparent optical depths. The escape velocity, circular velocity, and virial radius for a  $M_{\text{halo}} = 10^{12} M_{\odot}$  NFW halo are denoted in red, green, and black, respectively. The C IV map on the bottom has C IV  $\lambda 1548$  at  $v_{\text{LOS}} = 0 \text{ km s}^{-1}$  and C IV  $\lambda 1550$  at  $v_{\text{LOS}} = 497 \text{ km s}^{-1}$  analogous to Figure 5. The Ly $\alpha$  (top right) and C IV (bottom right) S/N maps are shown in the second column. Contours are plotted where applicable on each respective colorbar. Ly $\alpha$  (C IV) contours are separated by  $\Delta\tau = 0.1$  (0.05) and S/N contours proceed in increments of three (four) i.e.,  $\Delta(S/N) = 3$  (4). The black error bar in the top right of the left-hand panels shows the average bin size and effective LOS velocity resolution.

### 5.1. A semianalytic model

To better understand the main features of Figure 18, we tailored the simple analytic model presented by Chen et al. (2020) to our higher resolution absorption maps. We provide an overview of the model in this work and direct the reader to that study for a complete description of each parameter. The primary difference between the two models is that our sample is restricted to  $D_{\text{tran}} \leq 250$  kpc, while the Chen et al. (2020) sample extends to  $D_{\text{tran}} \simeq 4$  Mpc.

#### 5.1.1. Model Parameters

Following Chen et al. (2020), we constructed a two-component model that attempts to capture the overall trends in Figure 18: a general decrease in LOS velocity spread and  $\tau$  with  $D_{\text{tran}}$ . We employ two velocity components: an outflow component whose velocity depends on galactocentric radius, together with a random velocity component constrained by the gravitational potential well of the average foreground galaxy; for simplicity, both operate independent of one another. The outflow velocity profile assumes an NFW halo (Navarro et al. 1996, 1997) where gas is initially accelerated to a maximum velocity  $v_1$  within a galactocentric radius  $r \simeq 1$  kpc and subsequently decelerates with increasing  $D_{\text{tran}}$  solely under the influence of gravity. The outflowing radial velocity field is defined such that

$$v_{\text{out}}(r) = \sqrt{v_1^2 + A \left( -\ln \frac{R_s + 1}{R_s} + \frac{1}{r} \ln \frac{R_s + r}{R_s} \right)}, \quad (4)$$

where the NFW scale radius  $R_s = 27$  kpc ( $R_{\text{vir}} \simeq 90$  kpc, given a concentration parameter  $c = 3.3$ ) and

$$A = \frac{8\pi G \rho_0 R_s^3}{1 \text{ kpc}} \simeq 1.2 \times 10^7 \text{ km}^2 \text{ s}^{-2} \quad (5)$$

for a NFW halo at  $z \simeq 2.3$  with mass  $M_{\text{halo}} = 10^{12} M_{\odot}$ .

To add additional opacity near  $v_{\text{LOS}} = 0$  km s<sup>-1</sup>, the random velocity component takes on a Gaussian velocity distribution with constant width ( $\sigma_v$ ) with radius. In contrast to Chen et al. (2020), we also neglect the Hubble expansion due to the close-in range of  $D_{\text{tran}}$  sampled. This represents the simplest parameterization of the non-outflowing gas motions we observe.

Since the velocities we measure relative to the foreground galaxy systemic redshift are projected along our LOS, we set up two grids: one in terms of projected distance ( $D_{\text{tran}}$ ) and the other over a range of line of sight distances ( $\ell$ ) such that each combination of  $D_{\text{tran}}$  and  $\ell$  form a right triangle satisfying  $r^2 = \ell^2 + D_{\text{tran}}^2$ . The line of sight velocity for a given component is therefore

$$v_{\text{LOS}}(D_{\text{tran}}, \ell) = \frac{\ell}{r} v(r) = \frac{\ell}{\sqrt{D_{\text{tran}}^2 + \ell^2}} v(r). \quad (6)$$

Similar to the two velocity components, we let the apparent optical depth from each component vary as independent radial power laws

$$\tau_{\text{out}}(r) = \tau_{0, \text{out}} \left( \frac{r}{100 \text{ kpc}} \right)^{-\beta_{\text{out}}} \quad (7)$$

and

$$\tau_r(r) = \tau_{0, r} \left( \frac{r}{100 \text{ kpc}} \right)^{-\beta_r}, \quad (8)$$

in which  $\tau_{0, i}$  are the apparent optical depth maxima used to normalize the distribution,  $\beta_i$  are the respective power law indices for each component, and  $r$  is once again the galactocentric radius. For each  $(D_{\text{tran}}, \ell)$  grid point, we measured velocities and apparent optical depths and projected each into the  $v_{\text{LOS}} - D_{\text{tran}}$  plane using Equation 6. Like Figure 18,  $\tau_{\text{app}}$  is best interpreted as an excess optical depth (at a particular velocity and  $D_{\text{tran}}$ ) since we do not measure the total optical depth or absorption along the line of sight. The power laws in the model were therefore truncated at  $r = 500$  kpc (twice the maximum  $D_{\text{tran}}$  of the pair sample) or where  $\tau_{\text{app}}$  was below the noise level of the observed maps to ensure  $\tau_{\text{app}}$  represented absorption associated with the galaxy and not the IGM.

#### 5.1.2. Results

The observed Ly $\alpha$  map has  $\Delta v_{\text{LOS}} = 50$  km s<sup>-1</sup> and  $\Delta D_{\text{tran}} = 5$  kpc sampling. Given the simplicity of the model and its inability to capture small variations in apparent optical depth, we smoothed the observed Ly $\alpha$  map with a 2 pix  $\times$  2 pix Gaussian kernel ( $\sigma_{D_{\text{tran}}} = 10$  kpc and  $\sigma_{v_{\text{LOS}}} = 100$  km s<sup>-1</sup>) so the broad trends are captured and the fitting procedure is facilitated. Since the model is symmetric around  $v_{\text{LOS}} = 0$  km s<sup>-1</sup>, we folded the data around that point to compensate for the asymmetry in the measured Ly $\alpha$  absorption (especially at  $D_{\text{tran}} \lesssim 50$  kpc). We argue in Appendix D that this asymmetry results from foreground Ly $\alpha$  emission contributing to the background absorption feature, so the folded map bears a closer resemblance to the unaffected signal. We employ the emcee (Foreman-Mackey et al. 2013) Markov chain Monte Carlo (MCMC) sampler to find the best fit to the six ( $v_1$ ,  $\sigma_v$ ,  $\tau_{0, \text{out}}$ ,  $\tau_{0, r}$ ,  $\beta_{\text{out}}$ , and  $\beta_r$ ) model parameters given the smoothed Ly $\alpha$  optical depth and uncertainty maps. We require the fit  $\sigma_v$  to have a velocity consistent with the random velocity dispersion of a  $10^{12} M_{\odot}$  halo. The best fit model is shown in the middle panel of Figure 19 and the parameters used to generate it are enumerated in Table 5.

In comparing the best fit models between Chen et al. (2020) and our study we recall that the range of  $D_{\text{tran}}$  sampled in Chen et al. (2020) span galactocentric radii larger by an order of magnitude than our current sample. With this

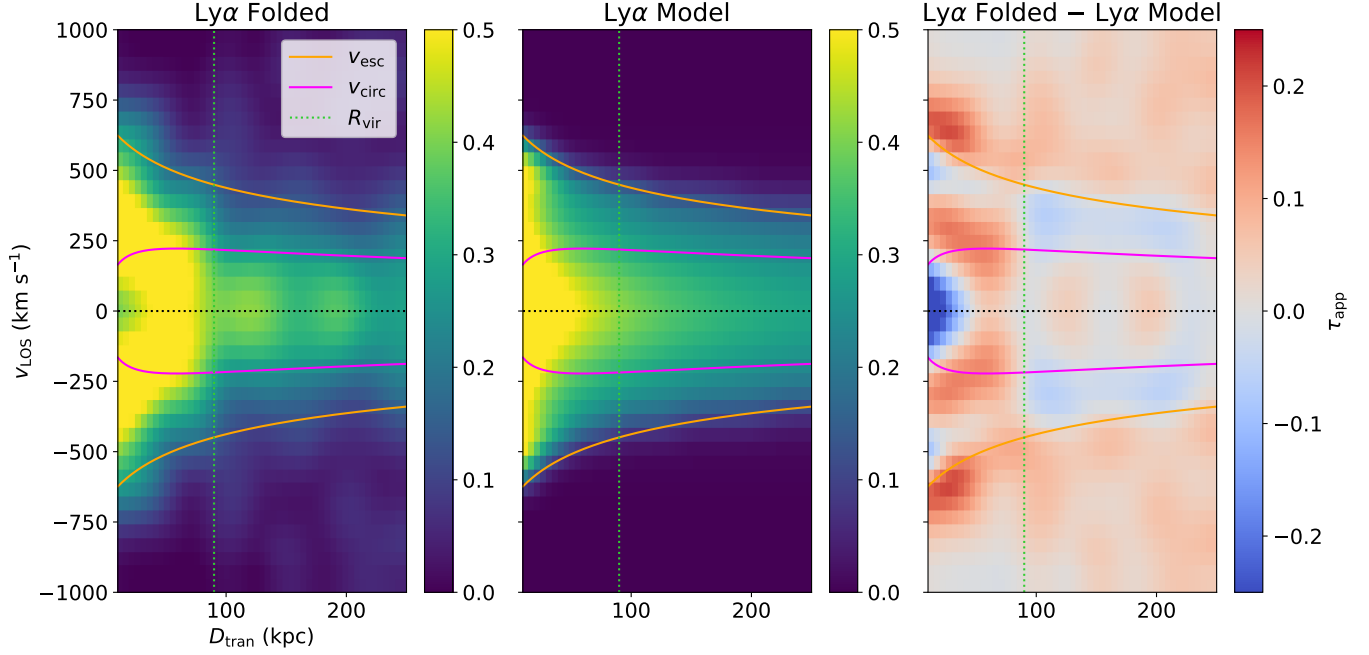


**Figure 19.** *Left:* Measured Ly $\alpha$  apparent optical depth folded about  $v_{\text{LOS}} = 0 \text{ km s}^{-1}$ ; *Middle:* Ly $\alpha$  best fit model utilizing both outflow and inflow components; *Right:* Ly $\alpha$  absorption residuals (data – model). The observed and model heatmaps have the same colorbar. The escape and circular velocities for a  $M_{\text{halo}} = 10^{12} M_{\odot}$  NFW halo are shown in orange and magenta respectively in conjunction with the approximate virial radius (lime green).

**Table 5.** Best Fit Model Parameters

Component	Parameter	Two Component <sup>a</sup>	Outflow Only
Outflow	$v_1$ (km s <sup>-1</sup> )	$781^{+73}_{-77}$	$750^{+44}_{-2}$
	$\tau_{0, \text{out}}$	$0.21^{+0.08}_{-0.09}$	$0.32^{+0.01}_{-0.01}$
	$\beta_{\text{out}}$	$0.40^{+0.21}_{-0.17}$	$0.35^{+0.04}_{-0.04}$
Random Velocity	$\sigma_v$ (km s <sup>-1</sup> )	$219^{+32}_{-34}$	...
	$\tau_{0, r}$	$0.20^{+0.11}_{-0.11}$	...
	$\beta_r$	$0.32^{+0.36}_{-0.22}$	...

NOTE—

<sup>a</sup> The two component model features both outflowing and random velocity gas.

in mind, we note a few distinctions. The initial outflow velocity ( $v_1$ ) is larger by 30% in the current sample ( $781^{+73}_{-77} \text{ km s}^{-1}$  vs.  $603^{+5}_{-11} \text{ km s}^{-1}$ ) and the velocity of gas near the systemic velocity ( $\sigma_v$ ) is a factor of  $\simeq 2.6$  greater in magnitude ( $219^{+32}_{-34} \text{ km s}^{-1}$  vs.  $-84^{+6}_{-6} \text{ km s}^{-1}$ ). The finer sampling and higher velocity resolution of the current sample means low- $\tau_{\text{app}}$ , high- $v_{\text{LOS}}$  is more readily detectable than in the Chen et al. (2020) sample. Intuitively, the outflowing component in the model establishes a high velocity (relatively low optical depth) envelope while the non-outflowing velocity component adds additional opacity at lower velocities centered around  $v = 0 \text{ km s}^{-1}$ . Since the gas with the highest galactocentric velocity in both Chen et al. (2020) and

this sample is found at  $D_{\text{tran}} \lesssim 60 \text{ kpc}$ , those are the impact parameters that fix the model parameters of the outflowing component. In contrast, an H I overdensity with  $|v| < 200 \text{ km s}^{-1}$  was observed throughout the full 4 Mpc range in Chen et al. (2020), gradually decreasing in optical depth with  $D_{\text{tran}}$ . When restricted to  $D_{\text{tran}} < 250 \text{ kpc}$ , the velocity field appears considerably more active than at larger galactocentric radii so the constant velocity component (centered at  $v_{\text{LOS}} = 0 \text{ km s}^{-1}$ ) will naturally take on a correspondingly higher value to match that velocity spread. It is for this reason that although functionally similar to the “inflow” component of the Chen et al. (2020) model, we associate this component with gas with random velocities or high optical depth non-radial flows since it is unlikely that the excess optical depth at these galactocentric distances and velocities results strictly from “inflowing” material.

We observe that the outflow and constant velocity gas absorption coefficients ( $\tau_{0, \text{out}}$ ,  $\tau_{0, r}$ ) in the current sample are larger than the Chen et al. (2020) measurements by a factor of  $\sim 6$  and  $\sim 25$ , respectively (cf.  $\alpha_{0, \text{in}}$  and  $\alpha_{0, \text{out}}$  in Chen et al. 2020). The difference in integration box sizes between the two samples may affect this quantity most significantly. Moreover, the increased spectral resolution in the current study results in more pronounced absorption troughs and therefore higher excess optical depth measurements especially near the systemic velocity. This explains why the

random velocity component (centered around  $v_{\text{sys}} = 0 \text{ km s}^{-1}$ ) has the largest contrast between samples.

Perhaps of more significance is that the opacity of the random velocity gas is similar to that of the outflow i.e.  $\tau_{0,r} \sim \tau_{0,\text{out}}$  contrary to what was seen previously in [Chen et al. \(2020\)](#). One can consider this element of the model as absorption due to gas with velocities  $v_{\text{LOS}} \lesssim 300 \text{ km s}^{-1}$ , similar to but not the same as an ISM component to a down-the-barrel absorption line profile in a galaxy with outflowing material. For our sample, the ratio  $\tau_{0,r}/\tau_{0,\text{out}} \simeq 1$  suggests (perhaps unsurprisingly) most of the gas in the inner CGM ( $D_{\text{tran}} < 250 \text{ kpc}$ ) is relatively slow moving ( $v_{\text{LOS}} \lesssim 300 \text{ km s}^{-1}$ ) but there exists an appreciable component of outflowing material.

More quantitatively, in [Figure 19](#), we plot the circular and escape velocity for a  $M_{\text{halo}} = 10^{12} M_{\odot}$  NFW halo. These curves treat  $r = D_{\text{tran}}$  and do not account for velocity projection effects so the real radii may be larger and LOS velocities may be smaller. As expected, the circular velocity approximately matches the random velocity component since both are constrained by the gravitational potential well of the average host galaxy. We observe the escape velocity at the virial radius  $v_{\text{esc}}(R_{\text{vir}}) \approx 400 \text{ km s}^{-1}$  is close to the maximum velocity associated with the outflowing component. While most of the absorbing gas has velocities less than the escape velocity, a nontrivial fraction has the possibility of escaping the halo. As discussed in [Section 4.2](#),  $\text{Ly}\alpha$  absorption is not the best probe of high velocity gas since higher ionization lines sample a larger cross-section of the CGM, but the fact that a nominal amount of H I exceeds  $v_{\text{esc}}$  supports this hypothesis.

As a possible simplification, we attempt to fit the  $\text{Ly}\alpha$  optical depth map with an outflow-only model; the results are shown in [Figure 20](#) and listed in the right-most column in [Table 5](#). Looking at the residual map (right panel in [Figure 20](#)), it is apparent that fitting solely the outflow provides a marginal reproduction of the observed trends. In particular, while the high velocity gas envelope is present, the model  $\tau_{\text{app}}$  is inaccurate throughout most of the map. The lack of absorbing gas in the model at  $|v_{\text{LOS}}| \lesssim 250 \text{ km s}^{-1}$ , especially at  $D_{\text{tran}} \gtrsim 50 \text{ kpc}$  is a clear indicator that another component is required for the model to better resemble the observed  $\text{Ly}\alpha$  absorption.

As discussed in [Chen et al. \(2020\)](#), the strictly radial dependence of velocity and excess optical depth is clearly an oversimplification of a complex environment. With the improved resolution in both  $v_{\text{LOS}}$  and  $D_{\text{tran}}$ , this simplification becomes even more suspect. We measure a clumpy distribution of  $\text{Ly}\alpha$  absorption due to variance in the constituent galaxy stacks; two examples of regions with higher than average opacity can be seen in the left panel of [Figure 19](#) at  $D_{\text{tran}} \simeq 125 \text{ kpc}$  and  $D_{\text{tran}} \simeq 175 \text{ kpc}$ . To model these

semianalytically, either non-radial optical depth and velocity profiles would need to be implemented or a third component would need to be added for this express purpose, but since these features are most likely systematic noise, further complications to the model may be unjustified.

In the observed  $\text{Ly}\alpha$  map there is a step in the velocity field at approximately the virial radius for the average foreground galaxy halo ( $R_{\text{vir}} \simeq 80 \text{ kpc}$ ) where the velocity spread decreases from  $\sim 750 \text{ km s}^{-1}$  to  $\sim 500 \text{ km s}^{-1}$ ; we denote the approximate virial radius as a green dotted line in the left panel of [Figure 19](#). Despite its simplicity, the inflow component of the model shows a marked downturn in absorption strength at approximately the same projected distance. We conjecture that this could be a site where outflowing and inflowing gas are both present and would therefore result in a smaller average velocity when measured spectroscopically. The data are unable to show the degree (or lack thereof) to which the two components interact or mix but considering that the model treats the outflowing and random velocity components as separate sources of excess absorption, even noninteracting gas streams may produce this ‘‘pinch’’ in the velocity field. In a situation where the two components interact, the effect on the line of sight velocities could be more pronounced.

## 6. DISCUSSION

The enhanced excess  $\text{Ly}\alpha$  absorption extending out to the maximum  $D_{\text{tran}}$  of the sample ( $D_{\text{tran}} \simeq 250 \text{ kpc}$ ) is consistent with [Rudie et al. \(2012\)](#) and [Turner et al. \(2014\)](#) using KBSS QSO lines of sight and [Steidel et al. \(2010\)](#) and [Chen et al. \(2020\)](#) with KBSS galaxy pairs. The  $\text{Ly}\alpha$  equivalent width scaling ( $W_{\lambda}(\text{Ly}\alpha) \propto D_{\text{tran}}^{-0.50}$ ) in particular closely matches the dependence seen in both [Steidel et al. \(2010\)](#) and [Chen et al. \(2020\)](#). The [Chen et al. \(2020\)](#)  $W_{\lambda}(\text{Ly}\alpha)$  measurements are shown in [Figure 6](#) (brown curve) for comparison and both  $W_{\lambda}(\text{Ly}\alpha)$  agree well with one another. Note that in [Steidel et al. \(2010\)](#),  $W_{\lambda}(\text{Ly}\alpha)$  at  $100 \lesssim \langle D_{\text{tran}} \rangle / \text{kpc} \lesssim 250$  were computed from HIRES spectra of QSO-galaxy pairs while [Chen et al. \(2020\)](#) used galaxy-galaxy pairs for the full range of  $D_{\text{tran}}$  (4 Mpc).

In addition, we find a reduced  $W_{\lambda}(\text{Ly}\alpha)$  and  $\sigma(\text{Ly}\alpha)$  between  $75 \lesssim D_{\text{tran}} / \text{kpc} \lesssim 125$  in accordance with the [Chen et al. \(2020\)](#) results. Given the large overlap in galaxy pairs between [Steidel et al. \(2010\)](#), [Chen et al. \(2020\)](#), and this sample, it is not surprising that the equivalent widths show large agreement. The  $75 \lesssim D_{\text{tran}} / \text{kpc} \lesssim 125$  region is also close to the virial radius of the typical galaxy in our sample and is associated with a ‘‘pinch’’ in the velocity field, evident in [Figures 18](#) and [19](#). If the galaxies in our sample are accreting gas and that gas is cospatial with outflowing material, the superposition of outflowing and inflowing components could reduce the net LOS velocity measured in that

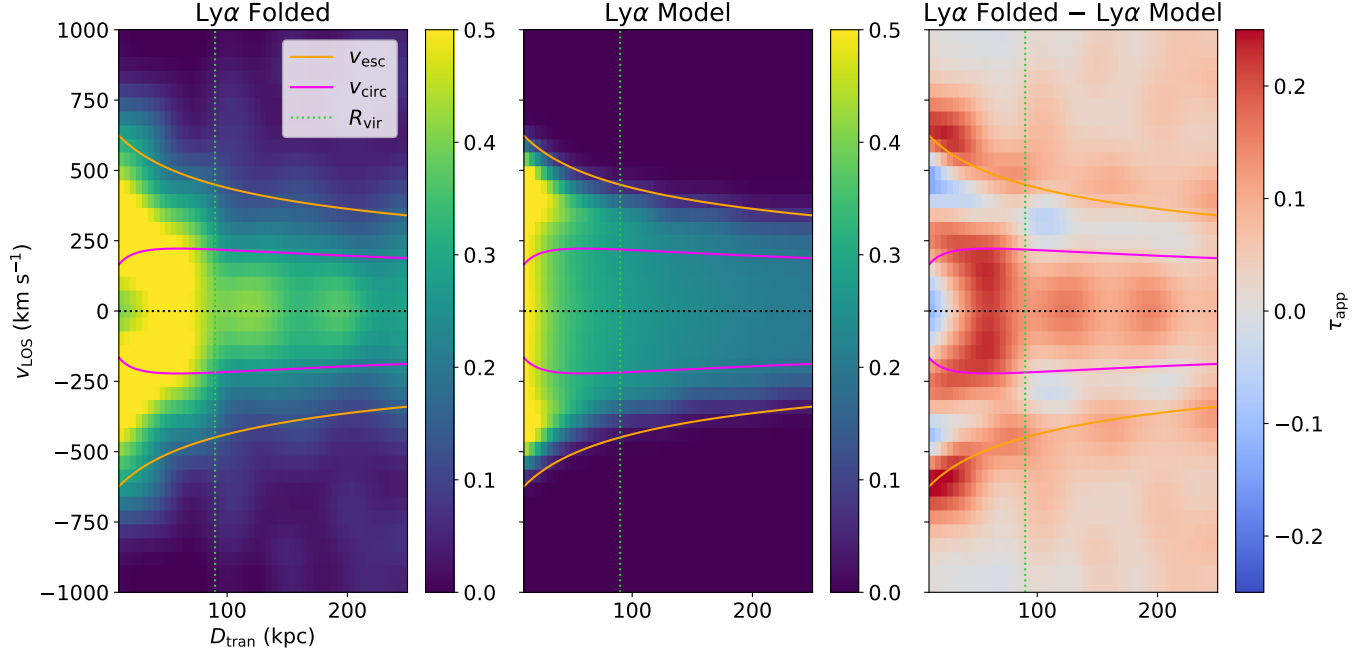


**Figure 20.** Same as Figure 19 except with an outflow-only model.

region. Such a situation may contribute to the local minimum in  $\sigma(\text{Ly}\alpha)$  at  $D_{\text{tran}} \simeq 80$  kpc.

Outside of the KBSS sample, the anticorrelation between  $W_\lambda$  and  $D_{\text{tran}}$  for  $\text{Ly}\alpha$  and metals has been observed in galaxies across a range of masses and redshifts. Kacprzak et al. (2020) recently compiled  $W_\lambda$  vs.  $D_{\text{tran}}$  measurements for  $\text{Ly}\alpha$  and several far-UV transitions from studies (Prochaska et al. 2011; Werk et al. 2013; Bordoloi et al. 2014; Liang & Chen 2014; Borthakur et al. 2015; Burchett et al. 2016; Johnson et al. 2017; Pointon et al. 2019) of  $9 \leq \log(M_*/M_\odot) \leq 11$  galaxies at  $z \lesssim 0.3$ . Each transition shows a decrease in absorption strength with  $D_{\text{tran}}$  with the metals showing the most rapid falloff. Analogous to Si II in our sample, at  $z \lesssim 1.4$ , there is a similar trend between  $W_\lambda(\text{Mg II})$  and  $\sigma(\text{Mg II})$  with  $D_{\text{tran}}$  (Martin et al. 2019; Hamanowicz et al. 2020; Chen & Zahedy 2024) in line with the previously listed studies at  $z \lesssim 0.3$ . It is worth noting that the previously listed studies all use QSOs as their background source which lead to more stochastic gas distributions in comparison to foreground/background galaxy pairs which probe gas on  $\sim 4$  kpc scales (Steidel et al. 2010; the typical half-light diameter of a galaxy in our sample).

At  $z \sim 2$ , Steidel et al. (2010) modeled gas covering fraction  $f_c$  from both H I and metals as power laws of the form  $f_c \propto r^{-\beta}$  and found  $\beta = 0.37$  for  $\text{Ly}\alpha$  at  $D_{\text{tran}} \lesssim 250$  kpc; both of our best-fit  $\text{Ly}\alpha$  model parameters ( $\beta_{\text{out}} = 0.40$ ;  $\beta_r = 0.32$ ) are comparable. In fitting the  $W_\lambda$  vs.  $D_{\text{tran}}$  distribution, we find similarly shallow power law indices:  $\langle \gamma \rangle \simeq 0.38$  for the high ions and  $\langle \gamma \rangle \simeq 0.46$  for the low

ions. In this case however, the power law indices are fits to projected distance not a radial distance as in Steidel et al. (2010). At face value, this suggests that the column density of the low ions decreases faster than the high ions over the range of projected distances or that the low ions sample a narrower range of CGM velocities and absorbing columns; a result also put forth by Rudie et al. (2019).

While there is good agreement in  $v_{\text{LOS}}$  between Chen et al. (2020) and this study (see Section 5) especially in the high velocity gas at  $D_{\text{tran}} < 100$  kpc,  $\sigma(\text{Ly}\alpha)$  and  $\sigma(\text{C IV})$  are larger by a factor of  $\simeq 2$  than the Liang & Chen (2014) velocity measurements of gas surrounding  $z < 0.176$  galaxies within  $D_{\text{tran}} < 250$  kpc. Moreover, Liang & Chen (2014) find gas moving with  $v_{\text{LOS}} \gtrsim 200$  km s $^{-1}$  almost exclusively arises from  $D_{\text{tran}} > 250$  kpc sightlines, contrary to our results. The authors speculated that the broad velocity wings may be associated with large-scale filaments; in our case, most of the  $v_{\text{LOS}} \gtrsim 250$  km s $^{-1}$  excess  $\text{Ly}\alpha$  absorption likely arises from star formation induced outflows.

Our  $W_\lambda(\text{C IV})$  vs.  $D_{\text{tran}}$  dependence is consistent with the results of Adelberger et al. (2005), Steidel et al. (2010), and Turner et al. (2014) where the samples have overlap in  $D_{\text{tran}}$ . Adelberger et al. (2005) reported C IV with a velocity spread  $\simeq 260$  km s $^{-1}$  for  $D_{\text{tran}} \lesssim 80$  kpc using galaxy-galaxy pairs and Steidel et al. (2010) extended these measurements to  $D_{\text{tran}} \simeq 100$  kpc. The  $W_\lambda(\text{C IV})$  measurements from both studies are in agreement with our sample (which recall is a broad superset of theirs); the additional galaxy-galaxy pairs at  $D_{\text{tran}} > 100$  kpc in our sample enable an analysis that was



not possible previously. At  $\langle z_{\text{fg}} \rangle \sim 2.6$ , Méndez-Hernández et al. (2022) measured  $W_\lambda(\text{C IV})$  vs.  $D_{\text{tran}}$  around 238 star-forming galaxies at  $D_{\text{tran}} < 173$  kpc. Both this sample and the Méndez-Hernández et al. (2022) measurements are consistent in their slopes and approximate  $W_\lambda(\text{C IV})$  values although the Méndez-Hernández et al. (2022)  $D_{\text{tran}}$  sampling and spectral resolution are considerably coarser.

We find the  $z \simeq 2.3$  QSO-QSO pairs in Prochaska et al. (2014) have systematically larger  $W_\lambda(\text{C IV})$  but have a similar  $W_\lambda$  vs.  $D_{\text{tran}}$  power law index to our sample. Surprisingly, the  $z \simeq 3.3$  Ly $\alpha$  emitters studied in Muzahid et al. (2021) do not show a  $W_\lambda(\text{C IV})$  vs.  $D_{\text{tran}}$  dependence. A possible explanation for this discrepancy is that  $D_{\text{tran, med}} = 165$  kpc for the Muzahid et al. (2021) sample and the largest variability in  $W_\lambda(\text{C IV})$  tends to be at  $D_{\text{tran}} \lesssim 100$  kpc. Indeed our sample shows only a factor of  $\simeq 2$  change in  $W_\lambda(\text{C IV})$  between  $D_{\text{tran}} \simeq 100$  kpc and  $D_{\text{tran}} \simeq 250$  kpc.

We observe that  $W_\lambda(1548)/W_\lambda(1550)$  transitions from  $\simeq 1$  to  $\simeq 2$  around  $D_{\text{tran}} \simeq 60$  kpc (Figure 9) and the velocity centroid over the full C IV doublet becomes consistently blueshifted at a similar projected distance (Figure 8) suggesting C IV becomes optically thin around that point. At  $z \leq 0.1$ , Bordoloi et al. (2014) found  $W_\lambda(\text{C IV})$  falls off as a power law with  $D_{\text{tran}}$  and remained detectable out to  $D_{\text{tran}} \approx 100$  kpc. At  $D_{\text{tran}} \simeq 100$  kpc,  $W_\lambda(1548) \lesssim 0.1$  Å and  $\log[N(\text{C IV})] \lesssim 13.5$ ; within a factor of  $\simeq 2$  of our observed  $W_\lambda(\text{C IV})$  and consistent with optically thin C IV. Using QSO-galaxy pairs at  $z \sim 2$ , Turner et al. (2014) also computed  $W_\lambda(\text{C IV})$  and  $N(\text{C IV})$ . In their first and second  $D_{\text{tran}}$  bins (40 – 130 kpc and 130 – 180 kpc), like Bordoloi et al. (2014), they measured  $\log[N(\text{C IV})] \simeq 13.0 - 13.5$  and  $W_\lambda(\text{C IV}) \simeq 0.01 - 0.1$  Å again suggesting optically thin C IV at a similar  $D_{\text{tran}}$  to this study.

The most significant trend when splitting the pair sample up by SED-derived galaxy properties is between C IV absorption strength and  $M_*$ , followed tentatively by SFR. The trend of increased  $W_\lambda(\text{C IV})$  in higher mass galaxies is observed at  $z \sim 0$  (Burchett et al. 2016),  $z \sim 1$  (Kumar et al. 2024) and at  $z \sim 2$  (Méndez-Hernández et al. 2022). Bordoloi et al. (2014) also detected a mild correlation between C IV absorption strength and sSFR in  $z < 0.1$ ,  $\log(M_*/M_\odot) \leq 10$  galaxies but we do not observe this at higher redshift. Bordoloi et al. (2018) and Wilde et al. (2021) report a correlation between  $M_*$  and Ly $\alpha$  absorption strength at  $z < 1$  but evidence for this is not seen in the Méndez-Hernández et al. (2022)  $z \sim 2$  sample. These findings can be reconciled since our sample extends to lower stellar masses (by approximately an order of magnitude) and the most significant change we observe in Ly $\alpha$  absorption occurs between the two lowest mass bins in our sample ( $\log(M_*/M_\odot) \simeq 9$  and  $\log(M_*/M_\odot) \simeq 9.6$ ). It is inter-

esting to note that  $W_\lambda(\text{Mg II})$  depends most strongly on  $M_*$  and SFR for galaxies at  $z \sim 0.5$  (Bordoloi et al. 2011; Rubin et al. 2018a; Chen & Zahedy 2024), the same stellar population parameters that correlate with C IV, but we lack sufficient  $S/N$  in the split pair samples to make a more thorough comparison.

## 7. SUMMARY

We have measured the mean spatial distribution of absorbing gas around galaxy halos at projected distances  $8 \leq D_{\text{tran}}/\text{kpc} \leq 250$  using 2738 KBSS galaxy pairs (see Figure 1 for some examples and Figures 2 and 3 for sample statistics). For galaxy pairs at a given projected distance, we shift background KCWI and LRIS galaxy spectra to the redshift of their associated foreground galaxies and construct stacks binned by  $D_{\text{tran}}$  in the foreground rest frame. We measure the properties of the foreground absorbing gas using rest-UV interstellar absorption features in the composite spectra. Our principal conclusions are:

1. We detect significant excess Ly $\alpha$  absorption throughout the full range of  $D_{\text{tran}}$  sampled (Figures 4 and 5), consistent with previous results using background QSOs (Adelberger et al. 2003, 2005; Rudie et al. 2012; Turner et al. 2014) and background galaxy pairs (Steidel et al. 2010; Chen et al. 2020). Ly $\alpha$  equivalent width falls off as  $W_\lambda \propto D_{\text{tran}}^{-0.50}$ , in agreement with the previously listed studies (Table 1 and Figure 6).
2. After Ly $\alpha$ , C IV is the strongest absorption feature detected in stacks and can be observed to  $D_{\text{tran}} \simeq 250$  kpc around the average galaxy halo.  $W_\lambda(\text{C IV})$  falls off as  $W_\lambda \propto D_{\text{tran}}^{-0.38}$  suggesting that C IV occupies a larger cross-section of the CGM as compared to H I. Using the C IV velocity centroid (Figure 8) and doublet ratio (Figure 9), we determine that C IV transitions from optically thick to optically thin at  $D_{\text{tran}} \simeq 60$  kpc.
3. The remaining high ionization species (Si III and Si IV) are detected out to  $D_{\text{tran}} \simeq 200$  kpc while low ionization species (e.g., Si II, C II, and O I) take on steeper power law profiles (Table 1) with the faintest becoming undetectable between  $D_{\text{tran}} \simeq 60$  kpc (e.g., Si II  $\lambda 1526$ ) and  $D_{\text{tran}} \simeq 100$  kpc (e.g., O I; Figure 6). Using  $W_\lambda(1260)/W_\lambda(1526)$ , we estimate the saturation of the Si II transition with impact parameter and find, like C IV, Si II becomes optically thin at  $D_{\text{tran}} \simeq 70$  kpc. We show how absorption strength varies on a per-transition basis (Figure 10) and demonstrate that the low and high ions with similar absorption profiles DTB (e.g., Si II and C II) tend to also exhibit similar velocity profiles at  $D_{\text{tran}} > 0$  kpc when significantly detected (Figure 11).

4. We split the pairs involving foreground galaxies with SED measurements into subsamples based on their  $M_*$ , SFR, sSFR, and  $E(B - V)$  in a  $D_{\text{tran}}$  bin. The strongest trend seen is between C IV absorption strength and stellar mass (Figures 12 and 17):  $W_\lambda(\text{C IV})$  increases by a factor of  $\simeq 3.5$  at a fixed  $D_{\text{tran}}$  between halos with  $\log(M_*/M_\odot) \simeq 9.0$  and  $\log(M_*/M_\odot) \simeq 10.2$ . Between the same bins,  $W_\lambda(\text{Ly}\alpha)$  increases by a factor of  $\simeq 2$ .  $W_\lambda(\text{C IV})$  is weakly correlated with SFR, increasing by  $\simeq 60\%$  between bins with  $\log[\text{SFR}/(M_\odot \text{ yr}^{-1})] = 0.6$  and  $\log[\text{SFR}/(M_\odot \text{ yr}^{-1})] = 1.2$  (Table 2 and Figure 13).
5. We construct maps of Ly $\alpha$  and C IV absorption (Figure 18) and make a simple model of how the Ly $\alpha$  excess optical depth varies with  $D_{\text{tran}}$  and  $v_{\text{LOS}}$  (Figures 19 and 20). We observe a local minimum in the Ly $\alpha$  LOS velocity dispersion near  $D_{\text{tran}} \simeq 80$  kpc, approximately the same distance as the virial radius of the typical galaxy in our sample. The velocity centroid of the net Ly $\alpha$  absorption profile varies with projected distance. At  $D_{\text{tran}} \lesssim 50$  kpc, Ly $\alpha$  emission at the redshift of the foreground galaxy contributes to the background absorption signal resulting in a net blueshifted Ly $\alpha$  absorption profile (Figure 27). At  $75 \lesssim D_{\text{tran}}/\text{kpc} \lesssim 200$ , we observe a net redshifted profile (as found previously in Chen et al. 2020) using both background galaxies and background QSOs (Figure 22) suggesting emission at the foreground redshift is not directly responsible for the apparent velocity shift at this  $D_{\text{tran}}$ .

KCWI has significantly improved the effective spectral resolution and spatial coverage at small  $D_{\text{tran}}$  of the KBSS galaxy pair sample. This sample, started by Adelberger et al. (2005) and augmented by Steidel et al. (2010), Chen et al. (2020), and now this study, represents a complementary dataset to QSO sightlines with which to study the CGM. With the current sample, we have consistently detected Ly $\alpha$  and C IV over  $D_{\text{tran}} = 8 - 250$  kpc and fit their  $W_\lambda$  with power laws. The other ions follow similar power laws but become too weak to significantly detect sooner – closer to  $D_{\text{tran}} \simeq 60$  kpc for the weakest transitions (e.g. Si II  $\lambda 1526$  and Al II). Si III and Si IV extend out to  $D_{\text{tran}} \simeq 225$  kpc with a fairly steady decrease in  $W_\lambda$  with  $D_{\text{tran}}$  but then be-

come undetectable suggesting the lack of a detection is an artifact of this pair sample and not the result of a physical scarcity of gas. Indeed, the velocity dispersion of Si IV takes on a relatively smooth evolution with  $D_{\text{tran}}$ . As the galaxy pair sample grows, a larger number of pairs and less noisy continua will make it possible to detect Si III and Si IV at larger  $D_{\text{tran}}$  and improve the precision of the measured low ion evolution at small  $D_{\text{tran}}$ .

N. Z. P. thanks Yuanze Ding, Zihui Li, Evan Nuñez, and Zhuyun Zhuang for thought-provoking discussions, sumptuous meals, and capersome camaraderie during the writing of this paper. N. Z. P. additionally thanks Cameron Hummels for his insights into modeling the results presented in this study. The authors thank Rosalie McGurk, Greg Doppmann, Mateusz Matuszewski, and Don Neill for constructive conversations about KCWI. The authors are indebted to Kurt L. Adelberger, Milan Bogosavljević, Dawn K. Erb, Matthew P. Hunt, David R. Law, Olivera Rakic, Naveen A. Reddy, Gwen C. Rudie, Alice E. Shapley, Allison L. Strom, Rachel L. Theios, Ryan F. Trainor, and Monica L. Turner for their efforts towards the KBSS survey over the past  $\sim$ two decades. N. Z. P. and C. C. S. were supported in part by NSF grant AST-2009278. This research has made use of the Astrophysics Data System, funded by NASA under Cooperative Agreement 80NSSC21M00561. Finally, the authors wish to recognize and acknowledge the very significant cultural role and reverence that the summit of Maunakea has always had within the Native Hawaiian community. We are most fortunate to have the opportunity to conduct observations from this mountain.

*Software:* matplotlib (Hunter 2007), numpy (Harris et al. 2020), scipy (Virtanen et al. 2020), Astropy (The Astropy Collaboration et al. 2013, 2018, 2022), YT (Turk et al. 2011), TRIDENT (Hummels et al. 2017), tqdm (da Costa-Luis et al. 2024), scikit-image (Van Der Walt et al. 2014), multiprocessing (McKerns et al. 2012), corner (Foreman-Mackey 2016), IRAF<sup>9</sup> (Tody 1986, 1993; National Optical Astronomy Observatories 1999; Fitzpatrick et al. 2024), seaborn (Waskom 2021), plotly (Plotly Technologies Inc. 2015), L.A.COSMIC (van Dokkum 2001), IPYTHON (Perez & Granger 2007)

*Facilities:* Keck:II (KCWI), Keck:I (LRIS), Keck:I (MOSFIRE), Keck:I (HIRES)

## APPENDIX

<sup>9</sup> NOIRLab IRAF is distributed by the Community Science and Data Center at NSF NOIRLab, which is managed by the Association of Universities for Research in Astronomy (AURA) under a cooperative agreement with the U.S. National Science Foundation.

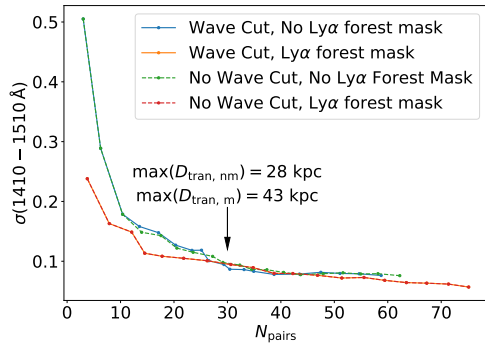


**Figure 21.** Continuum noise ( $\sigma$ ) for a given number of pairs ( $N_{\text{pairs}}$ ) depending on wavelength trimming method. The two options include manual wavelength cuts or a redshift dependent rejection that excludes objects with foreground absorption that falls within the Ly $\alpha$  forest of the background spectrum.

### A. WAVELENGTH TRIMMING

In deciding which galaxies contribute to the galaxy-galaxy pair sample, both Steidel et al. (2010) and Chen et al. (2020) imposed an upper bound on the redshift difference between the foreground and background pairs. The former uses  $\Delta z \leq 1$  while the latter imposes  $\frac{\Delta z}{1+z_{\text{fg}}} < 0.3$ ; for the median foreground and background galaxy redshifts in our sample, these criteria are very similar. We observe that

$$\lambda_{\text{bg}}(1+z_{\text{bg}}) = \lambda_{\text{fg}}(1+z_{\text{fg}}), \quad (\text{A1})$$

or equivalently,

$$\frac{\Delta z}{1+z_{\text{fg}}} = \frac{\lambda_{\text{fg}}}{\lambda_{\text{bg}}} - 1 \quad (\text{A2})$$

where  $\Delta z = z_{\text{bg}} - z_{\text{fg}}$  and  $\lambda_{\text{fg}}$  and  $\lambda_{\text{bg}}$  are the rest wavelengths of a particular transition in the foreground and background frames, respectively. To prevent foreground C IV absorption from being contaminated by unrelated Ly $\alpha$  forest absorption, we chose  $\lambda_{\text{fg}} = 1549 \text{ \AA}$  and  $\lambda_{\text{bg}} = 1216 \text{ \AA}$  so only pairs with  $\frac{\Delta z}{1+z_{\text{fg}}} < 0.27$  are included. Naturally, if one observed significant noise from the background Ly $\alpha$  forest contributing to foreground absorption, this requirement could be strengthened at the cost of many potential foreground/background galaxy pairs; for example, requiring  $\frac{\Delta z}{1+z_{\text{fg}}} < 0.15$  would prevent Ly $\alpha$  forest absorption from contributing to the foreground Si IV profiles.

In our sample, we experimented with several such redshift cuts and found that the continuum noise level is indeed reduced, especially when the number of pairs in a bin is small (see the red dashed curve in Figure 21). In addition to a blanket cut, we also tried wavelength trimming for each individual spectrum, choosing the highest  $S/N$  regions in the bandpass to contribute to the final stacks. This typically involved masking the short wavelength end of the spectrum in

the Ly $\alpha$  forest and (in the case of LRIS) the wavelengths near the dichroic cutoff near  $5600 \text{ \AA}$ . The fact that the noise levels in the stacks remain similar with or without a manual wavelength mask suggests that such trimming is not necessary (see the solid vs. dashed curves in Figure 21).

While both noise mitigation techniques converge once the number of pairs in a bin exceeds 30, the range of  $D_{\text{tran}}$  differs. Figure 21 shows the maximum  $D_{\text{tran}}$  in a bin of 30 pairs drawn from a pair list sorted by  $D_{\text{tran}}$ . In other words, when applying a redshift cut, the 30 pairs with the smallest separations probe  $D_{\text{tran}} \lesssim 43 \text{ kpc}$ ; however, if such a cut is not imposed and each spectrum is manually trimmed of noisy regions, the first 30 pairs sorted by impact parameter probe gas within 28 kpc of an average galaxy halo. Since the noise levels in stacks with  $N \gtrsim 30$  pairs are comparable and all of the stacks in our sample contain at least thirty pairs, we chose to avoid using the blanket redshift cut (dashed green curve in Figure 21), effectively maximizing the number of galaxy pairs contributing to a stack.

### B. HIRES

In order to provide some insight into the cause of asymmetries observed for some of the galaxy-galaxy pair samples, we assembled a sample of QSO-galaxy pairs using existing HIRES spectra of the central QSOs in the KBSS fields (see Rudie et al. 2012; Turner et al. 2014). Briefly, the KBSS QSOs have  $\langle z \rangle \simeq 2.7$ , and their HIRES spectra have  $R \simeq 45,000$  with  $S/N \simeq 50 - 100 \text{ pix}^{-1}$  over the observed wavelength range  $3100 - 6000 \text{ \AA}$ . Figure 22 shows stacks constructed using the same method as for the galaxy-galaxy pair samples, for 53 foreground galaxies with  $D_{\text{tran}} \leq 250 \text{ kpc}$ . The results are shown in two broad bins of  $D_{\text{tran}}$ , for the Ly $\alpha$  and C IV transitions. The bins were chosen to be similar to those used for the galaxy-galaxy pair samples discussed in Section 4.3.) We note that the QSO-galaxy pair measurements pertain to foreground galaxies in the same KBSS survey regions and at similar redshifts, but are completely independent of the galaxy-galaxy pair measurements since the QSO sightlines sample different  $D_{\text{tran}}$  even when probing the same foreground galaxy.

Figure 22 shows that, even when the background spectra have very high  $S/N$  and spectral resolution, the mean profiles from combining QSO-galaxy pairs can be strongly affected by sample variance – stochastic variation of peculiar velocities and component line strength contributed by different QSO-galaxy pairs – as well as by unrelated absorption lines from other redshifts that fall happen to fall within the same wavelength intervals. Applying outlier rejection in forming the stacks reduces the effects of unrelated absorption features and/or unusual absorption profiles in one or a few individual QSO-galaxy pairs; however, with small pair

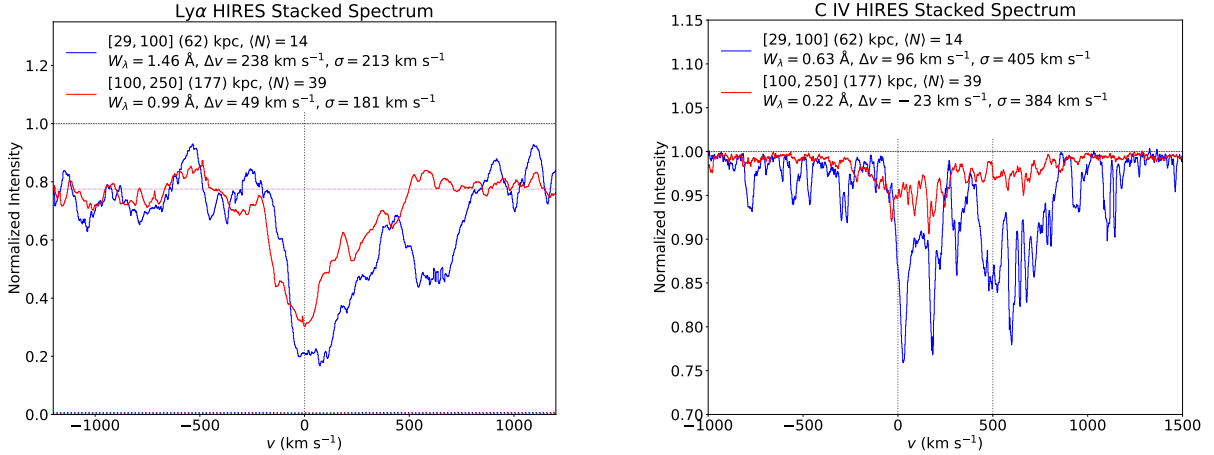


**Figure 22.** Stacked HIRES absorption spectra shifted into the rest frame of the foreground systems centered around the Ly $\alpha$  and C IV transitions. The range of  $D_{\text{tran}}$  and the number of pairs contributing are enumerated in the plot legend. For each bin,  $W_\lambda$ ,  $\Delta v$ , and  $\sigma$  are also shown. The horizontal dotted purple line denotes the suppressed continuum used for the  $W_\lambda(\text{Ly}\alpha)$  measurement.

numbers the average profiles can appear quite asymmetric in velocity (e.g., the blue curves in both panels of Figure 22).

For absorption systems with a high incidence rate such as Ly $\alpha$  (lefthand panel of Figure 22), an additional effect of combining many systems shifted to the redshift of a foreground galaxy is that the net absorption is superposed on a suppressed local continuum, reflecting the average line blanketing in the Ly $\alpha$  forest at the mean redshift of the foreground galaxy sample – in this case,  $\langle z \rangle \sim 2.3$ . For stacks with a relatively small number of contributing QSO-galaxy pairs, sample variance in the local Ly $\alpha$  forest can cause “noise” in the net absorption profile due to fluctuations in the local continuum. The apparent continuum fluctuations become smaller for samples with larger numbers of QSO-galaxy pairs, as do the net velocity asymmetries (i.e., centroid shift relative to  $v = 0$ ; compare the blue and red composites in the lefthand panel of Figure 22.)

For metal line transitions such as the C IV doublet, when limited to redshifts that place C IV at wavelengths longward of Ly $\alpha$  in the spectrum of the background QSO (as in the righthand panel of Figure 22), the continuum remains well-defined. However, small samples may still produce asymmetric C IV profiles that do not resemble a simple velocity-broadened C IV doublet with equivalent width ratio  $1 \leq W_\lambda(1548)/W_\lambda(1550) \leq 2$ , and the velocity centroid of the absorption may also appear shifted with respect to the foreground galaxy systemic redshift for a similar reason. When a larger number of QSO/galaxy pairs is averaged (red spectrum in the righthand panel of Fig. 22) the net profile is much smoother, and has an apparent doublet ratio close to that expected for unsaturated absorption. We observe similar behavior, albeit using galaxy spectra with  $\sim 20 - 30$  times lower resolving power and  $S/N$ , in the galaxy-galaxy pair samples covering similar ranges of  $D_{\text{tran}}$ .

For Ly $\alpha$  and C IV, the values of  $W_\lambda$ ,  $\Delta v$ , and  $\sigma$  for each  $D_{\text{tran}}$  bin are shown in the legend of Figure 22. We find general agreement in  $W_\lambda(\text{Ly}\alpha)$ ,  $\Delta v(\text{Ly}\alpha)$ , and absorption profile morphology between the HIRES 100 – 250 kpc stack of Ly $\alpha$  and the stacks plotted in Figure 16. The computed  $\sigma(\text{Ly}\alpha)$  for the HIRES stacks are 50 – 100  $\text{km s}^{-1}$  lower than their full sample or SED-binned counterparts, but we note that  $\sigma$  depends sensitively on continuum normalization. Similar to the lower resolution stacks, we measure a redshifted velocity centroid at small  $D_{\text{tran}}$  ( $\Delta v = 238 \text{ km s}^{-1}$  at  $D_{\text{tran}} = 62 \text{ kpc}$ ) that approaches the systemic velocity with increasing  $D_{\text{tran}}$  ( $\Delta v = 49 \text{ km s}^{-1}$  at  $D_{\text{tran}} = 177 \text{ kpc}$ ). The C IV profiles all show broad ( $\sigma \sim 400 \text{ km s}^{-1}$ ), nearly symmetric absorption in velocity space with a  $\simeq 100 \text{ km s}^{-1}$  shift towards a blueshifted centroid between the inner (blue) and outer (red) bins. This global trend is consistent with a decreasing optical depth where the individual C IV systems transition from an equivalent width ratio  $W_\lambda(1548)/W_\lambda(1550)$  of one to two.

### C. STACKING METHOD

Before deciding on a trimmed mean (averaging the 5th – 95th percentile spectral pixels) for constructing stacks, we experimented with several other stacking options for the final composite spectra. In theory, with high resolution normalized spectra, any absorption manifests as a narrow feature centered at the rest wavelength in the frame of the foreground galaxy. Foreground galaxies without significant absorption will have normalized intensities close to unity. The distribution of intensities at a given rest wavelength is expected to have a mode near unity and a skew towards smaller normalized intensity caused by real absorption. For any distribution, the mean absorption profile will converge faster than the median for a fixed number of galaxy pairs; on the other hand,

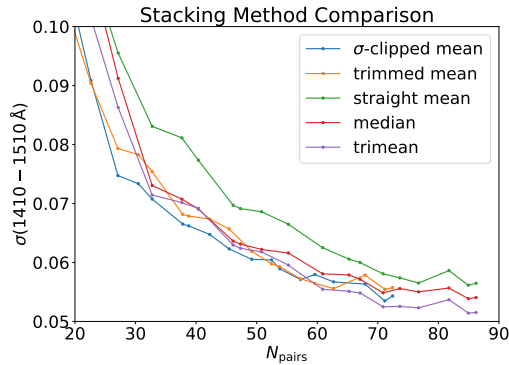


**Figure 23.** Similar to Figure 21, the continuum noise level over the 1410–1510 Å wavelength interval as a function of the number of pairs in a bin is plotted for several methods of combining spectra within that bin.

combining shifted spectra using the pixel-by-pixel mean can result in noise caused by unrelated absorption at other redshifts. This source is clearly exacerbated by averaging over only a few galaxy pairs where background Ly $\alpha$  forest absorption systems can produce large noise spikes at random foreground wavelengths.

In dealing with relatively low resolution ( $R \simeq 670$ ) LRIS spectra, Chen et al. (2020) found that the median of all foreground galaxies in a stack agrees well with a clipped mean using the same spectra, but opted for the median. Now incorporating moderate resolution ( $\langle R \rangle \simeq 1500$  at Ly $\alpha$  and  $\langle R \rangle \simeq 1900$  at C IV) KCWI spectra, we revisit this issue. Figure 23 shows the foreground continuum noise level for a stack as a function of the number of pairs included in the bin. The list of pairs begins at the minimum  $D_{\text{tran}}$  and is sorted by  $D_{\text{tran}}$  so more pairs probe larger  $D_{\text{tran}}$ . The stack is either the mean (green), sigma-clipped mean (blue), trimmed mean (orange), median (red), or the trimean (purple) of the pixels at each wavelength point in that bin. The trimmed mean clips pixels that are either below the 5th percentile or above the 95th percentile at a given wavelength. In the small sample size limit, this algorithm rejects the minimum and maximum values; for larger samples, more pixels may be rejected (effectively 4–6 objects for most of our  $D_{\text{tran}}$  bins). The trimean is defined as

$$\text{TM} \equiv \frac{1}{2} \left( Q_2 + \frac{Q_1 + Q_3}{2} \right) \quad (\text{C3})$$

where  $Q_i$  are the  $i$ th quartiles of the underlying distribution. Although a less efficient estimator than the mean, the trimean emphasizes both the central values and the extrema of a distribution. For our spectra, this measure of central tendency helps mitigate continuum noise while preserving the strength of absorption features.

We note that the straight mean has  $\sim 10\%$  higher noise levels overall compared to the other statistics, which are consis-

tent with one another (to within  $\simeq 5\%$ ). The sigma-clipped mean has a minor advantage for  $N < 50$  pairs, while the trimean has the lowest noise for  $N > 60$  pairs. With  $N > 30$  pairs, each measure of central tendency (straight mean excluded) is consistent with the others, suggesting they are at that point all reflective of the underlying distribution. The straight mean begins to converge to the rest of the metrics with  $N > 60$  pairs.

While the continuum noise level is consistent to within  $\sim 10\%$  regardless of method used, the same is not true for the absorption features. Figure 24 shows two  $D_{\text{tran}}$  bins where the foreground absorption spectra were combined using a trimmed mean (blue) and a median (red). For each absorption line, we observe higher variability near the systemic velocity when using the median over the trimmed mean. As a result, the continuum level in the vicinity of the absorption features is less stable and the equivalent widths one would measure are systematically smaller (see the solid vs. dashed lines in Figure 25). Indeed, Figure 25 shows spectra combined with a trimmed mean have  $W_\lambda \sim 50\%$  larger than those measured in median combined spectra, regardless of the line being measured. The approximate  $W_\lambda$  were measured by integrating over  $|v| \leq 700$  (500) km s $^{-1}$  around the systemic velocity for Ly $\alpha$  (C IV). When considering small  $D_{\text{tran}}$ , the contribution of foreground Ly $\alpha$  emission to the background galaxy spectrum (Appendix D) will bias both the median and average toward smaller  $W_\lambda$ , but if the velocity spread between absorption and emission is not the same, the median may show more variability around the systemic velocity than the mean. We therefore choose to use the trimmed mean as it provides the most distinguishable absorption signal when present.

In using the trimmed mean, we experimented with several different bounds (e.g., asymmetric, Q1 & Q3) but found that clipping the top and bottom 2–6 (depending on the number of pairs in a bin) background spectra was sufficient for achieving noise levels comparable to that of the median while still detecting strong absorption. Put differently,  $\lesssim 5\%$  of the spectra in a particular bin were noisy enough by themselves to result in severe contamination when stacked with  $N \gtrsim 30$  others. It is worth remembering that when normalizing each background spectrum, we only allow regions where the spline fit is consistently above the local (DRP-computed) noise level (evaluated in  $\Delta\lambda \simeq 50$  Å intervals) to enter into the stack (see Section 3.1). Such a requirement ensures that there is a continuum with at least  $S/N \gtrsim 1$  from which to measure absorption. It therefore follows that few of the spectra entering into the stack would need additional trimming.

In addition to noise properties, we investigated the convergence of the Ly $\alpha$  absorption profile for a given number of pairs. Figure 26 shows how the number of pairs averaged (using a trimmed mean) influences the net Ly $\alpha$  profile. For

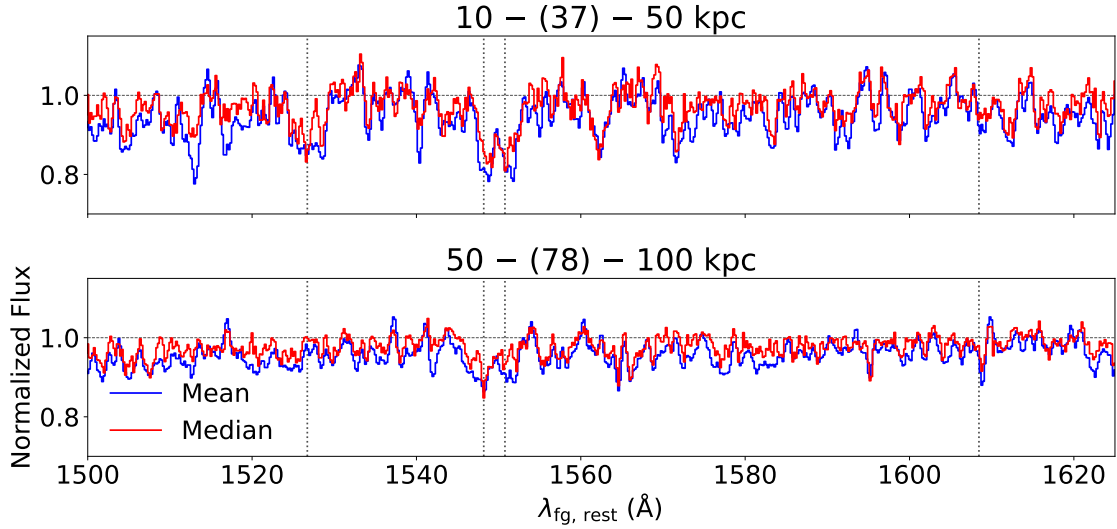


**Figure 24.** Background spectra shifted to the foreground rest frame and stacked using a trimmed mean (blue) and median (red) for two ranges of  $D_{\text{tran}}$  (top: 10 – 50 kpc, bottom: 50 – 100 kpc). The vertical dotted lines show Si II  $\lambda 1526$ , C IV, and Fe II  $\lambda 1608$  and each input spectrum has been normalized as described in Section 3.1.

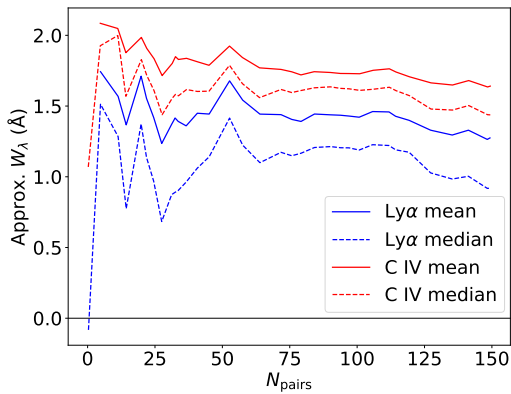


**Figure 25.**  $\text{Ly}\alpha$  (blue) and C IV (red) approximate equivalent width is measured from stacks with varying numbers of constituent galaxy pairs as a test of line profile convergence. The curves start at  $D_{\text{tran}} \simeq 10$  kpc and add pairs with progressively larger separations reaching up to  $D_{\text{tran}} \simeq 52$  kpc. Each stack is combined using either a trimmed mean (solid lines) or median (dashed lines).

transitions measured within the  $\text{Ly}\alpha$  forest of the background galaxy spectrum, a coherent absorption feature does not materialize until at least 10 pairs are averaged. Once 20 pairs are combined,  $\text{Ly}\alpha$  is discernible from the continuum and additional pairs help mitigate  $\text{Ly}\alpha$  forest noise spikes.  $\text{Ly}\alpha$  absorption strength is reduced with increasing  $D_{\text{tran}}$  (see Figure 6) so a larger number of pairs is required to produce absorption profiles with a comparable  $S/N$ . Although there is some sample variance, this effect can be seen by comparing the blue and red spectra in Figure 26: for a given number of pairs, the larger  $D_{\text{tran}}$  bins (red) are marginally noisier around  $\text{Ly}\alpha$  than their small  $D_{\text{tran}}$  counterparts.

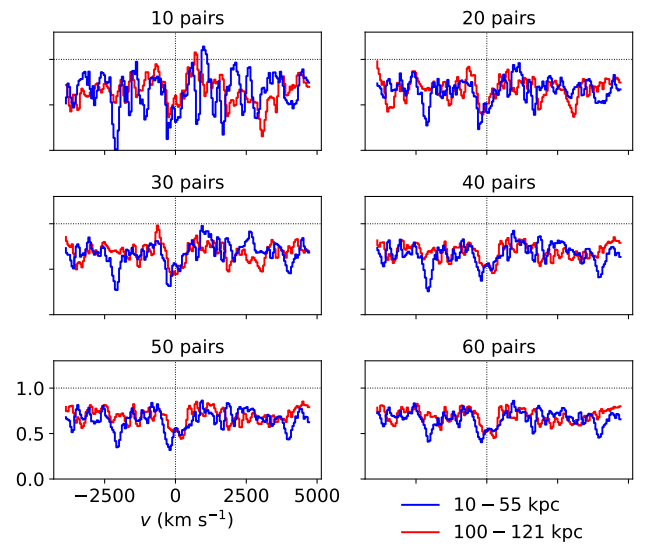


**Figure 26.** A spectral representation of Figures 23 and 25 showing how  $\text{Ly}\alpha$  absorption converges to a well-defined profile as more galaxy pairs are averaged. Two bin “starting points” are shown:  $D_{\text{tran}} \simeq 10$  kpc in blue and  $D_{\text{tran}} \simeq 100$  kpc in red; as more pairs are added, the median  $D_{\text{tran}}$  increases but  $\text{Ly}\alpha$  becomes easier to distinguish from the continuum. Note that the continuum is suppressed by the  $\text{Ly}\alpha$  forest when a sufficient number of pairs are averaged.

More quantitatively, Figure 25 shows that the  $W_\lambda$  varies considerably for stacks with fewer than 20 pairs due to stochastic background  $\text{Ly}\alpha$  forest absorption. However, once the number of pairs reaches  $N \simeq 30$ ,  $W_\lambda$  converges and remains roughly constant with increasing numbers of pairs. If one keeps adding pairs to the bin, the average  $D_{\text{tran}}$  sam-

pled will increase and since pairs at larger  $D_{\text{tran}}$  tend to have weaker absorption (recall absorption  $W_\lambda$  drops with  $D_{\text{tran}}$ ; Figure 6), the measured  $W_\lambda$  in the stacks will begin to fall off when  $\gtrsim 100$  pairs are included, as seen in Figure 25. A similar trend is observed in C IV, albeit with slightly less variability when the number of pairs is small.

Putting all this together, for the trimmed mean stacks, we seek to optimize the number of pairs in each bin such that the continuum noise is minimized and the absorption feature is unambiguous, while still providing as finely sampled of a grid in galactocentric radius as possible. From this analysis and some experimentation with various bins, we find optimum stacks at  $D_{\text{tran}} \lesssim 50$  kpc contain  $N \simeq 30 - 80$  pairs and design the bins used in this study accordingly.

#### D. THE EFFECTS OF Ly $\alpha$ EMISSION HALOS OF FOREGROUND GALAXIES

Chen et al. (2020) noted a significant asymmetry in the Ly $\alpha$  profile, both at  $D_{\text{tran}} \lesssim 40$  kpc and at  $50 \lesssim D_{\text{tran}}/\text{kpc} \lesssim 150$  and suggested that the asymmetry results from foreground Ly $\alpha$  emission contaminating the background Ly $\alpha$  absorption feature. In this work, we confirm the presence of net blueshifted Ly $\alpha$  absorption at  $D_{\text{tran}} \lesssim 40$  and net redshifted absorption at  $50 \lesssim D_{\text{tran}}/\text{kpc} \lesssim 150$  (see e.g. Figure 18). For the net redshifted absorption, we rule out noise arising from a particular set of background spectra (i.e. sample variance) since this feature is larger than the effective resolution element and with  $\langle N \rangle \sim 400$  galaxies being averaged together,  $S/N$  is not a major concern. We also see this effect in the HIRES stacked spectra (Figure 22) which have background sources considerably brighter than the foreground galaxies they probe. Since both means of measuring foreground galaxy absorption show redshifted Ly $\alpha$  absorption, the underlying cause may be related to a hitherto unknown bias in the set of background galaxies or another effect that remains to be explained.

We instead focus on understanding the (net blueshifted) Ly $\alpha$  profile at small  $D_{\text{tran}}$ , where Ly $\alpha$  photons in emission from the foreground galaxy modulate absorption measured from the background galaxy spectrum. We outline an order-of-magnitude calculation below to measure the flux in emission from the foreground galaxy that gets ‘‘added’’ to the background absorption signal. The values we use below are associated with the  $D_{\text{tran}} = 10 - 35$  kpc stack shown in the left panel of Figure 27, but the calculation is similar for the right panel and other  $D_{\text{tran}}$ .

We start by computing the flux ‘‘removed’’ from the background galaxy continuum by the foreground galaxy. In our sample,  $\langle z_{\text{fg}} \rangle = 2.03$  and  $\langle z_{\text{bg}} \rangle = 2.58$  which means Ly $\alpha$  absorption from the foreground system is on average near  $3685 \text{ \AA}$  in the observed frame (or  $1029 \text{ \AA}$  in the background galaxy rest frame). For simplicity, we perform all calcula-

tions in the observed frame. Starting with a stack of the background galaxies shifted to their respective rest frames, we find the average continuum flux density  $f_{\lambda, \text{abs}} \simeq 5 \times 10^{-19} \text{ erg s}^{-1} \text{ cm}^{-2} \text{ \AA}^{-1}$ . At  $D_{\text{tran}} \simeq 20$  kpc we measure a foreground equivalent width  $\langle W_\lambda(\text{Ly}\alpha) \rangle_{\text{fg}} \simeq 2 \text{ \AA}$  (Figure 6); shifting back to the observed frame for comparison with the observed Ly $\alpha$  emission,  $\langle W_\lambda(\text{Ly}\alpha) \rangle_{\text{obs}} = \langle W_\lambda(\text{Ly}\alpha) \rangle_{\text{fg}}(1 + \langle z_{\text{fg}} \rangle) \simeq 6.0 \text{ \AA}$ . Taking the product of the background continuum flux density with the equivalent width of the absorption feature, the background flux removed is  $F_{\text{Ly}\alpha, \text{abs}} = 6.0 \times 5 \times 10^{-19} = 3 \times 10^{-18} \text{ erg s}^{-1} \text{ cm}^{-2}$ .

Now we turn to the emission from the mean Ly $\alpha$  halo profile from KBSS-KCWI. Using a stack of KCWI Ly $\alpha$  halos from Chen et al. (2021, 2025), we construct the radial surface brightness (SB) distribution of Ly $\alpha$  for the mean galaxy halo in the sample. The peak surface brightness integrated over the full Ly $\alpha$  profile is  $\sim 2 \times 10^{-17} \text{ erg s}^{-1} \text{ cm}^{-2} \text{ arcsec}^{-2}$  within  $1'' - 2''$  from the center of the average halo. The halo falls off exponentially: at  $D_{\text{tran}} = 20$  kpc, the SB is down by a factor of  $\sim 10$ , and by  $D_{\text{tran}} = 50$  kpc, a factor of  $\sim 100$  (see also Steidel et al. 2011 and Chen et al. 2021).

To measure the Ly $\alpha$  emission flux contributed at the foreground galaxy redshift to the absorption signal at the same redshift we multiply the foreground galaxy surface brightness profile at the  $D_{\text{tran}}$  of interest with the  $1''.2 \times 1''.2$  KCWI/LRIS typical extraction aperture. Numerically,  $F_{\text{Ly}\alpha, \text{em}} = \text{SB}(D_{\text{tran}} = 20 \text{ kpc}) \times (1''.2)^2 = 2 \times 10^{-18} \times (1.2)^2 = 2.9 \times 10^{-18} \text{ erg s}^{-1} \text{ cm}^{-2}$ .

Comparing the flux in Ly $\alpha$  emission potentially added to the background absorption profile at  $D_{\text{tran}} \simeq 20$  kpc, we find  $F_{\text{Ly}\alpha, \text{em}}/F_{\text{Ly}\alpha, \text{abs}} = 2.9 \times 10^{-18}/3 \times 10^{-18} \simeq 1$  suggesting Ly $\alpha$  flux contributed along the line of sight by foreground galaxy emission is comparable to the flux removed by Ly $\alpha$  absorption. Moving outwards, the contribution of Ly $\alpha$  emission decreases exponentially; a similar calculation at  $D_{\text{tran}} \simeq 50$  kpc reveals  $F_{\text{Ly}\alpha, \text{em}}/F_{\text{Ly}\alpha, \text{abs}} = 0.13$  (13%). These results suggest that at small  $D_{\text{tran}}$ , in addition to the inherent variability associated with combining Ly $\alpha$  forest absorption systems, foreground galaxy Ly $\alpha$  emission may modulate the Ly $\alpha$  absorption profile. However, Ly $\alpha$  emission is unlikely to contribute significantly at  $D_{\text{tran}} \simeq 100$  kpc, and thus cannot be the sole contributor to the net redshifted Ly $\alpha$  profiles observed at  $50 \lesssim D_{\text{tran}}/\text{kpc} \lesssim 150$ .

Figure 27 shows absorption and emission profiles for  $D_{\text{tran}} \simeq 27$  kpc (left) and  $D_{\text{tran}} \simeq 52$  kpc (right). Whereas the order-of-magnitude calculation above compared fluxes, the spectra in Figure 27 are flux densities normalized by the stacked background galaxy continuum level ( $f_{\lambda, \text{abs}} \simeq 5 \times 10^{-19} \text{ erg s}^{-1} \text{ cm}^{-2} \text{ \AA}^{-1}$ ). The orange curves in both panels show normalized background composite spectra similar to those in the left panel of Figure 5.

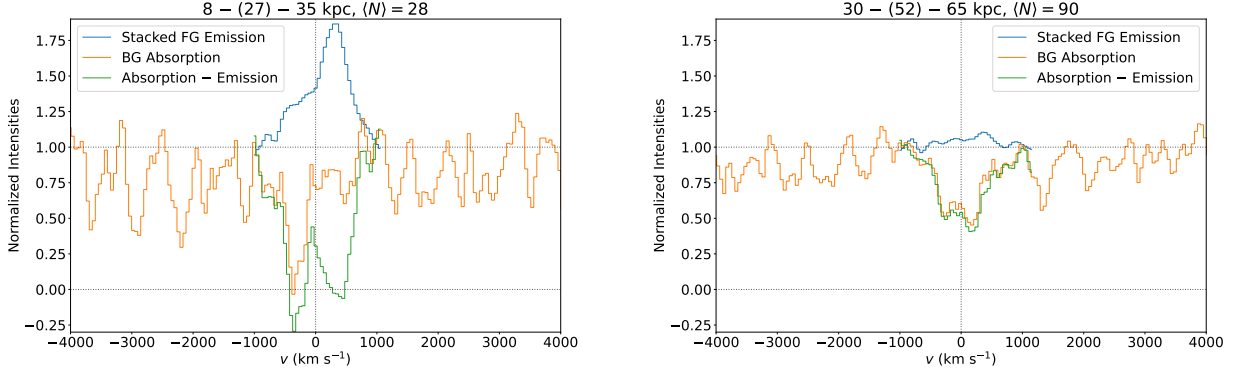


**Figure 27.** The contribution of  $\text{Ly}\alpha$  emission from the foreground galaxy (blue) to the  $\text{Ly}\alpha$  absorption profile measured in the background galaxy spectrum (orange) for two impact parameter bins. The green spectrum is an estimate of the unaffected absorption profile, computed by subtracting the emission feature from the absorption. The number of galaxies contributing to each stack is shown in each plot title.

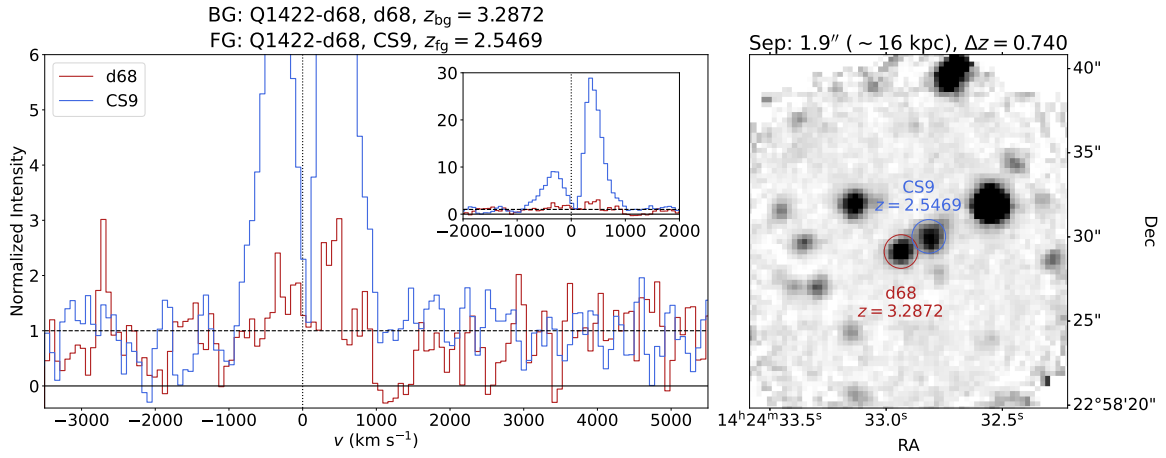


**Figure 28.** *Left:* The spectra of Q1422-d68 (red) and Q1422-d68-CS9 (blue) centered around  $\text{Ly}\alpha$  in the rest frame of CS9. *Right:* White light image of the Q1422-d68 cube with d68 and CS9 circled (same color scheme). We observe emission from CS9 (foreground) contributing to the d68 (background) spectrum effectively masking any absorption within  $v_{\text{LOS}} \simeq 1000 \text{ km s}^{-1}$  of the systemic velocity.

The emission spectra (in Figure 27) were derived from the same foreground galaxy surface brightness distribution used above integrated over the  $D_{\text{tran}}$  of interest and are weighted by the underlying galaxy pair distribution in that bin. The stack of the foreground galaxies again reveals an average continuum flux density  $f_{\lambda, \text{cont}} \sim 5 \times 10^{-19} \text{ erg s}^{-1} \text{ cm}^{-2} \text{ \AA}^{-1}$  and an average  $\text{Ly}\alpha$  emission peak flux density close to  $2 \times 10^{-18} \text{ erg s}^{-1} \text{ cm}^{-2} \text{ \AA}^{-1}$ , both measured in the foreground rest frame at  $D_{\text{tran}} = 0 \text{ kpc}$ . The resultant flux density is then normalized with respect to the continuum level and translated up by +1 for ease of visualization.

In Figure 27, the noise properties of the emission and absorption spectra depend oppositely on  $D_{\text{tran}}$ . As the range of  $D_{\text{tran}}$  increases, the  $S/N$  of the background absorption spectra increases, while at the same time, the  $\text{Ly}\alpha$  surface brightness is decreasing and the emission spectra become noisier. The two bins illustrated in Figure 27 do not meet the fiducial cutoff for the minimum number of pairs in an impact parameter bin ( $N_{\text{pairs}} \gtrsim 30$ ; Appendix C), but represent a compro-

mise where the changing emission and absorption profiles can be seen despite the low  $S/N$ . Both spectra are therefore smoothed with a one pixel ( $\sigma = 50 \text{ km s}^{-1}$ ) Gaussian kernel.

At small  $D_{\text{tran}}$ , the  $\text{Ly}\alpha$  absorption and emission profiles resemble inverted and reflected images of one another (about the intensity and velocity axes respectively). This can be explained simply by considering a symmetric  $\text{Ly}\alpha$  absorption trough where red-dominated emission contributes to the profile resulting in a blue-dominated absorption trough. We note that subtracting off the expected foreground emission from the background (modulated) absorption profile (the green curve in Figure 27) results in a quasi-symmetric  $\text{Ly}\alpha$  absorption line. Since  $\text{Ly}\alpha$  emission falls off exponentially with  $D_{\text{tran}}$ , we would expect this effect to be reduced significantly by  $D_{\text{tran}} \simeq 50 \text{ kpc}$ . Indeed, the observed absorption profile in the right panel of Figure 27 at  $D_{\text{tran}} \simeq 50 \text{ kpc}$  is considerably more symmetric.

As a specific example that illustrates an extreme, we plot the Q1422-d68-CS9 galaxy pair in Figure 28 which has a sep-



aration of  $D_{\text{tran}} \simeq 16$  kpc. Going off of the full sample  $W_\lambda$  vs.  $D_{\text{tran}}$  evolution (Figure 6), at  $D_{\text{tran}} \simeq 16$  kpc, the average  $\text{Ly}\alpha$  absorption system has  $W_\lambda(\text{Ly}\alpha) \simeq 2 \text{ \AA}$ . Instead, the background (d68, red) spectrum at the wavelength of  $\text{Ly}\alpha$  in the foreground shows *emission* with a red-dominated profile similar to that of foreground galaxy (CS9, blue). Only once the  $\text{Ly}\alpha$  emission from foreground galaxy has diminished and no longer contributes (at  $|v| \simeq 1000 \text{ km s}^{-1}$ ) do we

observe absorption. For this particular system, it is likely that the unaffected absorption signal would cover  $|v_{\text{LOS}}| \lesssim 1000 \text{ km s}^{-1}$ , but a brighter background source (e.g. a QSO) would be needed to confirm this. This effect represents one of the pitfalls in using comparably luminous sources as pairs especially at small  $D_{\text{tran}}$  where  $\text{Ly}\alpha$  emission contributes to the background galaxy signal.

## REFERENCES

- Adelberger, K. L., Shapley, A. E., Steidel, C. C., et al. 2005, *ApJ*, 629, 636, doi: [10.1086/431753](https://doi.org/10.1086/431753)
- Adelberger, K. L., Steidel, C. C., Shapley, A. E., et al. 2004, *The Astrophysical Journal*, 607, 226, doi: [10.1086/383221](https://doi.org/10.1086/383221)
- Adelberger, K. L., Steidel, C. C., Shapley, A. E., & Pettini, M. 2003, *The Astrophysical Journal*, 584, 45, doi: [10.1086/345660](https://doi.org/10.1086/345660)
- Behroozi, P. S., Wechsler, R. H., & Conroy, C. 2013, *The Astrophysical Journal*, 770, 57, doi: [10.1088/0004-637X/770/1/57](https://doi.org/10.1088/0004-637X/770/1/57)
- Bergeron, J., & Boissé, P. 1991, *A&A*, 243, 344
- Bertin, E., & Arnouts, S. 1996, *A&AS*, 117, 393, doi: [10.1051/aas:1996164](https://doi.org/10.1051/aas:1996164)
- Bordoloi, R., Prochaska, J. X., Tumlinson, J., et al. 2018, *The Astrophysical Journal*, 864, 132, doi: [10.3847/1538-4357/aad8ac](https://doi.org/10.3847/1538-4357/aad8ac)
- Bordoloi, R., Lilly, S. J., Knobel, C., et al. 2011, *The Astrophysical Journal*, 743, 10, doi: [10.1088/0004-637X/743/1/10](https://doi.org/10.1088/0004-637X/743/1/10)
- Bordoloi, R., Tumlinson, J., Werk, J. K., et al. 2014, *The Astrophysical Journal*, 796, 136, doi: [10.1088/0004-637X/796/2/136](https://doi.org/10.1088/0004-637X/796/2/136)
- Borthakur, S., Heckman, T., Tumlinson, J., et al. 2015, *The Astrophysical Journal*, 813, 46, doi: [10.1088/0004-637X/813/1/46](https://doi.org/10.1088/0004-637X/813/1/46)
- Bouche, N., Cresci, G., Davies, R., et al. 2007, *The Astrophysical Journal*, 671, 303, doi: [10.1086/522221](https://doi.org/10.1086/522221)
- Bouché, N., Murphy, M. T., Kacprzak, G. G., et al. 2013, *Science*, 341, 50, doi: [10.1126/science.1234209](https://doi.org/10.1126/science.1234209)
- Burchett, J. N., Tripp, T. M., Bordoloi, R., et al. 2016, *The Astrophysical Journal*, 832, 124, doi: [10.3847/0004-637X/832/2/124](https://doi.org/10.3847/0004-637X/832/2/124)
- Byrohl, C., & Nelson, D. 2023, *Monthly Notices of the Royal Astronomical Society*, 523, 5248, doi: [10.1093/mnras/stad1779](https://doi.org/10.1093/mnras/stad1779)
- Chen, H.-W., & Zahedy, F. S. 2024, *The Circumgalactic Medium*, arXiv, doi: [10.48550/arXiv.2412.10579](https://doi.org/10.48550/arXiv.2412.10579)
- Chen, Y., Steidel, C. C., Hummels, C. B., et al. 2020, *Monthly Notices of the Royal Astronomical Society*, 499, 1721, doi: [10.1093/mnras/staa2808](https://doi.org/10.1093/mnras/staa2808)
- Chen, Y., Steidel, C. C., Erb, D. K., et al. 2021, *Monthly Notices of the Royal Astronomical Society*, 508, 19, doi: [10.1093/mnras/stab2383](https://doi.org/10.1093/mnras/stab2383)
- da Costa-Luis, C., Larroque, S. K., Altendorf, K., et al. 2024, tqdm: A fast, Extensible Progress Bar for Python and CLI, Zenodo, doi: [10.5281/zenodo.595120](https://doi.org/10.5281/zenodo.595120)
- Dutta, R., Fumagalli, M., Fossati, M., et al. 2020, *Monthly Notices of the Royal Astronomical Society*, 499, 5022, doi: [10.1093/mnras/staa3147](https://doi.org/10.1093/mnras/staa3147)
- . 2021, arXiv:2109.10927 [astro-ph], <http://arxiv.org/abs/2109.10927>
- Erb, D. K., Li, Z., Steidel, C. C., et al. 2023, *The Astrophysical Journal*, 953, 118, doi: [10.3847/1538-4357/acd849](https://doi.org/10.3847/1538-4357/acd849)
- Erb, D. K., Quider, A. M., Henry, A. L., & Martin, C. L. 2012, *The Astrophysical Journal*, 759, 26, doi: [10.1088/0004-637X/759/1/26](https://doi.org/10.1088/0004-637X/759/1/26)
- Faucher-Giguère, C.-A., Kereš, D., & Ma, C.-P. 2011, *Monthly Notices of the Royal Astronomical Society*, 417, 2982, doi: [10.1111/j.1365-2966.2011.19457.x](https://doi.org/10.1111/j.1365-2966.2011.19457.x)
- Faucher-Giguère, C.-A., & Oh, S. P. 2023, *Annual Review of Astronomy and Astrophysics*, 61, 131, doi: [10.1146/annurev-astro-052920-125203](https://doi.org/10.1146/annurev-astro-052920-125203)
- Faucher-Giguère, C.-A., & Quataert, E. 2012, *Monthly Notices of the Royal Astronomical Society*, 425, 605, doi: [10.1111/j.1365-2966.2012.21512.x](https://doi.org/10.1111/j.1365-2966.2012.21512.x)
- Fitzpatrick, M., Placco, V., Bolton, A., et al. 2024, *Modernizing IRAF to Support Gemini Data Reduction*, arXiv, <http://arxiv.org/abs/2401.01982>
- Foreman-Mackey, D. 2016, *The Journal of Open Source Software*, 1, 24, doi: [10.21105/joss.00024](https://doi.org/10.21105/joss.00024)
- Foreman-Mackey, D., Hogg, D. W., Lang, D., & Goodman, J. 2013, *Publications of the Astronomical Society of the Pacific*, 125, 306, doi: [10.1086/670067](https://doi.org/10.1086/670067)
- Hamanowicz, A., Péroux, C., Zwaan, M. A., et al. 2020, *Monthly Notices of the Royal Astronomical Society*, 492, 2347, doi: [10.1093/mnras/stz3590](https://doi.org/10.1093/mnras/stz3590)
- Harris, C. R., Millman, K. J., Van Der Walt, S. J., et al. 2020, *Nature*, 585, 357, doi: [10.1038/s41586-020-2649-2](https://doi.org/10.1038/s41586-020-2649-2)
- Hummels, C. B., Smith, B. D., & Silvia, D. W. 2017, *The Astrophysical Journal*, 847, 59, doi: [10.3847/1538-4357/aa7e2d](https://doi.org/10.3847/1538-4357/aa7e2d)
- Hunter, J. D. 2007, *Computing in Science & Engineering*, 9, 90, doi: [10.1109/MCSE.2007.55](https://doi.org/10.1109/MCSE.2007.55)

- Jacob, J. C., Katz, D. S., Berriman, G. B., et al. 2010, *Montage: An Astronomical Image Mosaicking Toolkit*
- Johnson, S. D., Chen, H.-W., Mulchaey, J. S., Schaye, J., & Straka, L. A. 2017, *The Astrophysical Journal Letters*, 850, L10, doi: [10.3847/2041-8213/aa9370](https://doi.org/10.3847/2041-8213/aa9370)
- Kacprzak, G. G., Nielsen, N. M., Nateghi, H., et al. 2020, *Monthly Notices of the Royal Astronomical Society*, 500, 2289, doi: [10.1093/mnras/staa3461](https://doi.org/10.1093/mnras/staa3461)
- Kereš, D., Katz, N., Weinberg, D. H., & Davé, R. 2005, *Monthly Notices of the Royal Astronomical Society*, 363, 2, doi: [10.1111/j.1365-2966.2005.09451.x](https://doi.org/10.1111/j.1365-2966.2005.09451.x)
- Kluyver, T., Ragan-Kelley, B., Pérez, F., et al. 2016, in *Positioning and Power in Academic Publishing: Players, Agents and Agendas*, ed. F. Loizides & B. Schmidt (Netherlands: IOS Press), 87–90. <https://eprints.soton.ac.uk/403913/>
- Kumar, S., Chen, H.-W., Qu, Z., et al. 2024, *The Open Journal of Astrophysics*, 7, doi: [10.33232/001c.124930](https://doi.org/10.33232/001c.124930)
- Leclercq, F., Bacon, R., Verhamme, A., et al. 2020, *Astronomy & Astrophysics*, 635, A82, doi: [10.1051/0004-6361/201937339](https://doi.org/10.1051/0004-6361/201937339)
- Leitherer, C., Schaerer, D., Goldader, J. D., et al. 1999, *The Astrophysical Journal Supplement Series*, 123, 3, doi: [10.1086/313233](https://doi.org/10.1086/313233)
- Li, Z., Gronke, M., & Steidel, C. C. 2024, *Monthly Notices of the Royal Astronomical Society*, 529, 444, doi: [10.1093/mnras/stae469](https://doi.org/10.1093/mnras/stae469)
- Liang, C. J., & Chen, H.-W. 2014, *Monthly Notices of the Royal Astronomical Society*, 445, 2061, doi: [10.1093/mnras/stu1901](https://doi.org/10.1093/mnras/stu1901)
- Madau, P., & Dickinson, M. 2014, *Annual Review of Astronomy and Astrophysics*, 52, 415, doi: [10.1146/annurev-astro-081811-125615](https://doi.org/10.1146/annurev-astro-081811-125615)
- Martin, C. L., Ho, S. H., Kacprzak, G. G., & Churchill, C. W. 2019, *The Astrophysical Journal*, 878, 84, doi: [10.3847/1538-4357/ab18ac](https://doi.org/10.3847/1538-4357/ab18ac)
- Martin, C. L., Shapley, A. E., Coil, A. L., et al. 2012, *The Astrophysical Journal*, 760, 127, doi: [10.1088/0004-637X/760/2/127](https://doi.org/10.1088/0004-637X/760/2/127)
- McKerns, M. M., Strand, L., Sullivan, T., Fang, A., & Aivazis, M. A. G. 2012, *Building a Framework for Predictive Science*, arXiv. <http://arxiv.org/abs/1202.1056>
- McLean, I. S., Steidel, C. C., Epps, H. W., et al. 2012, in *Society of Photo-Optical Instrumentation Engineers (SPIE) Conference Series*, Vol. 8446, *Ground-based and Airborne Instrumentation for Astronomy IV*, ed. I. S. McLean, S. K. Ramsay, & H. Takami, 84460J, doi: [10.1117/12.924794](https://doi.org/10.1117/12.924794)
- Morrissey, P., Matuszewski, M., Martin, D. C., et al. 2018, *The Astrophysical Journal*, 864, 93, doi: [10.3847/1538-4357/aad597](https://doi.org/10.3847/1538-4357/aad597)
- Murray, N., Ménard, B., & Thompson, T. A. 2011, *The Astrophysical Journal*, 735, 66, doi: [10.1088/0004-637X/735/1/66](https://doi.org/10.1088/0004-637X/735/1/66)
- Muzahid, S., Schaye, J., Cantalupo, S., et al. 2021, *Monthly Notices of the Royal Astronomical Society*, 508, 5612, doi: [10.1093/mnras/stab2933](https://doi.org/10.1093/mnras/stab2933)
- Méndez-Hernández, H., Cassata, P., Ibar, E., et al. 2022, *Astronomy & Astrophysics*, 666, A56, doi: [10.1051/0004-6361/202142553](https://doi.org/10.1051/0004-6361/202142553)
- National Optical Astronomy Observatories. 1999, *IRAF: Image Reduction and Analysis Facility*
- Navarro, J. F., Frenk, C. S., & White, S. D. M. 1996, *ApJ*, 462, 563, doi: [10.1086/177173](https://doi.org/10.1086/177173)
- . 1997, *ApJ*, 490, 493, doi: [10.1086/304888](https://doi.org/10.1086/304888)
- Neill, D., Matuszewski, M., & Martin, C. 2023, *kderp: Keck Cosmic Web Imager Data Extraction and Reduction Pipeline in IDL*
- Peeples, M. S., Werk, J. K., Tumlinson, J., et al. 2014, *The Astrophysical Journal*, 786, 54, doi: [10.1088/0004-637X/786/1/54](https://doi.org/10.1088/0004-637X/786/1/54)
- Perez, F., & Granger, B. E. 2007, *Computing in Science & Engineering*, 9, 21, doi: [10.1109/MCSE.2007.53](https://doi.org/10.1109/MCSE.2007.53)
- Planck Collaboration, Aghanim, N., Akrami, Y., et al. 2020, *Astronomy & Astrophysics*, 641, A6, doi: [10.1051/0004-6361/201833910](https://doi.org/10.1051/0004-6361/201833910)
- Plotly Technologies Inc. 2015, *Collaborative data science*, Montreal, QC: Plotly Technologies Inc. <https://plot.ly>
- Pointon, S. K., Kacprzak, G. G., Nielsen, N. M., et al. 2019, *The Astrophysical Journal*, 883, 78, doi: [10.3847/1538-4357/ab3b0e](https://doi.org/10.3847/1538-4357/ab3b0e)
- Prochaska, J. X., Lau, M. W., & Hennawi, J. F. 2014, *The Astrophysical Journal*, 796, 140, doi: [10.1088/0004-637X/796/2/140](https://doi.org/10.1088/0004-637X/796/2/140)
- Prochaska, J. X., Weiner, B., Chen, H.-W., Mulchaey, J., & Cooksey, K. 2011, *The Astrophysical Journal*, 740, 91, doi: [10.1088/0004-637X/740/2/91](https://doi.org/10.1088/0004-637X/740/2/91)
- Prusinski, N. Z., & Chen, Y. 2024, *KCWIKit: KCWI Post-Processing and Improvements*
- Prusinski, N. Z., Erb, D. K., & Martin, C. L. 2021, *The Astronomical Journal*, 161, 212, doi: [10.3847/1538-3881/abe85b](https://doi.org/10.3847/1538-3881/abe85b)
- Péroux, C., & Howk, J. C. 2020, *Annual Review of Astronomy and Astrophysics*, 58, 363, doi: [10.1146/annurev-astro-021820-120014](https://doi.org/10.1146/annurev-astro-021820-120014)
- Rauch, M., Sargent, W. L. W., & Barlow, T. A. 2001, *ApJ*, 554, 823, doi: [10.1086/321402](https://doi.org/10.1086/321402)
- Reddy, N. A., Steidel, C. C., Erb, D. K., Shapley, A. E., & Pettini, M. 2006, *ApJ*, 653, 1004, doi: [10.1086/508851](https://doi.org/10.1086/508851)
- Richards, G. T., Strauss, M. A., Fan, X., et al. 2006, *The Astronomical Journal*, 131, 2766, doi: [10.1086/503559](https://doi.org/10.1086/503559)
- Rubin, K. H. R., Diamond-Stanic, A. M., Coil, A. L., Crighton, N. H. M., & Moustakas, J. 2018a, *The Astrophysical Journal*, 853, 95, doi: [10.3847/1538-4357/aa9792](https://doi.org/10.3847/1538-4357/aa9792)

- Rubin, K. H. R., Diamond-Stanic, A. M., Coil, A. L., Crighton, N. H. M., & Stewart, K. R. 2018b, *The Astrophysical Journal*, 868, 142, doi: [10.3847/1538-4357/aad566](https://doi.org/10.3847/1538-4357/aad566)
- Rubin, K. H. R., Xavier Prochaska, J., Koo, D. C., & Phillips, A. C. 2012, *The Astrophysical Journal*, 747, L26, doi: [10.1088/2041-8205/747/2/L26](https://doi.org/10.1088/2041-8205/747/2/L26)
- Rudie, G. C., Steidel, C. C., Pettini, M., et al. 2019, *The Astrophysical Journal*, 885, 61, doi: [10.3847/1538-4357/ab4255](https://doi.org/10.3847/1538-4357/ab4255)
- Rudie, G. C., Steidel, C. C., Trainor, R. F., et al. 2012, *The Astrophysical Journal*, 750, 67, doi: [10.1088/0004-637X/750/1/67](https://doi.org/10.1088/0004-637X/750/1/67)
- Shapley, A. E., Steidel, C. C., & Pettini, M. 2003, 588
- Stanway, E. R., & Eldridge, J. J. 2018, *Monthly Notices of the Royal Astronomical Society*, 479, 75, doi: [10.1093/mnras/sty1353](https://doi.org/10.1093/mnras/sty1353)
- Steidel, C. C., Adelberger, K. L., Shapley, A. E., et al. 2003, *The Astrophysical Journal*, 592, 728, doi: [10.1086/375772](https://doi.org/10.1086/375772)
- Steidel, C. C., Bogosavljević, M., Shapley, A. E., et al. 2011, *The Astrophysical Journal*, 736, 160, doi: [10.1088/0004-637X/736/2/160](https://doi.org/10.1088/0004-637X/736/2/160)
- . 2018, *The Astrophysical Journal*, 869, 123, doi: [10.3847/1538-4357/aaed28](https://doi.org/10.3847/1538-4357/aaed28)
- Steidel, C. C., Erb, D. K., Shapley, A. E., et al. 2010, *The Astrophysical Journal*, 717, 289, doi: [10.1088/0004-637X/717/1/289](https://doi.org/10.1088/0004-637X/717/1/289)
- Steidel, C. C., Shapley, A. E., Pettini, M., et al. 2004, *ApJ*, 604, 534, doi: [10.1086/381960](https://doi.org/10.1086/381960)
- Steidel, C. C., Strom, A. L., Pettini, M., et al. 2016, *The Astrophysical Journal*, 826, 159, doi: [10.3847/0004-637X/826/2/159](https://doi.org/10.3847/0004-637X/826/2/159)
- Steidel, C. C., Rudie, G. C., Strom, A. L., et al. 2014, *The Astrophysical Journal*, 795, 165, doi: [10.1088/0004-637X/795/2/165](https://doi.org/10.1088/0004-637X/795/2/165)
- Strom, A. L., Steidel, C. C., Rudie, G. C., Trainor, R. F., & Pettini, M. 2018, *The Astrophysical Journal*, 868, 117, doi: [10.3847/1538-4357/aae1a5](https://doi.org/10.3847/1538-4357/aae1a5)
- Strom, A. L., Steidel, C. C., Rudie, G. C., et al. 2017, *The Astrophysical Journal*, 836, 164, doi: [10.3847/1538-4357/836/2/164](https://doi.org/10.3847/1538-4357/836/2/164)
- The Astropy Collaboration, Robitaille, T. P., Tollerud, E. J., et al. 2013, *Astronomy & Astrophysics*, 558, A33, doi: [10.1051/0004-6361/201322068](https://doi.org/10.1051/0004-6361/201322068)
- The Astropy Collaboration, Price-Whelan, A. M., Sipőcz, B. M., et al. 2018, *The Astronomical Journal*, 156, 123, doi: [10.3847/1538-3881/aabc4f](https://doi.org/10.3847/1538-3881/aabc4f)
- The Astropy Collaboration, Price-Whelan, A. M., Lim, P. L., et al. 2022, *The Astrophysical Journal*, 935, 167, doi: [10.3847/1538-4357/ac7c74](https://doi.org/10.3847/1538-4357/ac7c74)
- Theios, R. L., Steidel, C. C., Strom, A. L., et al. 2019, *The Astrophysical Journal*, 871, 128, doi: [10.3847/1538-4357/aaf386](https://doi.org/10.3847/1538-4357/aaf386)
- Tody, D. 1986, in *Society of Photo-Optical Instrumentation Engineers (SPIE) Conference Series*, Vol. 627, *Instrumentation in astronomy VI*, ed. D. L. Crawford, 733, doi: [10.1117/12.968154](https://doi.org/10.1117/12.968154)
- Tody, D. 1993, in *Astronomical Society of the Pacific Conference Series*, Vol. 52, *Astronomical Data Analysis Software and Systems II*, ed. R. J. Hanisch, R. J. V. Brissenden, & J. Barnes, 173
- Tumlinson, J., Peebles, M. S., & Werk, J. K. 2017, *Annual Review of Astronomy and Astrophysics*, 55, 389, doi: [10.1146/annurev-astro-091916-055240](https://doi.org/10.1146/annurev-astro-091916-055240)
- Turk, M. J., Smith, B. D., Oishi, J. S., et al. 2011, *The Astrophysical Journal Supplement Series*, 192, 9, doi: [10.1088/0067-0049/192/1/9](https://doi.org/10.1088/0067-0049/192/1/9)
- Turner, M. L., Schaye, J., Steidel, C. C., Rudie, G. C., & Strom, A. L. 2014, *Monthly Notices of the Royal Astronomical Society*, 445, 794, doi: [10.1093/mnras/stu1801](https://doi.org/10.1093/mnras/stu1801)
- Van Der Walt, S., Schönberger, J. L., Nunez-Iglesias, J., et al. 2014, *PeerJ*, 2, e453, doi: [10.7717/peerj.453](https://doi.org/10.7717/peerj.453)
- van Dokkum, P. 2001, *Publications of the Astronomical Society of the Pacific*, 113, 1420, doi: [10.1086/323894](https://doi.org/10.1086/323894)
- Veilleux, S., Cecil, G., & Bland-Hawthorn, J. 2005, *Annual Review of Astronomy and Astrophysics*, 43, 769, doi: [10.1146/annurev.astro.43.072103.150610](https://doi.org/10.1146/annurev.astro.43.072103.150610)
- Virtanen, P., Gommers, R., Oliphant, T. E., et al. 2020, *Nature Methods*, 17, 261, doi: [10.1038/s41592-019-0686-2](https://doi.org/10.1038/s41592-019-0686-2)
- Waskom, M. 2021, *Journal of Open Source Software*, 6, 3021, doi: [10.21105/joss.03021](https://doi.org/10.21105/joss.03021)
- Weiner, B. J., Coil, A. L., Prochaska, J. X., et al. 2009, *The Astrophysical Journal*, 692, 187, doi: [10.1088/0004-637X/692/1/187](https://doi.org/10.1088/0004-637X/692/1/187)
- Weldon, A., Reddy, N., Topping, M., et al. 2022, arXiv:2203.09539 [astro-ph]. <http://arxiv.org/abs/2203.09539>
- Werk, J. K., Prochaska, J. X., Thom, C., et al. 2013, *The Astrophysical Journal Supplement Series*, 204, 17, doi: [10.1088/0067-0049/204/2/17](https://doi.org/10.1088/0067-0049/204/2/17)
- Wilde, M. C., Werk, J. K., Burchett, J. N., et al. 2021, *The Astrophysical Journal*, 912, 9, doi: [10.3847/1538-4357/abea14](https://doi.org/10.3847/1538-4357/abea14)